



**HAL**  
open science

# Diameter engineering in III-V nanowire heterostructures - Experiments and modelling

Anton Pishchagin

► **To cite this version:**

Anton Pishchagin. Diameter engineering in III-V nanowire heterostructures - Experiments and modelling. Materials Science [cond-mat.mtrl-sci]. Sorbonne Université, 2021. English. NNT : 2021SORUS516 . tel-03828512

**HAL Id: tel-03828512**

**<https://theses.hal.science/tel-03828512v1>**

Submitted on 25 Oct 2022

**HAL** is a multi-disciplinary open access archive for the deposit and dissemination of scientific research documents, whether they are published or not. The documents may come from teaching and research institutions in France or abroad, or from public or private research centers.

L'archive ouverte pluridisciplinaire **HAL**, est destinée au dépôt et à la diffusion de documents scientifiques de niveau recherche, publiés ou non, émanant des établissements d'enseignement et de recherche français ou étrangers, des laboratoires publics ou privés.

# Sorbonne Université

Ecole doctorale 397 : Physique et chimie des matériaux

*Centre de Nanosciences et de Nanotechnologies (C2N)*

## **Diameter engineering in III-V nanowire heterostructures - Experiments and modelling**

Par Anton PISHCHAGIN

Thèse de doctorat de Physique et chimie des matériaux

Dirigée par Frank GLAS

Présentée et soutenue publiquement le 8 juillet 2021

Devant un jury composé de :

**Mme Anna FONTCUBERTA I MORRAL**

Rapporteur

*Professeure, Ecole Polytechnique Fédérale de Lausanne (Lausanne, Suisse)*

**M. Teemu HAKKARAINEN**

Rapporteur

*Senior research fellow, Tampere University (Tampere, Finlande)*

**M. Jean-Noël AQUA**

Examineur

*Maître de conférences, HDR, Sorbonne Université*

**M. Vladimir G. DUBROVSKII**

Examineur

*Professeur, Saint Petersburg State University et Institut Ioffe (Saint-Pétersbourg, Russie)*

**M. Frank GLAS**

Directeur de thèse

*Directeur de recherche CNRS, C2N*

**M. Jean-Christophe HARMAND**

Co-directeur de thèse

*Directeur de recherche CNRS, C2N*

**M. Fabrice OEHLER**

Encadrant de thèse, membre invité

*Chargé de recherche CNRS, C2N*



# Contents

<b>1</b>	<b>Introduction - The present work in the context of nanowire growth studies</b>	<b>1</b>
1.1	Nanowire growth techniques - General overview . . . . .	2
1.2	Crystal structure of III-V nanowires . . . . .	4
1.3	Vapor-liquid-solid growth . . . . .	5
1.4	Axial and radial heterostructures in nanowires . . . . .	8
1.5	Issues addressed in this thesis . . . . .	10
<b>2</b>	<b>Experimental methods</b>	<b>13</b>
2.1	Molecular beam epitaxy . . . . .	13
2.1.1	Principles and components . . . . .	13
2.1.2	Flux calibration by RHEED . . . . .	15
2.2	Nanowire characterisation by electron microscopy . . . . .	19
2.3	Substrate preparation and optimisation of growth conditions . . . . .	20
2.3.1	Non-patterned substrates . . . . .	21
2.3.2	Patterned substrates . . . . .	23
<b>3</b>	<b>Catalyst droplet dynamics</b>	<b>27</b>
3.1	State of the art: vapor fluxes impinging the droplet . . . . .	27
3.2	Experiments on partial droplet consumption . . . . .	30
3.3	Analytical calculation of the various contributions to droplet consumption	33
3.3.1	Direct impingement . . . . .	34
3.3.2	Re-emission . . . . .	34
3.3.3	Contribution of surface diffusion to droplet consumption . . . . .	42
3.3.4	Desorption of P and Ga from the droplet . . . . .	43
3.4	Axial and radial growth during consumption - Experimental determination of the unknown model parameters . . . . .	45
3.5	Dynamics of droplet consumption: model and experiment . . . . .	48
3.6	Changing at will the droplet dimensions . . . . .	51

---

3.7	Summary and conclusions . . . . .	53
<b>4</b>	<b>Towards diameter-modulated nanowires</b>	<b>55</b>
4.1	Modulation of nanowire diameter - State of the art . . . . .	55
4.2	Reducing the nanowire diameter . . . . .	58
4.3	Enlarging the nanowire diameter . . . . .	63
4.4	Conclusions . . . . .	67
<b>5</b>	<b>Geometrical limits for defect-free growth of core/shell nanowires</b>	<b>69</b>
5.1	State of the art: Elastic and plastic strain in core/shell nanowires . . . . .	70
5.1.1	Elastic strain state . . . . .	71
5.1.2	Plastic strain state . . . . .	72
5.2	Elastic strain state of a core/shell nanowire . . . . .	75
5.3	Partial relaxation by dislocation formation . . . . .	80
5.3.1	Straight edge dislocation . . . . .	80
5.3.2	Dislocation loops . . . . .	83
5.4	Crystalline structure of nanowires . . . . .	84
5.5	Geometrical limits for dislocation formation . . . . .	86
5.6	Actual growth of mismatched core/shell nanowires . . . . .	89
5.6.1	General procedure for core/shell nanowire growth . . . . .	89
5.6.2	Growth of the thin core . . . . .	89
5.6.3	Catalyst droplet consumption and shell growth . . . . .	91
5.6.4	Summary of the conditions of GaAs/GaP core/shell nanowire growth . . . . .	93
5.7	Observation of dislocations . . . . .	94
5.8	Comparison of the calculated and experimental geometrical limits for plastic relaxation . . . . .	97
5.9	Summary and conclusions . . . . .	99
<b>6</b>	<b>General conclusion and perspectives</b>	<b>101</b>
	<b>Résumé en français</b>	<b>107</b>
	<b>Bibliography</b>	<b>115</b>

# Acknowledgments

*Не дай вам Бог жить в эпоху перемен*  
*May you live in interesting times*  
*Puissiez-vous vivre à une époque palpitante*

These three and a half years I have spent as a PhD student at the C2N have been marked by many changes. Besides the changes affecting the C2N or even the whole world, there were my personal changes, the changes in the way of thinking, learning and doing research. Good or sometimes inconvenient, these changes always brought me new, interesting and unforgettable experiences and made my PhD as it is.

The road to PhD would not be passed without my supervisors Frank Glas, Jean-Christophe Harmand and Fabrice Oehler. I am very grateful to you for hundreds of hours of fruitful discussions, for useful advices in research and everyday issues, for constructive criticism, for inspiration and for many other reasons, the list of which will not fit into this page.

I thank all the single members of the thesis jury for accepting to be in my PhD defence and evaluating my work: the referees Anna Fontcuberta i Morral and Teemu Hakkarainen and the examiners Jean-Noël Aqua and Vladimir G. Dubrovskii.

Obviously, this work could not have been accomplished alone. I greatly acknowledge Andrea Cattoni for the patterned substrates, Gilles Patriarche for the TEM experiments, Laurent Travers for keeping the MBE machine in a working state and all my C2N colleagues who make the clean room equipment work. I also thank all members of the Marie Skłodowska-Curie Actions network INDEED for organizing conferences, summer schools and internal project events.

I would like to thank all the people I met during these years: my officemate Camille Barbier for the unforgettable moments spent inside and outside the laboratory, and also for improving my French, Marina Yakovleva for the opportunity not to forget Russian, Andrea Scaccabarozzi for being one of my guides during my first months at C2N, Tanbir Kaur Sodhi for making me a professional of turning off the light in the MBE room, Capucine Tong for the possibility to come to the clean room during the thesis writing, Nuño Amador, Federico Panciera, Martina Morassi, Linsheng Liu, Diana She, Romaric de Lépinau, Stéphane Guillet, Christophe Dupuis, Aristide Lemaître and all others I unintentionally forget to mention.

Finally, I wish to thank my family for their support and confidence in me and, especially, my soulmate Liudmila for accepting to leave everything we had in Russia and to move with me to France for new opportunities.



# Chapter 1

## Introduction - The present work in the context of nanowire growth studies

Semiconductor III-V nanowires (NWs) have been investigated for several decades. While not yet widely implemented in commercial products, they nevertheless demonstrate exciting properties as building blocks in transistors [1–6], photonics [7–14], photovoltaics [15–20] and various other applications [21–24]. The NWs offer several key advantages, such as an excellent material and crystal quality and a large range of NW-based structure designs. These include the various combinations of 1D and 0D structures, including some which are specific to NWs, such as crystal phase heterostructures and quantum dots [19, 25–29], axial and radial homo- and heterojunctions with various compositions or doping levels [6, 7, 16], compositional and morphological (*i.e.* periodic changes of NW dimensions along the growth axis) superlattices [11, 13, 30, 31]. Contrary to most bulk and thin film III-V semiconductors, the III-V NWs can be integrated on a silicon substrate without damage to the crystal quality due to their small footprint, which facilitates the accommodation of the lattice-mismatch strain. In addition, the recent progress in NW growth techniques makes it possible to fabricate large ensembles of identical NWs with the same composition, structure and morphology on a single substrate, with a high level of reproducibility. However, the full potential of NW-based devices will only be realized if the NW physical properties (morphology, crystal phase, doping concentrations, compositional profiles) can be precisely tailored. Although nowadays various techniques are used to fabricate NWs of diverse composition and structures, many of the mechanisms controlling their formation and their properties remain to be studied and fully understood [28, 29, 32–34].

## 1.1 Nanowire growth techniques - General overview

There are two approaches for NW fabrication: one can use a top-down method, where NWs with the required properties are obtained by selective etching of a previously grown planar structure, or a bottom-up technique, where NWs are formed by supplying their constituents under suitable growth conditions [35,36]. Even though the top-down approach makes it possible to control precisely the dimensions of the NWs and their position on the substrate, this method suffers from several drawbacks. First, the etching techniques may limit the minimum NW diameter as well as introduce some surface damage. Moreover, fabricating NWs with complex alternating compositions may be quite challenging, especially if it involves lattice-mismatched materials or materials with different crystal phases, since such structures may not exist as a 2D heterostructures. With the bottom-up fabrication approach, most of these issues can be avoided. Recent studies offer various possibilities for precisely tailored NW positions and dimensions [32,33,37–40]. The bottom-up approach also allows one to control the NW composition down to a single monolayer (ML), which is essential for certain structures.

The bottom-up approach for NW fabrication can be divided into catalyst-free and catalyst-assisted mechanisms. In the former case, the NW growth occurs in vapor-solid (VS) mode, when the material is provided in a vapor (V) phase to form the solid (S) NW. Such a growth can occur on a pre-patterned substrate or in a self-assembled fashion [41–44]. If no catalyst is needed, we avoid introducing any kind of impurities from it. On the other hand, catalyst-free selective-area growth requires a complex substrate preparation. In case of self-assembled growth, it starts with the formation of islands, which relies on the strain between the substrate and the deposit, and then evolves into NW growth.

Catalyst-assisted growth can occur either in the vapor-solid-solid (VSS) mode, if the catalyst is in a solid state, or in the vapor-liquid-solid (VLS) mode, if the catalyst is liquid. These two modes are rather similar, except for the growth kinetics and the requirements for the catalyst stability. The VSS mode results in a slower growth rate, and facilitates the obtention of ML-sharp interfaces in NW heterostructures [45, 46]. On the contrary, such sharp interfaces can be difficult to realize in VLS due to the liquid catalyst acting as a large reservoir of growth species [47–49]. On the other hand, the liquid can change and adapt its shape more quickly than the solid. The liquid catalyst facilitates the nucleation of NWs and is an efficient collector for the vapor species. Nevertheless, both VLS and VSS grant a good degree of control over the NW geometry, structure and composition. In this work, we focus on NWs grown in the VLS mode.

The VLS mechanism was introduced by Wagner and Ellis [50] in 1964 in order to explain the growth of Si whiskers (*i.e.* wires with diameters from several  $\mu\text{m}$  to several mm) by chemical vapor deposition. Prior to the growth, Au:Si liquid droplets were formed on a Si(111) substrate. The gaseous reactants were then provided, which led to droplet supersaturation with Si atoms and their precipitation at the liquid-solid interface. Since the decomposition of reactants is catalyzed by the droplet, which stays at the top of the whiskers, this droplet was called the 'catalyst' and such a growth was termed metal-catalyzed.

Shortly after the pioneering work of Wagner and Ellis, the metal-catalyzed VLS technique was employed for growing GaAs whiskers on GaAs by Givargizov [51]. Several decades later, when the diameter of the whiskers was reduced to the nano-metric dimensions, they could be called nanowires, and the metal-catalysed growth of GaAs NWs on Si substrates was demonstrated [52, 53]. It was shown that NWs of elementary semiconductors usually grow along a  $\langle 111 \rangle$  direction. A number of studies were then dedicated to the investigation of this growth regime and to the application of this technique to other III-V compounds and heterostructures [54–61]. Most of these studies used gold particles as a catalyst. Nevertheless, using a gold catalyst may be undesirable. For instance, if one wants to integrate III-V NWs with silicon, the latter will suffer from the deep defect states introduced by Au diffusion. Therefore, some efforts were devoted towards the growth of III-V NWs in a 'self-catalyzed' mode, using the group III element itself as a VLS catalyst.

The first self-assisted growth was demonstrated in 1965 by Barns and Ellis [62] for Ga-catalyzed GaAs 'whisker-like crystals' on GaAs substrates, but these wires were grown in clumps with random growth directions. Vertically-aligned and more or less organized self-catalyzed NWs, namely In-catalyzed InP and InAs NWs, were fabricated only several decades later [63–65]. In these studies, the catalyst In droplets were created either by substrate heating [63] or by direct nucleation on deoxidized [65] or silica-covered [64] substrates.

For GaAs, the first self-catalysed NW growth by MBE was performed on GaAs (001) and (111)B substrates [66], and soon after on Si(100) [67] and Si(111) [68] substrates. In all these cases, a silicon oxide layer was pre-deposited or formed spontaneously on the substrate. The NW growth occurred preferentially at silica depressions ('nanocraters'), which are supposed to be the favoured sites for Ga droplet nucleation. The importance of the silica layer was shown by several studies [69–71]. Namely, it was demonstrated that NW growth on oxidized and oxide-free surface occurs under different conditions and that the amount of the parasitic growth (*i.e.* the growth of 3D crystallites between

the NWs) and the verticality of the NWs depend on the  $\text{SiO}_x$  thickness and roughness. A number of studies were then devoted to a better understanding and control of the homogeneity and regularity of NW arrays. Particularly, it has been reported that pre-established holes in the  $\text{SiO}_x$  layer lead to growth of NW arrays with uniform properties. The catalyst positioning and its interaction with the hole has a significant influence on the NW yield (*i.e.* the proportion of holes giving vertical NWs) and geometry [71–79]. Also, a careful substrate preparation, including the removal of the silica traces inside the holes prior to the growth, is necessary to obtain a high-quality NW array [73,76,77].

Such selective-area growth on a patterned substrate presents several advantages. It ensures that all NWs grow in the same conditions and thus exhibit similar morphological and structural properties, which is of primary importance for NW-based devices. Also, a single NW randomly extracted from the array in order to address its physical properties is representative of the whole ensemble, which simplifies the statistical analysis. On the other hand, this growth technique requires complex and costly procedures (such as lithography and etching) in order to pattern the substrate, the parameters of which have to be precisely adjusted to obtain a high yield of vertical NW.

## 1.2 Crystal structure of III-V nanowires

Most of bulk or planar layer III-V semiconductors exhibit a cubic zinc blende (ZB) crystal structure, except for nitrides, which usually adopt a hexagonal wurtzite (WZ) crystal structure under ambient conditions. The ZB lattice is a face-centred cubic (fcc) lattice with a lattice constant  $a_{ZB}$  (Figure 1.1(a)). It contains two sub-lattices, occupied by group III and group V atoms, and displaced with respect to each other by  $\frac{a}{4}$  (111). The cubic unit cell consists of four atoms of each type.

Along a  $\langle 111 \rangle$  direction (*i.e.* typical NW growth direction), the (111) crystal planes can be either the group III-terminated, labeled (111)A, or group V-terminated ((111)B). In NWs, the latter case is the usual one. When viewed along the diagonal of a cube face, one can see that the crystal is composed by a stack of (111) atomic planes containing group III or group V atoms in a hexagonal arrangement. One calls a monolayer (ML) a biatomic III-V (111) plane. To form a close packed structure (*i.e.* the structure with minimum distance between the atoms), subsequent layers of (111)A and (111)B planes are positioned differently with respect to the first one. The three possible lateral positions are labelled A,B and C. In the ZB crystal structure, the stacking sequence repeats every third layer, *i.e.* the stacking sequence is ‘...ABCABCA...’. This stacking can be described by a hexagonal structure with  $a_{ZB}^{hex} = a_{ZB}/\sqrt{2}$  and

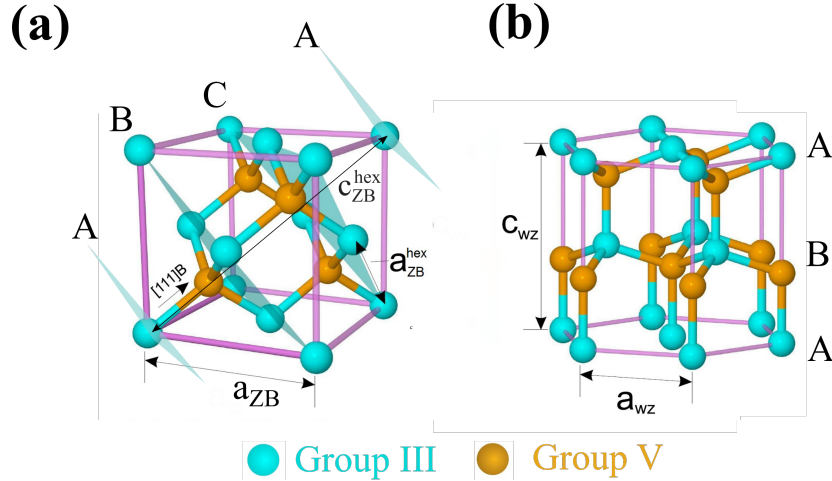


Figure 1.1: Schematics of (a) ZB and (b) WZ unit cell of III-V semiconductors. In ZB structure along  $[111]$  direction the subsequent atomic layers are stacked in a  $\dots ABCBCA \dots$  sequence. The WZ crystal structure has a stacking sequence  $\dots ABABA \dots$ . The lattice constants of the cubic and the hexagonal unit cells are shown (see the main text for details). Adapted from [80].

$$c_{ZB}^{hex} = \sqrt{3} a_{ZB} \text{ (Figure 1.1(a)).}$$

Table 1.1: The lattice parameters of ZB and WZ crystal phases of GaAs and GaP. For the WZ structure the values between brackets are those geometrically converted from ZB unit cell. The values are taken from Refs. [81–84]

	$a_{ZB}$ (nm)	$a_{ZB}^{hex}$ (nm)	$c_{ZB}^{hex}$ (nm)	$a_{WZ}$ (nm)	$c_{WZ}$ (nm)
GaAs	0.565	0.400	0.979	0.399 (0.400)	0.656 (0.652)
GaP	0.545	0.385	0.944	0.384 (0.385)	0.634 (0.629)

The other option to form a close packed structure is to order the layers as  $\dots ABABA \dots$ , forming a WZ structure with  $c[0001]$  axis along the NW growth direction (Figure 1.1(b)). This hexagonal structure has the same in-plane lattice constant  $a_{WZ} = a_{ZB}^{hex}$ , but the  $c$ -axis lattice constant is shorter due to the reduced number of atomic layers, namely  $c_{WZ} = 2a_{ZB}/\sqrt{3}$ . In addition, III-V materials exhibit a slight deviations of the lattice parameters in the WZ phase compared to those, converted geometrically from the ZB crystal [81–83]. Table 1.1 summarizes the lattice constants for the ZB and WZ crystal structures of GaAs and GaP, compounds, used in this Thesis.

### 1.3 Vapor-liquid-solid growth

VLS growth is nowadays widely used for III-V NW fabrication. The growth mechanisms of self-catalyzed NWs are very similar to those of NWs grown by metal-catalyzed VLS. Self-catalysed VLS growth can be roughly divided into two steps: the formation of

the catalyst droplet, often by pre-deposition (Figure 1.2(a)) and the VLS NW growth itself (Figure 1.2(b)). Note that the first step is not mandatory, and the growth can be started by simultaneously providing both group III and group V materials.

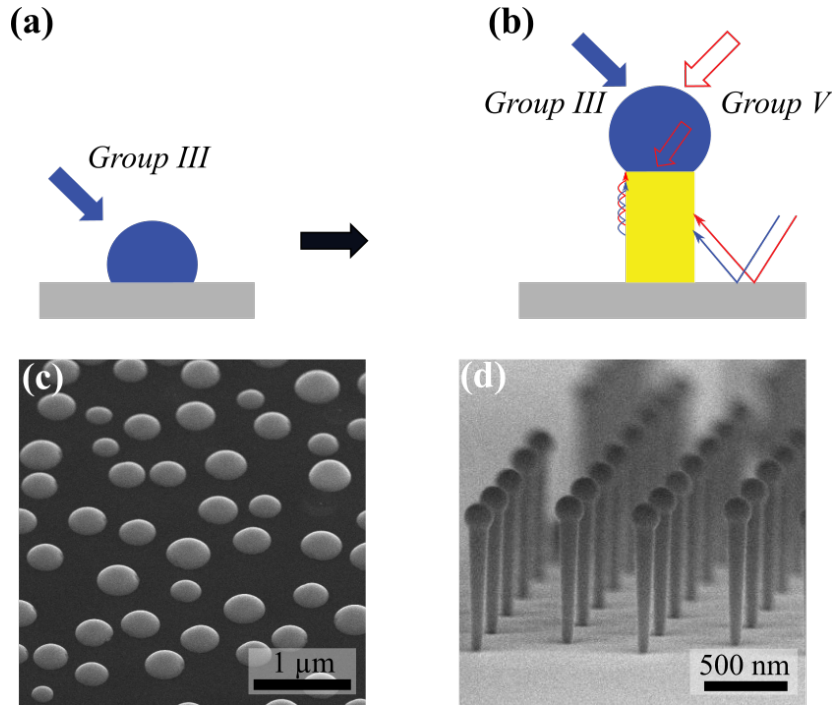


Figure 1.2: Schematics of the self-catalyzed VLS growth of III-V NWs. Growth starts with the deposition of liquid droplets (a), which then serve as a catalyst for solid precipitation (b) beneath it. (c) SEM image of Ga droplets deposited on a Si(111) substrate with native oxide. (d) SEM images of NW array.

In general, the catalyst of group III material (*e.g.* Ga or In) is firstly deposited on the heated substrate in order to form liquid droplets (Figure 1.2(a)). The location of a catalyst droplet determines the future NW position as well as its diameter, albeit in a complex fashion. Next, group III and group V fluxes are provided simultaneously (Figure 1.2(b)). After some incubation time, the concentration of group V material in the droplet exceeds the equilibrium concentration, and the catalyst droplet becomes supersaturated. However, for thin diameter NWs the Gibbs-Thomson effect elevates the liquid chemical potential due to the droplet curvature and imposes a minimal diameter of the liquid metallic droplet above which the nucleation and further NW growth is possible [85–88]. Thus, the growth of extremely thin NWs may require an increase of the supersaturation in the case where group III and group V materials are deposited simultaneously, without pre-deposition.

Once the catalyst is supersaturated, a III-V solid precipitates at the liquid-solid interface below the droplet, and VLS growth takes place. During the growth, the species are transferred twice, from vapor to liquid and then from liquid to solid. These

transfers occur if the chemical potentials  $\mu$  of each species in each phase are in the correct order, namely:

$$\mu_V > \mu_L > \mu_S. \quad (1.1)$$

The first inequality results in the species transfer from vapor to liquid phase, and the second leads to the formation of a solid nucleus. Note that in the stoichiometric crystalline solid, one should consider the chemical potential of a III-V pair rather than those of the atoms. The nucleation event is not necessarily favoured since it involves the formation of new interfaces, which increase the overall energy. The difference  $\mu_L - \mu_S$  must thus be larger than a minimal value. Furthermore, the nucleation can occur either on the liquid-solid interface inside the droplet, or at the triple phase line (TPL), which, as has been shown by Glas *et al* [89], can lead to the formation of a different crystal phase, ZB or WZ.

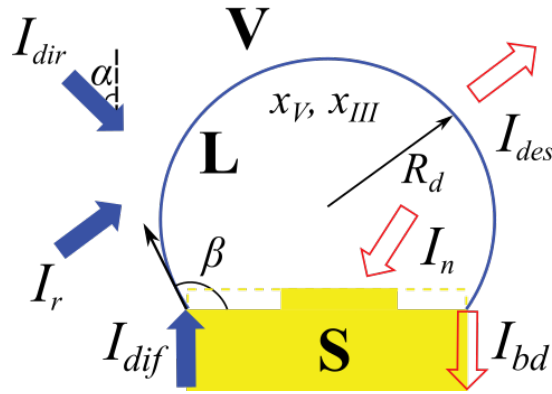


Figure 1.3: Schematics of the currents that feed and empty the droplet during the self-catalyzed VLS growth. Adapted from [90].

Recent studies, based on *in situ* TEM observation of VLS growth of GaAs NWs [91–93], showed that the formation of the WZ crystal structure is favourable for droplet contact angles  $\beta$  in the range  $100 - 125^\circ$ , and that of the ZB crystal structure at smaller or larger contact angles. The droplet contact angle appears to be a major parameter as regards the crystal phase adopted by the NWs during growth<sup>1</sup>. However, one should keep in mind that the formation of WZ structure requires a high enough supersaturation of the liquid. Changing at will the crystal structure is hence possible via controlling  $\beta$ , which can be done by changing the droplet volume.

Since in self-catalyzed VLS growth the droplet consists primarily of group III constituents [90], such a control can be performed by changing the V/III flux ratio, as has

<sup>1</sup>For more complex ternary NWs the crystal phase may also depend on its composition. See, for example, the theoretical study of Johansson and Leshchenko [94].

been recently demonstrated for GaAs [93] and GaP [95] NWs. An excess input of group III inflates the droplet whereas an excess of group V reduces its volume by consuming stored group III atoms to form the III-V solid phase. On the contrary, the droplet maintains a given geometry (contact angle  $\beta$  and radius  $R_d$ ) if the atomic currents of material entering and leaving the droplet are balanced so that:

$$I_{dir,V(III)} + I_{r,V(III)} + I_{dif,V(III)} = I_{des,V(III)} + I_{bd,V(III)} + I_n. \quad (1.2)$$

Here, the terms on the left account for input into the droplet.  $I_{dir}$  stands for direct droplet impingement,  $I_r$  for re-emission by the substrate and neighbouring NWs [90, 96–98] and  $I_{dif}$  for surface diffusion on the NW sidewalls towards the droplet [96, 99, 100]. Note that the surface diffusion includes the species arrived to the sidewalls by direct impingement and by re-emission by the neighbouring surfaces. The right part corresponds to the droplet emptying by desorption  $I_{des,V(III)}$ , possible back diffusion  $I_{bd,V(III)}$  from the droplet [99] and solid nucleation and growth  $I_n$  (Figure 1.3). All these currents depend on the droplet geometry, and some of them (*e.g.*  $I_{des,V(III)}$ ,  $I_n$  and the diffusion fluxes) depend also on the temperature  $T$  and atomic fractions of the material in the droplet  $x_{V(III)}$ . Note also that  $I_{n,V} = I_{n,III}$  since the growth of III-V solid consumes equal numbers of group III and group V atoms.

A change of any current will lead to a change of droplet geometry and to subsequent changes of all currents. Therefore, the understanding and evaluation of each contribution is essential for a precise control the droplet volume and geometry. This requires the explicit calculation of all the separate currents, to finally compute the dynamics of the droplet under varying growth conditions. These questions will be addressed in Chapters 3 and 4.

## 1.4 Axial and radial heterostructures in nanowires

A large number of NW applications, such as NW-based transistors, photodetectors or solar cells, require the formation of single or multiple heterojunctions in the NW. There are two ways to realize a heterojunction in the NW. If the heterojunction is formed along the NW growth axis, we have an axial heterostructure (Figure 1.4(a)). Such a structure is usually grown by changing the constituents supplied according to the required NW composition profile during VLS growth. Nonetheless, obtaining the desired compositional profiles might be challenging, especially due to the reservoir effect in the catalyst [47–49]. When forming an A/B heterostructure, the droplet accumulates material A during the growth of the first section, and the switch from A to B will yield

a segment with compositional A/B gradient. The length of this segment depends on the speed at which the material A will be purged out from the droplet and replaced by material B. Therefore, forming interfaces with desired profiles and abruptness requires the growth conditions to be carefully adjusted [101–105].

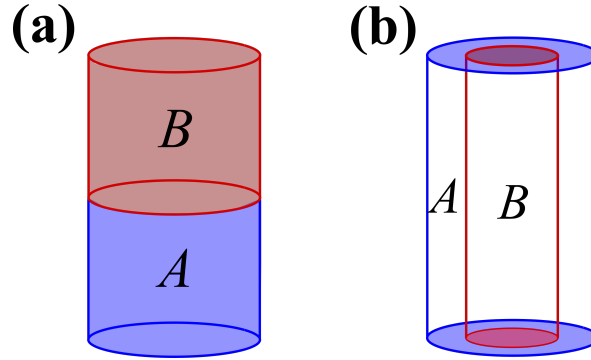


Figure 1.4: Schematic of simplest NW heterostructures: (a) axial heterostructure, (a) core/shell (radial) heterostructure.

In radial (or core/shell) heterostructures, the heterojunction is formed in the lateral direction (Figure 1.4(b)). The inner material is referred to as the core and the surrounding layer as the shell. The main interests of shells is to prevent charge carriers generated in the core to diffuse to the NW surface traps and to strain the NW core and thereby modify the energy levels of the core structure [106–108].

Growth of a NW shell usually occurs in the VS mode. VS growth can also take place in the presence of the apical catalyst droplet, but in this case the rate of the axial growth, which is governed by VLS mechanism, is usually significantly higher than that of the radial growth. If one wants to favour radial growth and to limit as much as possible the NW axial extension during the shell growth, the catalyst droplet must be preliminary removed through crystallization. The shell growth is then performed under a large excess of group V material in order to avoid the re-creation of the catalyst droplet at the NW top and to remain in pure VS growth mode. Both types of heterostructures can be combined so as to produce complex NW structures, *e.g.* single or multishell NWs with quantum dots.

In many cases, the materials of a heterostructure are lattice-mismatched. As in any epitaxial growth, the increase of the thickness of the deposited layer increase the elastic energy stored in the system. At a certain critical thickness, it may become energetically favourable for the deposit to relax plastically by introducing misfit dislocations. The dislocations are known to degrade the optical and electrical properties of the material, since they can act as non-radiative recombination centres and one usually tries to avoid their formation.

The occurrence of such plastic relaxation depends on the composition and the dimensions of the structure. An important feature of the NWs is that the critical thickness under which the deposit remains dislocation-free is significantly larger than in 2D case. In axial NW heterostructures, this is due to the small interface area, which allows the materials to relax laterally. Moreover, for a given mismatch it exists a certain NW radius below which a mismatched layer of any thickness can be grown without forming a dislocation [109, 110]. A similar effect occurs in core/shell structures. The elastic relaxation is less favourable than in axial heterostructures since the core does not have a free lateral surface, which restricts the coherent strain accommodation. Understanding the amount of stress that can be admitted while remaining in the purely elastic (defect-free) regime is thus crucial for the formation of efficient NW-based devices and for the precise tailoring of their properties. This points will be addressed in Chapter 5.

## 1.5 Issues addressed in this thesis

A vast amount of experimental and theoretical investigation has been performed over the last years in order to understand properly the NW growth mechanisms and to achieve a high level of control of their properties, so as they can be used in the fabrication of devices. Nevertheless, there remains many unanswered matters relative to the precise tailoring of the NW geometry, crystal structure, composition and electronic properties, and fabrication of new types of NW-based devices, which would make use of the unique geometry and properties of NWs.

In this thesis, we concentrate on self-catalyzed GaAs and GaP NWs grown on a Si substrate. We address experimental and theoretical issues related to the precise control of the diameter of a NW and particularly its deterministic modification during growth. In **Chapter 2** we introduce our fabrication and characterisation methods. We discuss the calibration and optimisation of the key growth parameters, namely atomic fluxes of the NW constituents and substrate temperature, which govern the NW formation and the precise handling of which is absolutely necessary for fabricating NWs with specific geometry, composition and structure. We also present our efforts in pre-growth substrate preparation and growth conditions optimisation, which allow us to ensure a high homogeneity of the NW properties in a single sample and their reproducibility from sample to sample.

Since the catalyst droplet is key to control the VLS-grown NW composition, dimensions and crystal structure [86, 88], we present in **Chapter 3** a joint experimental and theoretical study of the droplet dynamics. Based on experimental results about

the consumption of a Ga droplet seating on top of a GaP NW, under exposure to a phosphorous flux, we establish the mechanisms that contribute to the decrease of the droplet volume. We provide an explicit theoretical model of droplet evolution during its consumption, which grants control over this process and allows one to obtain (within certain limits) a droplet with desired geometry, even when the real time observation of this process is not accessible.

The ability to alter deterministically the droplet size, in particular its base radius, is key to perform the growth of structures presenting diameter changes or modulations (possibly superlattices) along the NW growth axis. Such periodic morphological changes are expected to change the NW photonic, electronic and thermal properties and could thus be the basis of new types of functional nanostructures where, for instance, carrier confinement would be realized not via composition changes, but via size changes in a single materials [111–113]. **Chapter 4** presents the results of an implementation of our model to modulate locally the NW diameter. We demonstrate the possibility to form a thinner or thicker NW segment of a stable diameter on the top of a stem of the same material, and discuss the mechanisms which lead to this. We also present experimental results on the droplet stable parameters, namely, radius and contact angle, during its inflation and show their dependence on the growth conditions.

To be used in device fabrication, the NWs will usually need to be wrapped by a defect-free shell. Although several studies attempted to understand and evaluate the limits for defect-free shell growth, the results published so far are somewhat confusing, and the models used to derive these results are frequently oversimplified [110]. To clarify some of these issues, in **Chapter 5**, we study the geometrical limits for the dislocation-free formation of the shell in GaAs/GaP core/shell NWs. Accounting for different types of dislocations that can be formed in the shell, we perform the calculation of the critical core and shell dimensions above which dislocations tend to form. These theoretical results are compared with experimental observations of the dislocations in GaAs/GaP core/shell NWs for a broad range of core radii and shell thicknesses.

The experimental and theoretical findings achieved in this Thesis advance our understanding and control of the principles and methods for the fabrication of various types of NW-specific heterostructures. Future research directions and the perspectives, opened by this work are discussed in the Conclusion.



# Chapter 2

## Experimental methods

”Epitaxy” describes the oriented growth of a crystalline material on the surface of another one. Historically, this method refers to the growth of a *film* on a crystalline *substrate*, which imposes its crystal structure and its orientation to this film.

Depending on the means of delivering the material constituents of the deposit to the substrate, the epitaxy techniques can be roughly divided into three groups. If the material is provided from a *liquid* phase, the technique is called liquid phase epitaxy. Vapor phase epitaxy (VPE) involves chemical reactions of precursors, which are carried as a *vapor* to the substrate. In molecular beam epitaxy (MBE), the species are delivered by *molecular* or atomic beams, depending on the element. This is the method we will use and study in this Thesis. VLS growth can be considered as combining MBE or VPE with liquid phase epitaxy.

### 2.1 Molecular beam epitaxy

#### 2.1.1 Principles and components

The MBE growth technique is widely used in the fabrication of various semiconductor structures, particularly NWs. In MBE, growth occurs under ultra-high vacuum (UHV) conditions, which significantly reduces the risk of incorporating impurities in the growing structure and also allows one to avoid the scattering of the material beam on its way to the substrate. In addition, UHV makes it possible to characterize the growing structure by several *in situ* techniques, such as reflection high energy electron diffraction (RHEED), mass-spectrometry, or even transmission electron microscopy. The growth of alloys requires suitable material sources. The typical MBE growth rate of planar films is rather low, about 1 ML/s, which corresponds to approximately 1  $\mu\text{m}/\text{h}$ . This low growth rate grants a very precise (sub-monolayer) control of the thickness and

composition of the fabricated films or nanostructures.

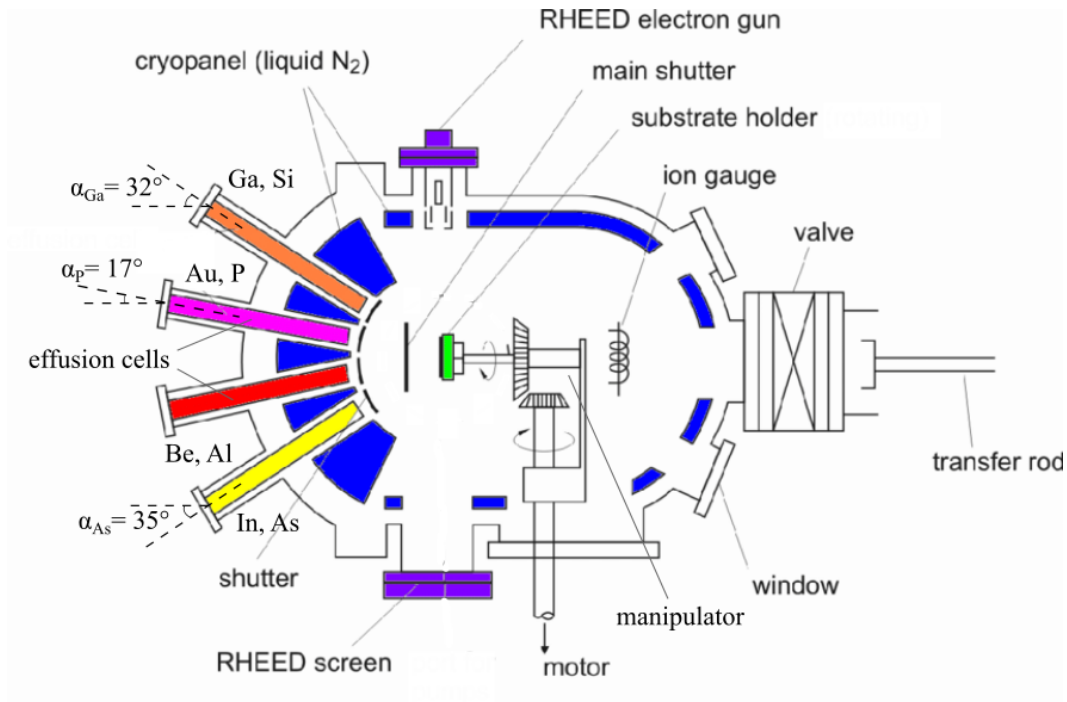


Figure 2.1: Schematics of the RIBER 32 MBE growth chamber. The main components and the materials of the source cells are indicated. The source cell inclination angles with respect to the substrate normal are showed for the materials used in this study, namely gallium ( $\alpha = 32^\circ$ ), phosphorous ( $\alpha = 17^\circ$ ) and arsenic ( $\alpha = 35^\circ$ ).

All the growth experiments presented in this manuscript are performed in a RIBER 32 MBE system (Figure 2.1). The growth chamber is made of UHV-compatible stainless steel and is connected via a gate valve to separate outgas and load-lock modules, used for transfer and pre-growth substrate preparation (not shown in Figure 2.1). The UHV conditions are achieved by the joint use of an ionic, a cryogenic and a Ti sublimation pumps. In addition, the hollow cryopanel, which are placed near the chamber walls and between the material cells, are filled with liquid nitrogen in order to trap the residual molecules and to prevent their re-evaporation. This combination allows one to obtain a typical residual (*i.e.* when all the beams are off) pressure of  $10^{-10} - 10^{-11}$  Torr.

The substrate holder is placed at the center of the chamber, on the manipulator arm, and is usually rotated to improve the homogeneity of the material deposition. The substrate is heated by a filament embedded in a pyrolytic boron nitride disk. The substrate temperature is controlled by the thermocouple fitted at the back of the substrate holder and by two optical pyrometers, operating at 900 nm and 1.1  $\mu\text{m}$ .

The growth chamber comprises 8 source cells, which are disposed in two rows. Six of them, namely Ga, In, Al, Si, Be and Au, are Knudsen-like effusion cells, from which the materials are evaporated from elemental compounds to deliver the atomic fluxes

towards the substrate. Phosphorous and arsenic are provided by valve cracker cells, where the solid material sources are firstly evaporated as tetramers and can then be decomposed into dimers in a separate cracking zone, which is isolated from the reservoir by a valve. Some cells are less inclined with respect to the substrate normal than the others. Specifically, there are four different cell inclination angles:  $\alpha \approx 17^\circ$  for P and Al cells,  $\alpha \approx 32^\circ$  for Ga and In cells,  $\alpha \approx 35^\circ$  for As and Si cells and  $\alpha \approx 16^\circ$  for Be and Au cells (not used in this study). As will be shown in Chapter 3, these inclination angles are crucial to compute the material currents to which the NWs are exposed.

The emitted fluxes are controlled by the crucible temperature (via a thermocouple) for the effusion cells, and by the valve opening for the valved cracker cells. Each cell is equipped with its own mechanical shutter, which allows one to interrupt or to re-establish rapidly the material beams. Additionally, all the fluxes can be interrupted simultaneously by operating the main shutter, which is placed in front of the substrate holder.

### 2.1.2 Flux calibration by RHEED

In order to evaluate the material fluxes, the manipulator of the MBE chamber is equipped with a Bayard-Alpert ion gauge, which can be placed at the substrate growth position by rotating the manipulator. At this position, the gauge can measure a pressure  $P_i^{BA}$ , corresponding to the beam flux of the molecular species  $i$ , emitted from one elemental source at given temperature and/or valve opening. This value is usually referred to as the beam equivalent pressure (BEP). The BEP actually depends on the ionization cross section and the thermal velocity of the molecules considered. It also depends on the solid angle of the beam intercepted by the ionisation volume of the gauge. Therefore, *a priori*, this BEP cannot be directly converted into atomic or molecular flux. Nevertheless, in a limited temperature range of a given source, the BEP is almost proportional to the absolute atomic flux on the substrate,  $F_i$ , (number of atoms per unit area and unit time, in  $\text{at m}^{-2} \text{s}^{-1}$ ). The constant  $\eta_i$  that links the two quantities ( $F_i = \eta_i P_i^{BA}$ ) is different for each material source and depends on the geometry of the growth chamber. It has to be calibrated experimentally for each configuration.

To this end, we employ the RHEED technique, based on the scattering of electrons by the topmost atomic layers of the crystal. The MBE growth chamber is equipped with an electron gun. The electrons are accelerated at 15 keV towards the substrate at grazing incidence ( $1-3^\circ$ ). Due to this low incident angle, the electrons penetrate only to a depth of a few atomic layers in the growing sample and are diffracted to a fluorescent

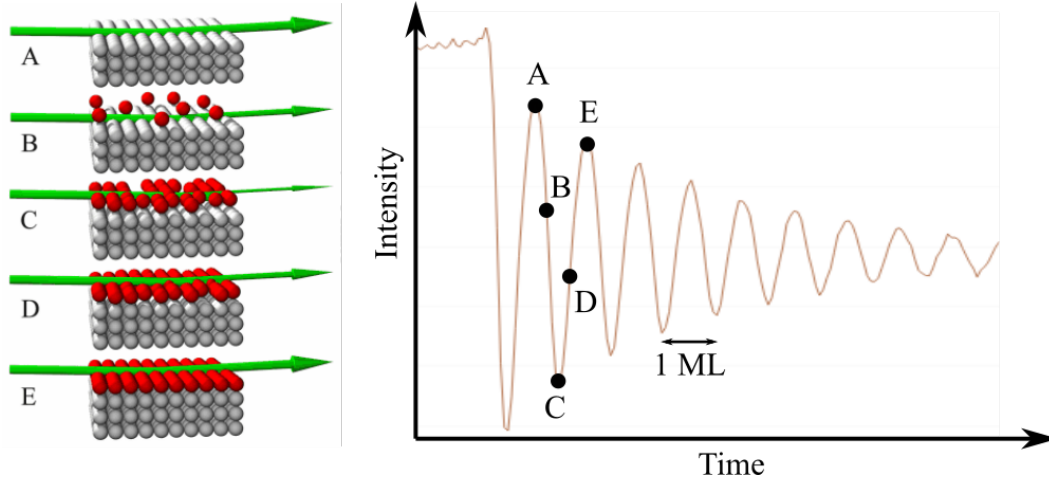


Figure 2.2: Schematics of the RHEED pattern intensity changes and resulting intensity oscillation during the growth of GaAs on a GaAs (001) substrate.

screen. The resulting diffraction pattern provides information about the bulk crystal structure, the surface reconstruction and the morphology of the sample surface. If the sample surface is atomically flat, the RHEED pattern consists of vertical streaks that correspond in reciprocal space to the diffraction rods of a crystalline surface. If the epitaxial growth occurs layer by layer, by nucleation, growth and coalescence of 2D islands, the intensity of the RHEED pattern oscillates with the surface coverage [114]. The reason of this oscillation is showed in Figure 2.2. When the surface is atomically flat (state A), the intensity of the diffracted pattern is maximal. When a ML starts to grow, the roughness of the surface increases due to random nucleus formation, leading to a reduction of intensity (state B). The intensity reaches its minimum when the new ML is half formed (state C). Once the formation of the new ML is complete, the RHEED pattern intensity returns back to a maximum (state E). Therefore, if the epitaxial growth occurs ML by ML, the oscillation period corresponds exactly to the time required to grow a single ML. The inverse of this value is the growth rate expressed in ML/s, which can be easily converted into nm/s, since the ML thickness is known. For cubic (001) III-V materials it is  $a_0/2$ , where  $a_0$  is the lattice parameter of the cubic unit cell (see Figure 1.1, page 5 in Section 1.2 of Chapter 1).

To calibrate the GaAs and GaP 2D deposition rates, RHEED oscillations have been measured during planar growth on GaAs (001) and GaP (001) substrates, respectively. Prior to the growth, the samples were outgassed in a separate chamber at the temperature of 400°C, and then deoxidized in the growth chamber at 600°C under a group V flux. The RHEED oscillations were recorded at 580°C.

When planar growth is performed with an excess of group V species, the growth rate is *group-III limited*. In that case, the RHEED oscillation period  $\tau$  measures the

time necessary to supply the number of group III atoms equivalent to 1 ML, i.e. 2 atoms per area  $a_0^2$ . Thus, we have :

$$F_{III} = \frac{2}{\tau a_0^2} \quad (2.1)$$

When planar growth is performed with an excess of group III species, the sample rapidly degrades because group III atoms accumulate at the surface. However, it is possible to record a few RHEED oscillations in these *group-V-limited* conditions. Similarly to the previous situation, we have :

$$F_V = \frac{2}{\tau a_0^2} \quad (2.2)$$

Note that these expressions do not include that part of the incoming fluxes which may desorb from the sample surface. Experimental conditions corresponding to negligible desorption must be chosen in order to measure the total incoming flux of each species. This is achieved by lowering the substrate temperature during the RHEED intensity oscillation measurements. For an atomic group III flux, this method gives an unambiguous result and the absolute flux is derived. For group V elements, however, there is still an ambiguity when using tetramers. Indeed, Foxon and Joyce [115] reported that  $\text{As}_4$  has a maximum sticking coefficient of 0.5 during the planar growth of GaAs, regardless of growth temperature. This means that for each tetramer only a dimer is incorporated. However, several later studies did not support this conclusion [98, 116, 117]. As for group V dimers, Tok *et al.* [118] reported a sticking coefficient of  $\text{As}_2$  of about 1 for a wide range of growth temperatures. The phosphorous sticking coefficient is not widely discussed in the literature. Barnes *et al.* [119] found that during InP growth, the sticking coefficient of  $\text{P}_2$  is unity at 360°C, but decreases rapidly when the growth temperature increases. Moreover, the sticking coefficient may strongly depend on the substrate material. This can be related to different binding energies for the various III-V pairs. In the present work, we did not study this question, and assume a sticking coefficient of 1. Therefore, the atomic flux used for NW growth is taken equal to that deduced from the RHEED intensity oscillation measurements for both group V and group III elements.

The fluxes  $F_i$  being determined, we can deduce the constants  $\eta_i$  which link these fluxes to the corresponding BEPs  $P_i^{BA}$  that can be measured with the Bayard Alpert gauge before recording the RHEED oscillation.

Figure 2.3(a) shows how the planar growth rate of GaP on GaP (001) varies when the phosphorus BEP  $P_P^{BA}$  is varied by changing the valve opening of the  $\text{P}_2$  cell,

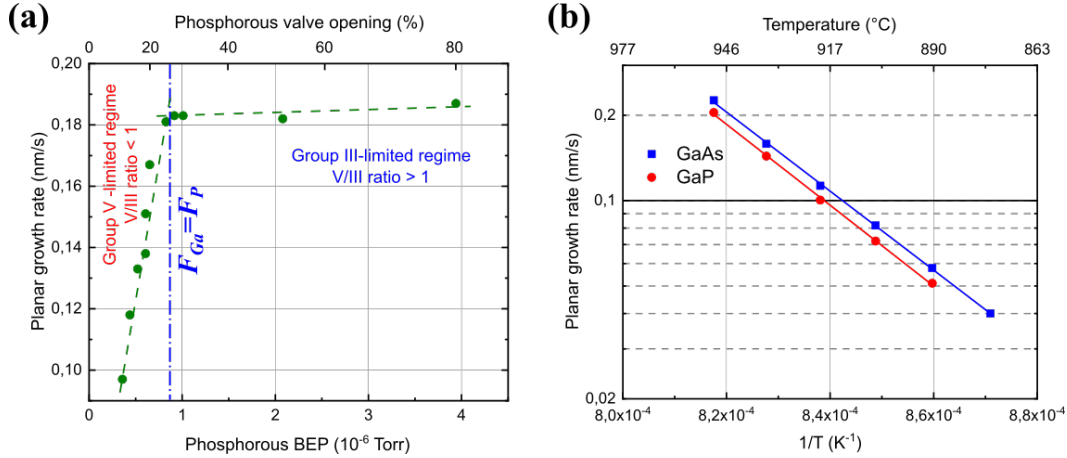


Figure 2.3: (a) Dependence of GaP(001) growth rate on the  $P_2$  BEP and corresponding valve opening, for a fixed Ga deposition rate of 0.19 nm/s. The dash-dotted line indicates the BEP value at which the atomic fluxes of phosphorous and gallium are equal ( $F_P = F_{Ga}$ ) and the transition between group V-limited and group III limited regimes occurs. (b) Growth rates of GaAs (blue squares) and GaP (red circles) measured by RHEED intensity oscillations in the group III-limited regime, as a function of Ga cell temperature.

while the Ga cell temperature is fixed to obtain a constant  $P_{Ga}^{BA}$ . The linear variation observed at low  $P_P^{BA}$  corresponds to the  $P_2$  limited regime, which gives us the  $F_P$  values at different valve openings. The plateau region corresponds to the Ga limited regime which gives us  $F_{Ga}$ . Figure 2.3(b) is a calibration of the Ga growth rate at different Ga cell temperatures, measured by RHEED oscillations during the growth of GaAs on GaAs (001) or GaP on GaP (001). The growth rate  $v$  (in  $\text{nm s}^{-1}$ ) is calculated as:

$$v = \frac{a_0^3}{4} F_{Ga} \quad (2.3)$$

The Ga fluxes  $F_{Ga}$  are the same in both cases (for a given cell temperature), but the conversion into growth rates leads to different results due to the different lattice parameters of GaAs and GaP, with  $v_{GaP} = v_{GaAs} \left( \frac{a_{GaP}}{a_{GaAs}} \right)^3 \approx 0.898 v_{GaAs}$ .

RHEED intensity oscillation calibrations are time-consuming and therefore cannot be performed on a daily basis. Instead, the BEP of each elemental beam is measured every day with the ion gauge and converted in atomic flux by using the constants  $\eta_i$  previously determined. The flux ratio corresponding to equal growth rates for group III and group V elements is equal to one ( $F_V/F_{III} = 1$ ). This is obtained with a BEP ratio  $\frac{P_V^{BA}}{P_{III}^{BA}} = \frac{\eta_{III}}{\eta_V}$ . For our MBE setup, we find  $\frac{\eta_{Ga}}{\eta_P} \approx 4.34$  for GaP and  $\frac{\eta_{Ga}}{\eta_{As}} \approx 9.21$  for GaAs. Knowing this coefficient allows us to distinguish experimentally if the growth occurs in group III or group V limited regime, and also to adjust the fluxes so as to obtain the desired V/III ratio during the growth.

As we shall show in the next Chapters, knowing precisely the atomic fluxes and their flux ratio is very important, since these parameters have a major impact on the geometries of the droplet and hence of the NW. One must keep in mind that the fluxes discussed in this section are measured as captured by a planar substrate. The NW has a more complex geometry and comprises surfaces inclined differently with respect to the incident beams. To be used in NW growth modelling, the measured fluxes have to be corrected according to the cell inclination angles and the geometry of each NW surface.

## 2.2 Nanowire characterisation by electron microscopy

After the growth, the NWs were systematically characterized by scanning electron microscopy (SEM). This technique is widely used for imaging semiconductor structures, since it allows for easy and fast observation of the samples. To produce the image, the sample is scanned by a focused electron beam with energies from 1 to 40 keV, which interacts with the sample and produces various signals, such as secondary and back-scattered electrons, Auger electrons, X-rays etc. All the SEM images presented in this work are obtained by using a FEI Magellan 400L, usually operated at 10 keV. The NWs were observed directly on the substrate, typically with an inclination angle of  $45^\circ$ . For more precise measurements of NW geometry, some NWs were observed in cross-section. To this end, the samples were cleaved so as to have the NWs array as close as possible to the cleaved substrate border, and mounted on a specific sample holder, which allows one to place the NWs perpendicularly to the electron beam.

When detailed characterization of internal structure and composition were required, selected NWs were investigated by transmission electron microscopy (TEM). In contrast to SEM, TEM operates at much higher beam energies (100 - 400 keV), which allows the electrons to traverse the sample, provided the latter is thin enough (typically less than 100 nm). Hence, observing NWs usually does not require any sample thinning. TEM grants a higher image resolution than SEM and can operate in different modes. Among these are the bright-field (BF) mode, where the image is built by collecting the electrons transmitted on axis (with no or little scattering), the dark-field (DF) mode, in which diffracted electrons are collected, and the high-resolution (HR) TEM mode. HRTEM is performed at very high magnification and the obtention of atomic resolution is based on the interference between the direct and various diffracted electron beams. Modern TEMs can also operate in the scanning transmission electron microscopy (STEM) mode. In this mode, the beam is focused to a very narrow spot

and is scanned over the sample, similarly to SEM. The image is then formed either by collecting the electrons scattered at low angles (BF STEM) or at high angles, using an annular detector (HAADF STEM). In the HAADF mode, the electrons are scattered by Coulomb interaction with the atomic nuclei and the resulting image contrast depends strongly on atomic number. This allows one to get some insight on the chemical composition of the sample or even to measure it locally, given proper calibration.

In this work, the NWs were imaged using a FEI TITAN Themis 200 operating at 200 keV. After the growth, NWs were transferred mechanically to a copper TEM grid and observed from their lateral side. For each NW, the grid was tilted in order to align the  $[1\bar{1}0]$  NW crystal axis (in case of a ZB structure) with the electron beam. This technique is mostly employed in Chapter 5, where TEM serves to distinguish the core/shell structure of the NWs and to identify the defects formed in the shell.

Detailed studies of the NW composition, needed for investigating the shell formation in Chapter 5 and to differentiate the growth stages of the NW in Chapter 3, were performed by energy dispersive X-ray spectroscopy (EDX). To this end, the Bruker Super X detector of the FEI TITAN was used. The quantification of the NW chemical composition from the X-ray spectra was performed using the integrated Bruker software. The thickness of each investigated NW was specified in order to account for photon reabsorption and fluorescence.

## 2.3 Substrate preparation and optimisation of growth conditions

As discussed in Chapter 1, the self-catalyzed III-V NWs mostly grow in openings of the silica which covers the Si substrate. The silica layer can either be formed by spontaneous Si surface oxidation (which yields the *native* oxide), or by deposition of a uniform controlled thickness. In the latter method, arrays of holes with pre-defined diameter and order are then formed. We call *patterned* such a substrate. In contrast, the Si substrate with a native oxide will be called *non-patterned*. The two methods are employed in this Thesis. The growth on a patterned substrate results in the formation of uniform NWs for each area of the pattern, since the local growth conditions are the same for each hole [71]. That is why we use patterned  $\text{SiO}_x/\text{Si}(111)$  substrates in Chapters 3 and 4, where we need the NW randomly extracted for TEM examination to be representative of the whole ensemble. In contrast, the droplets deposited on non-patterned substrates present a distribution of size. This distribution as well as the surface density of the catalyst droplets, may be controlled to some degree by tuning the

thickness of deposited material and the substrate temperature [120]. Having NWs with various diameters on a single substrate may be useful if one studies the dependence of certain NW properties on NW dimensions. For our investigation of the geometrical limits for dislocation formation in core/shell NWs (Chapter 5), the NWs were thus grown on non-patterned Si(111) substrates. The (111) orientation of the substrate is chosen so as to provide the NW preferred growth direction (*i.e.* normal to the substrate), as discussed in Chapter 1.

Nevertheless, each kind of substrate requires a specific preparation in order to obtain NW ensembles with the desired properties and to avoid possible parasitic growth. In the next sections, we describe these fabrication steps and present the optimization of the growth conditions made to improve the resulting NW ensembles and avoid as far as possible the formation of parasitic crystallites.

### 2.3.1 Non-patterned substrates

It is known that the surface of a Si crystal exposed to air oxidises, forming a native silica layer with a thickness of 2 nm in a matter of hours [121]. The NW growth can thus be performed directly on a substrate taken from the shelf without any specific treatment. Unfortunately, our standard growth conditions are not optimized for this surface, and we observe a huge parasitic growth of crystallites on the native oxide between the NWs. The formation of such crystallites is detrimental for our study, since it can change the local growth conditions of the surrounding NWs and also reduce the number of NWs appropriate for further analysis. We thus introduce additional substrate processing steps in the pre-growth substrate preparation.

Namely, the initial native oxide is completely removed by wet etching using 5% hydrofluoric acid (HF), and the substrate is then immediately exposed to ultraviolet radiation at room temperature in an ultraviolet/ozone cleaning reactor (UVOX). In addition to general surface cleaning and removal of the organic contamination, such a process grants control and reproducibility of the stoichiometry of the native oxide and of the associated pinhole density. To explore the influence of the UVOX exposure time on the NW growth, we tested UVOX durations of 30 s, 150 s and 300 s. The substrates were then outgassed in a separate chamber at a temperature of 600°C, and GaAs NWs were grown on each, following the VLS growth procedure described in Section 1.3 of Chapter 1.

Firstly, Ga was deposited for 15 s in order to form the catalyst droplets, and Ga and As<sub>4</sub> fluxes with a V/III atomic flux ratio of 2.1 were then provided simultaneously for 20 min. The Ga flux was equivalent to a 2D growth rate of 0.159 nm/s on (001)

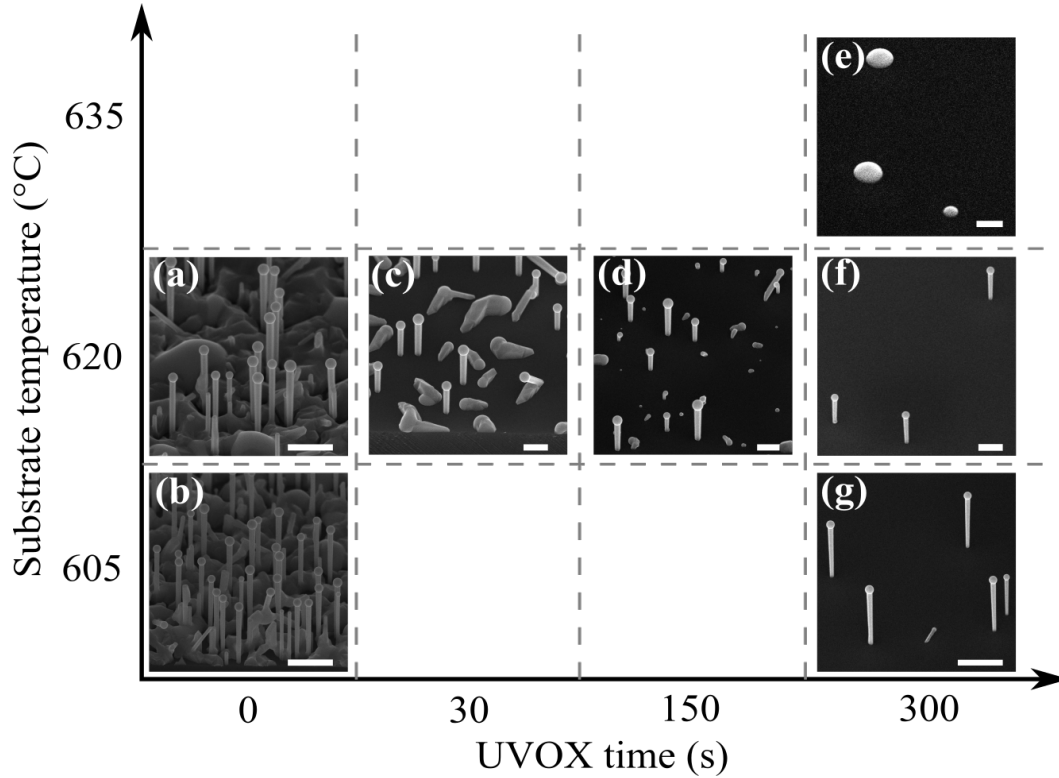


Figure 2.4: Changes in morphology of the substrate during the growth of GaAs NWs after various times of substrate pre-growth exposure to UVOX, and at various substrate temperatures. UVOX time of zero corresponds to the growth on the Si(111) substrate, taken from the shelf, without any specific treatment (native oxide).

GaAs, as measured by RHEED. As can be seen in Figure 2.4(a,b), the growth on the substrate without any specific treatment results in a significant parasitic growth between the NWs, although these are rather dense. Even a short substrate exposure in UVOX significantly reduces the parasitic growth, but the density of NWs also decreases slightly (Figure 2.4(c)). Longer exposures allow us to reduce further (Figure 2.4(d)) and finally to avoid completely (Figure 2.4(f)) the formation of parasitic crystallites. However, the density of NWs decreases continuously with increasing of UVOX exposure time. This can be qualitatively explained by the increase of the  $\text{SiO}_x$  "thickness" with exposure time *i.e.* the reduction of pinhole density and densification of the silica (change of the relative fractions of different species of silica  $\text{SiO}_2$ ,  $\text{SiO}$ ,  $\text{Si}_2\text{O}$ , and  $\text{Si}_2\text{O}_3$ ) [122]. We did not study this effect in more details.

We also investigated the influence of the substrate temperature on the formation of NW ensembles, using the same substrate treatment and growth recipe. For any substrate preparation sequence, we either kept the native oxide or used the UVOX exposure. In both cases, the number of grown features, crystallites as well as NWs, decreases when substrate temperature increases (Figure 2.4(a-b) and (e-g)). In the

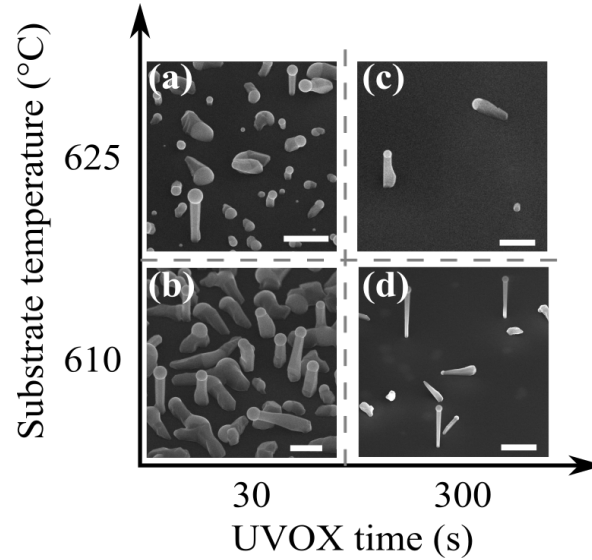


Figure 2.5: Changes in morphology of the substrate during the growth of GaP NWs after various times of substrate pre-growth exposure to UVOX, and at various substrate temperatures.

temperature window 600-620°C, GaAs NW growth is possible. The NWs are slightly shorter for higher temperature, which could indicate a lower concentration of As in the catalyst droplet due to its higher desorption. At 635°C, only a few crystallites are observed.

A similar study, but including less UVOX exposure times and substrate temperatures, was carried out for GaP NWs. The NW growth conditions were the same as for GaAs NWs, but the same Ga flux corresponds to a 2D growth rate of 0.138 nm/s on (001) GaP due to the smaller lattice parameter. As can be seen in Figure 2.5, as regards parasitic growth and NW density, GaP exhibits the same trends as GaAs with temperature and exposure time.

Therefore, for all the growths on *non-patterned* substrates discussed in the next Chapters, we employed the following pre-growth preparation procedure. The Si wafer is firstly dipped in a 5 % HF solution for 30 s for complete deoxidation and then exposed to UVOX for 300 s. Both treatments were performed immediately before the introduction to the MBE system. After outgassing at 600°C, the growth was performed at the same temperature, unless specified otherwise.

### 2.3.2 Patterned substrates

Before patterning, the 2 inches Si(111) wafers are fully deoxidized in a 5 % HF solution and cleaned by an oxygen plasma. A silica layer of about 30 nm is then deposited by plasma-enhanced chemical vapor deposition (PECVD). The thickness uniformity

across the wafer is controlled by ellipsometry. The patterns are written in a poly-methyl methacrylate (PMMA) mask deposited over the silica, by using electron beam lithography (EBL). The typical pattern design is presented in Figure 2.6.

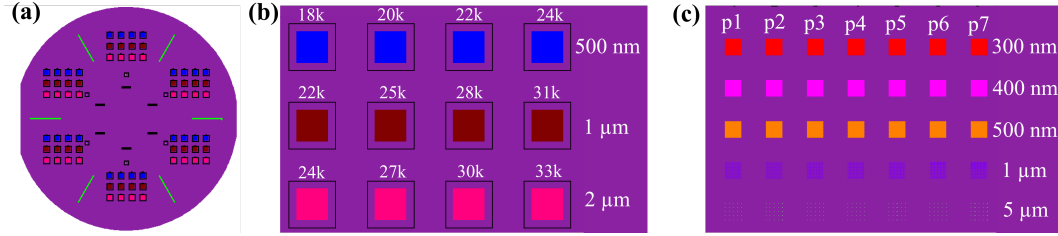


Figure 2.6: Schematics of a patterned 2 inch Si substrate (a), and pattern zones with large (b) and small squares (c). Pitch and doses (b) or number of pixels (c) used for EBL writing, are indicated.

Each sixth of the Si wafer contains several areas, written in different manners. The large matrix with  $1 \text{ mm} \times 1 \text{ mm}$  squares with pitches of 500 nm,  $1 \mu\text{m}$  and  $2 \mu\text{m}$  is written by delivering a single dose at the centre of each hole. The dose varies from 18 000 to 33 000  $\mu\text{C cm}^{-2}$ , (Figure 2.6(b)). The hole size, which increases with the dose, is determined by SEM on a test sample at the end of the pre-growth preparation. The patterns also contain a small square which includes several  $20 \mu\text{m} \times 20 \mu\text{m}$  squares with pitches of 300 nm, 400 nm, 500 nm,  $1 \mu\text{m}$  and  $5 \mu\text{m}$ . In these squares, EBL writes holes of nominal diameters from 20 to 70 nm in a pixel-by-pixel mode, with a beam step size of 1 nm and at a fixed dose of  $2500 \mu\text{C cm}^{-2}$  (Figure 2.6(c)).

Once the pattern is written, it is transferred to the silica layer following the procedure presented in Figure 2.7. Firstly, the substrate with patterned PMMA is processed using reactive ion etching (RIE) by  $\text{CHF}_3$  and  $\text{SF}_6$  gases with a flow ratio of 20:8 (Figure 2.7(b)). The RIE etching rate was previously calibrated on a planar silica layer deposited in the same conditions. Such a calibration is essential, since care should be taken not to etch the holes completely. In practice, we leave a  $\text{SiO}_x$  thickness of 4-5 nm at the bottom. This thin layer prevents the plasma-induced damage of Si during the RIE. The PMMA resist is then removed by using acetone and isopropanol, and the silica surface is cleaned by an oxygen plasma (Figure 2.7(c)).

The final preparation step consists in removing the silica remaining at the bottom of the holes by wet etching in 1 % HF (Figure 2.7(d)). The etching rate of a 1 % HF solution was also previously calibrated. Since, during the wet etching, the sample is not any more protected by the PMMA mask, the HF etches both the silica at the bottom of the holes and the rest of the substrate. The etching time should thus be adjusted so as to ensure the complete opening of the holes, but without thinning the

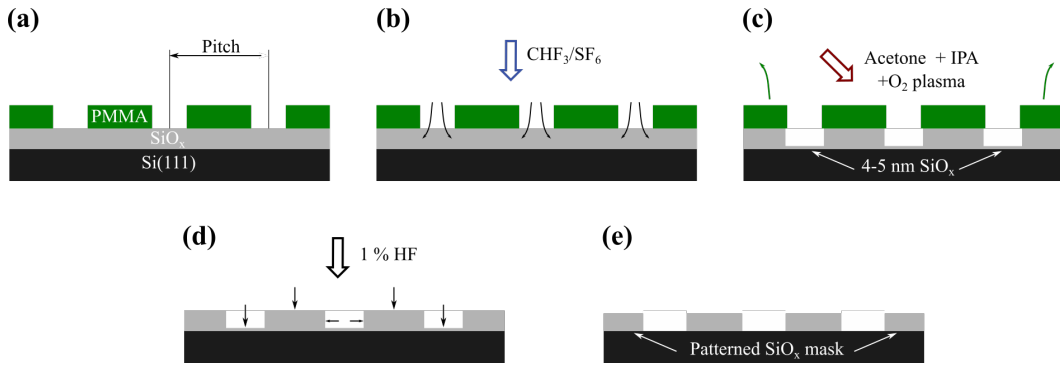


Figure 2.7: Patterned substrate fabrication procedure. (a) Initially, PMMA is patterned by EBL into a hexagonal array of holes. (b) The pattern is then transferred to the underlying silica by RIE, yet without complete hole etching, and (c) the PMMA resist is removed by chemical treatment, followed by substrate oxygen plasma cleaning. (d) Prior to the growth, the substrate is etched by 1 % HF. (e) The complete procedure yields the patterned silica mask. The SiO<sub>x</sub> layer is thinned and the holes are modestly enlarged due to the isotropy of HF wet etching.

rest of the silica excessively. Typically, wet etching is performed for 30-40 s, depending on the silica thickness and HF solution. In order to avoid the possible re-oxidation of the hole bottom, the last etching step is carried out immediately before loading to the MBE system.

Note that during the etching, the silica layer is etched not only in the vertical direction, but also in the lateral (Figure 2.7(b) and (d)). This effect is much more pronounced during wet HF etching, which is isotropic. The actual hole dimensions are thus typically larger than the nominal ones, as defined by EBL. To limit hole enlargement, one needs to reduce as much as possible the duration of the HF treatment. To this end, we always tried to leave the thinnest possible SiO<sub>x</sub> layer at the bottom of the hole after RIE, while making sure that it is not etched completely.



# Chapter 3

## Catalyst droplet dynamics

In Section 1.3 of Chapter 1 we have seen that controlling the droplet volume is crucial to obtain NWs with required geometry and crystal structure. For NWs grown by self-catalysed VLS the droplet contains only the NW elemental constituents (and actually a very large proportion of the group III species) and its volume can be changed at will. Such a change may affect the droplet contact angle, the droplet radius, or both. There is thus a strong interest in understanding the dynamics of droplet consumption in order to control precisely the geometry and the crystal phase of the NW.

In this Chapter, we first review recent studies of the modeling of the various material fluxes which determine the droplet volume. We then present a theoretical model of droplet dynamics, which is based on our *ex situ* investigation of droplet consumption (*i.e.* decrease of its volume). We consider the usual case of droplet consumption by providing only group V atoms and deal with low-density NW arrays, where the shadowing by neighboring NWs can be neglected. We establish the mechanisms that empty the droplet and estimate their respective contributions to the consumption process, which are all given in analytical form. This allows one to predict the droplet evolution under group V exposure. This understanding of the droplet dynamics is particularly important since direct and real-time observation of these processes is not accessible in standard epitaxy systems.

### 3.1 State of the art: vapor fluxes impinging the droplet

Several authors attempted to calculate the various contributions featuring in Eq. 1.2. For the *direct impingement*  $I_{dir}$ , a rigorous calculation has been performed by Glas [123]. His geometrical model of an isolated spherical cap subjected to an external flux, in-

clined by some angle  $\alpha$ , accounts for the variation of effective intercepted droplet area with droplet contact angle  $\beta$ . It is independent of the impinging species and remains valid for arrays of NWs of identical height, even quite dense, since no shadowing can then affect the direct impingement.

A number of studies have considered that both group III [96,97,124,125] and group V species [90,98] can be transferred to the NW sidewalls and to the droplet by *re-emission* of atoms initially landed on the substrate or on the neighbouring NWs, a process sometimes called secondary adsorption. Various assumptions have been made. The re-emitted current  $I_r$  of group III atoms was first calculated by Dalacu *et al.* [97] in the modelling of Au-catalysed InP NWs. However, only the current re-emitted from  $\text{SiO}_x$  mask to the sidewalls, with subsequent diffusion to the droplet over a migration length  $L_m$ , was considered. The authors also claimed that the droplet itself is subject to direct current only. Even though the NWs were grown in regular arrays, no dependence of the NW radius and length on the pitch was observed experimentally, and thus no mutual shadowing (*i.e.* shadowing of the NW by its neighbours) was discussed. The effect of the substrate shadowing by a NW itself, which subsequently affect the re-emitted current (*i.e.* the part of the substrate shadowed by a NW from the direct current cannot re-emit since no species had arrived to this area), was found negligible.

Kelrich *et al.* [126] adapted the model of Dalacu *et al.* to the case when a substrate area of a small radius around the NW is not covered by silica. Group III atoms, impinging there, are not scattered, but diffuse to the NW. Again, the NWs were grown in hexagonal arrays with various pitches, but here the authors included to their model a correction factor related to the mutual shadowing. In both these studies, the experimental results were fitted with the proposed model using the migration length  $L_m$  as a fitting parameter, albeit its value was not the same for similar growth conditions in Refs. [97,126]. In their experimental study of GaAs growth on non-patterned  $\text{SiO}_x/\text{GaAs}$  (111) substrate Rieger *et al.* [124] proposed that, especially in low density NW arrays, the re-emitted contribution of group III species to the NW sidewalls and to the catalyst droplet can be significant, without however providing a calculation of the re-emitted current.

As for group V species, although several studies [124,127] argued that the group V material (As in these cases) is primarily delivered to the droplet by direct impingement, Krogstrup *et al.* [125] suggested that it can also be re-emitted by the substrate, covered by  $\text{SiO}_x$ . Similarly, Ramdani *et al.* [98] showed a significant contribution to NW growth of As re-emission from the NW environment (*i.e.* substrate and neighbouring NWs), followed by adsorption by the droplet. The authors proposed that the re-emitted flux

is proportional to direct flux.

The idea of re-emitted contributions of both group III and group V species was revamped by Gibson and LaPierre [128], who extended the calculations of Dalacu *et al.* to the case of re-emission to the catalyst droplet. However, they considered the same substrate re-emission area for group III and group V species towards the sidewalls and the droplet. As we shall show in the next sections, this re-emission area is not a good assumption for the case of re-emission to the droplet. The experimental data were fitted by adjusting the 'incorporation coefficient', which characterizes the fraction of the species collected by the droplet or the sidewalls, that are used for NW growth.

The problem of the mutual shadowing in dense NW arrays was treated numerically using a 'line-of-sight' model [96, 126, 128, 129]. The reduction, due to shadowing, of the direct current reaching the substrate and then the sidewalls by re-emission primarily depends on the inclination angle  $\alpha$ , but also on the ratio between NW length and array pitch: the reduction becomes significant only if NW length exceeds the pitch, at least for  $\alpha$  around  $30^\circ$ . The re-emitted current from the substrate to the droplet is expected to exhibit the same behaviour, even it is shadowed significantly more. Oehler *et al.* [96] found such a flux of Ga to be negligible in comparison to direct one for NWs up to four times higher than the pitch.

As regards the angular distribution of the re-emission, most aforementioned studies [96, 97, 126, 128, 129] considered a Lambertian scattering of the arriving atoms, without however giving a physical justification. Only Oehler *et al.* [96] numerically tested the random uniform, Lambertian and specular distributions of re-emitted species reaching the NW sidewalls. The authors concluded that only specular reflection matches their experimental results, while the Lambertian re-emission provides an excessive amount of Ga. This disagrees with the results reported in Ref. [128]. This disagreement can be explained by the fact, that in the latter study the authors considered that not all the Ga, reached the droplet by re-emission, is used for the NW growth. To this end, they introduced the coefficient, which characterized the fraction of the material, arriving in the re-emitted current and used for the NW growth. This coefficient served as a fitting parameter (set to 0.35). On the contrary, the model of Oehler *et al.* does not involve any free parameter and uses only the NW geometry, deduced from the experiment.

As for sidewall *diffusion* current  $I_{dif}$ , that of group III is commonly taken into account in NW growth models [100, 130]. On the other hand, the surface diffusion of the volatile group V species is usually neglected [37, 39, 98, 131]. Several authors have nevertheless considered this possibility [69, 125, 132] and Krogstrup *et al.* [99] even estimated an As diffusion length of tens to hundreds of nm in the temperature range

400 – 800°C. In addition, Krogstrup *et al.* proposed that both group III and group V species can also diffuse out of the droplet with *back diffusion* current  $I_{bd}$ . The net sidewall diffusion current is hence a sum of the diffusion current towards the droplet and the back diffusion one (with the opposite sign).

The *desorption*  $I_{des}$  and *nucleation*  $I_n$  currents are widely considered in the NW growth modelling, and the corresponding calculations are performed by various authors [87, 88, 90, 133, 134].

To summarize, in contrast to direct impingement, desorption and nucleation currents, so far there is no analytical model for the re-emission current towards the catalyst droplet. The change of droplet volume may lead to the variation of the droplet surface, which intercepts the re-emitted flux, and also of the substrate re-emission area. Both of these effect will affect the re-emitted current to the catalyst. In addition, the role of the back diffusion, and its contribution to the material balance of the droplet, is not clear. To clarify these points, which may limit the control of droplet volume, in further section we revised the possible contribution of each term in Eq. (1.2) (page 8, Section 1.3 of Chapter 1). The droplet volume may be controlled by any change in the V/III ratio, but we limit our study of the dynamics of the droplet to the exposure to group V flux only (which means, at least,  $I_{dir,III} = I_{r,III} = 0$ ). Our study associates theory and experiment and clarifies the mechanisms of droplet consumption.

## 3.2 Experiments on partial droplet consumption

In order to observe the evolution of the droplet geometry, we performed a series of experiments of partial droplet consumption. Self-catalyzed GaP NWs were grown on patterned substrates by MBE. A 33 nm thick silica layer was formed on fully deoxidized intrinsic Si(111) wafers by chemical vapor deposition. The hexagonal pattern, which comprised several areas with pitches of 300, 400, 500 nm, 1 and 5  $\mu\text{m}$ , was transferred to the 33 nm thick silica layer, following the procedure described in Section 2.3.2 of Chapter 2. Each area contained holes with diameters from 30 to 70 nm. The samples were outgassed before growth in a separate chamber at 600°C and further outgassed *in situ* at 680°C.

Growth was performed at a substrate temperature of 600°C. To create catalyst droplets in the holes, Ga was deposited for 2 min. Ga and P<sub>2</sub> fluxes were then provided simultaneously for 20 min. The Ga flux was equivalent to a 2D growth rate of 0.144 nm s<sup>-1</sup> on (100) GaP, as measured by RHEED. During growth, the P<sub>2</sub> flux was adjusted to provide a V/III flux ratio equal to 1.3 (see Section 2.1.2 of Chapter 2

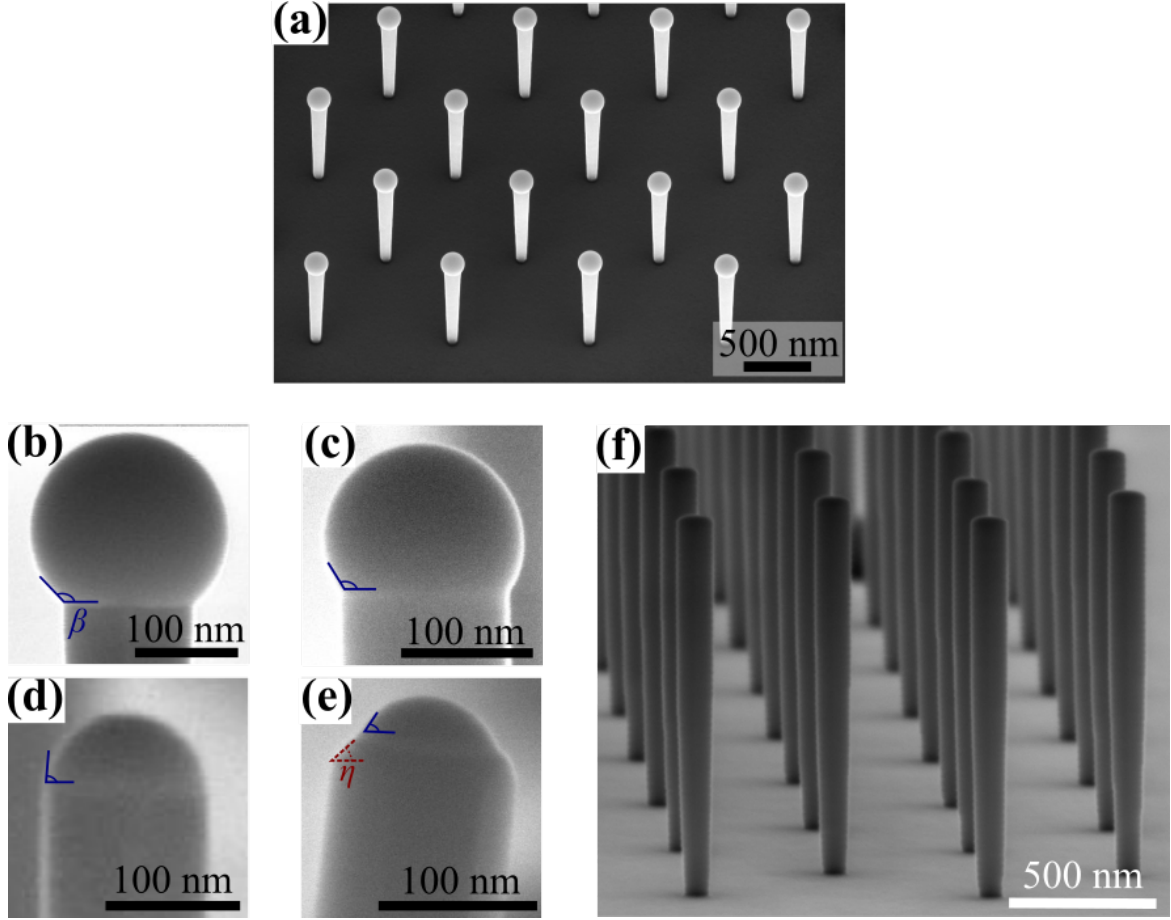


Figure 3.1: SEM images of GaP NWs (from arrays with  $1 \mu\text{m}$  pitch) after various times of droplet consumption. (a) General view of an array. The apical droplet immediately after growth (b) and after being consumed for 1 min (c), 2 min (d) and 2 min 20 s (e). Droplet contact angle  $\beta$  and tapering angle  $\eta$  of terminal section are indicated. (f) An array with totally consumed droplets.

for details). After growth, to consume the catalyst droplet, the Ga flux was abruptly switched off and the sample was exposed to  $\text{P}_2$  only, the atomic flux of phosphorous being set to a V/III ratio of 3, *i.e.*  $1.07 \times 10^{19}$  at  $\text{m}^{-2} \text{s}^{-1}$ . The experiment was terminated by closing all shutters and valves abruptly, and turning off the oven for rapid cooling. The duration of exposure to phosphorous was varied between 1 min and 3 min in order to study the progression of the catalyst droplet consumption.

Before droplet consumption, our arrays of as-grown NWs are of high quality (Figure 3.1(a)). Growth occurs in all openings. In a small fraction of these, we find 3D crystallites. All the others are occupied by single vertical NWs. Table 3.1 indicates how the geometrical parameters of the NWs and their dispersion vary with pitch. No significant difference is observed for the largest pitches of 1 and  $5 \mu\text{m}$ . The NWs are slightly back-tapered, their radius varying from 40-45 nm at the bottom to 55-60 nm at the top over a length of about 700 nm (Figure 3.1(a))

Figure 3.1(b) to (f) illustrates the droplet geometry on the top of the NWs, extracted from an area with a pitch of 1  $\mu\text{m}$ , after different times of consumption by exposure to phosphorus. The consumption rate is not the same for all pitches. In arrays with pitches of 500 nm and less, the droplets are consumed more slowly than those in the arrays with larger pitches. However, similarly to what we found for the as-grown NWs, we observed only very little difference in the droplet consumption rate for the pitches of 1  $\mu\text{m}$  and larger. This indicates an influence of neighbouring NWs in dense arrays and the absence of interaction in arrays with distant NWs. This can be related to the small inclination angle  $\alpha = 17^\circ$  of the P source with respect to the substrate normal, which restricts shadowing to the close neighbourhood of each NW. We shall show that a significant amount of phosphorous reaches the droplet after being re-emitted from the neighbouring surfaces, so that the presence of the NWs close by could have a strong influence on this flux. The impact of the neighbouring NWs, which was studied in detail by Oehler *et al.* [96] in the context of growth, was not studied in the present work. Instead, we focus on large pitches and model a single NW isolated on its substrate.

Table 3.1: Measured morphologies of self-catalysed GaP NWs grown in arrays with various pitches.  $H_{NW}$ : NW height,  $R_{NW}$ : top NW radius,  $\beta$ : droplet contact angle.

Pitch (nm)	300	400	500	1000	5000
$H_{NW}$ (nm)	$655 \pm 19$	$680 \pm 21$	$705 \pm 22$	$725 \pm 20$	$726 \pm 22$
$R_{NW}$ (nm)	$47 \pm 2$	$50 \pm 2$	$53 \pm 2$	$58 \pm 3$	$60 \pm 2$
$\beta$ ( $^\circ$ )	$138 \pm 2$	$138 \pm 2$	$137 \pm 2$	$137 \pm 2$	$137 \pm 2$

The droplet geometry is described by two parameters which may change over time, namely its contact angle  $\beta$  and its base radius. Initially,  $\beta$  is around  $137^\circ$  independently of the NW radius (Figure 3.1(b), Table 3.1). During consumption, as long as  $\beta$  remains larger than  $90^\circ$ , the droplet keeps a base radius equal to the NW radius (Figure 3.1(c)). Once the contact angle reaches  $\beta \simeq 90^\circ$  (Figure 3.1(d)), the NW tapers via the creation of sidewall facets tilted by angle  $\eta \simeq 47^\circ$ , a value close to that measured *in situ* by Panciera *et al.* [93] for GaAs during droplet manipulation (this tapering is much more pronounced than during stem growth and in the opposite direction). The droplet remains pinned to the edge of these facets, so that its base shrinks in a known fashion while the contact angle keeps decreasing (Figure 3.1(e)). We did not observe any contact angle below  $63^\circ$ . This value is close to the Young's angle  $\beta_Y \simeq 65^\circ$  for a pure Ga liquid droplet on a GaP (111) surface [135]. After the droplet adopts the Young's contact angle, it depins from the tilted facets, its base diameter shrinks further until it disappears completely (Figure 3.1(f)). The tapering at the top of the NW is

clearly visible in Figure 3.1(e) but absent from Figure 3.1(f), after complete droplet consumption. This is probably due to the radial growth which fills in the taper and restores vertical facets.

### 3.3 Analytical calculation of the various contributions to droplet consumption

To describe the dynamics of the droplet geometry during crystallization, we develop calculations taking into account four possible channels of droplet consumption under exposure to the sole group V species (Figure 3.2). Three channels correspond to different currents of phosphorus to the droplet that consume gallium by forming solid GaP. Phosphorus atoms can indeed be delivered to the droplet by direct impingement of the beam (i), or after re-emission from the substrate (ii) or via surface diffusion of adatoms deposited on the substrate or on the sidewalls (iii). This third pathway is usually deemed ineffective for group V elements. This three pathways also operate during NW growth, and they constitute the left side of Eq. (1.2) (page 8, Section 1.3 of Chapter 1). In addition, the droplet volume may decrease due to back diffusion of Ga atoms along the sidewalls towards the base of the NW; this constitutes our fourth (iv) channel. Finally, both Ga and P can leave the droplet due to desorption (v).

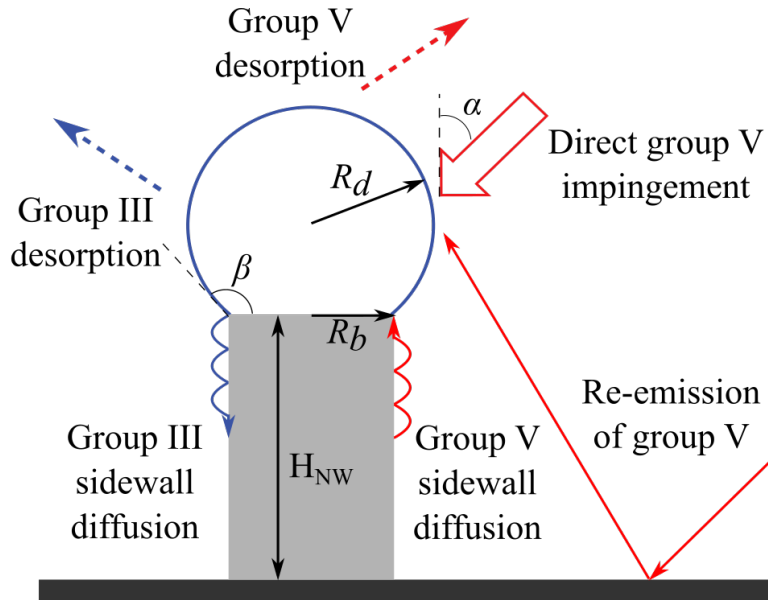


Figure 3.2: Schematics of the material currents contributing to the consumption of a droplet located on top of an isolated III-V NW. Here,  $R_b = R_{NW}$ .

To calculate the currents contributing to the consumption, we consider an axisymmetric NW isolated on an infinite substrate. The apical droplet is a spherical cap with

contact angle  $\beta$ , radius  $R_d$  and base radius  $R_b = R_d \sin \beta$  and the NW stem a right circular cylinder with radius  $R_{NW}$  and height  $H_{NW}$  (Figure 3.2). As long as the droplet remains pinned to the sidewalls,  $R_b = R_{NW}$ . The whole system is exposed to a  $P_2$  molecular beam (at angle  $\alpha$ ), yielding an atomic P flux  $F_e$  per unit area of substrate.

### 3.3.1 Direct impingement

The direct current  $I_{dir}$  is calculated following Glas [123]. It depends on droplet geometry and on the material source inclination angle  $\alpha$ :

$$I_{dir} = \pi R_d^2 \frac{F_e}{\cos \alpha} \varepsilon(\alpha, \beta) \quad (3.1)$$

Here,  $\varepsilon(\alpha, \beta)$  describes the cross-section of the droplet which intercepts the direct flux and its variation with the contact angle  $\beta$  during the consumption.

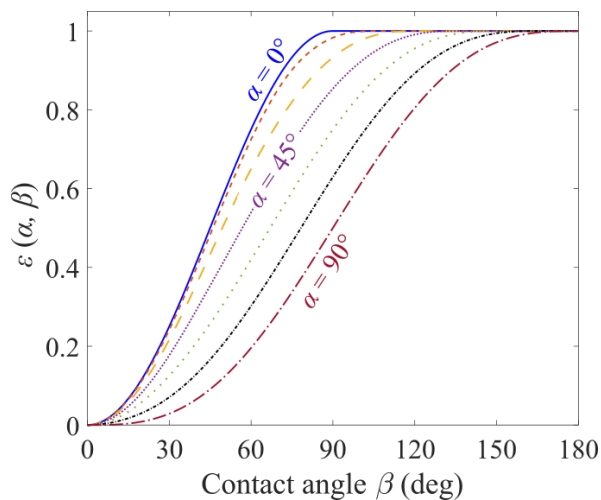


Figure 3.3: Variations of term  $\varepsilon(\alpha, \beta)$ , which characterizes the beam area intercepted by the droplet, normalized by the droplet section, as a function of the droplet contact angle. Each curve pertains to a particular beam incidence angle  $\alpha$ , by steps of  $15^\circ$ .

Figure 3.3 shows the variation of  $\varepsilon(\alpha, \beta)$  as a function of droplet contact angle  $\beta$ . For source inclination angles  $\alpha < 45^\circ$ , which is a range used in most of MBE setups, the direct current reaches its maximum (*i.e.* the intercepted area is  $\pi R_d^2$ ) for a droplet with contact angle around  $90^\circ$ .

### 3.3.2 Re-emission

We now calculate the re-emission of the group V species, initially proposed by Krogstrup *et al.* [125] and later considered by Ramdani *et al.* [98] and Gibson and LaPierre [128].

Here, for our isolated GaP NW, we consider re-emission of phosphorous from the substrate only. The absence of deposit on the mask indicates that all P species that reach it are actually re-emitted.

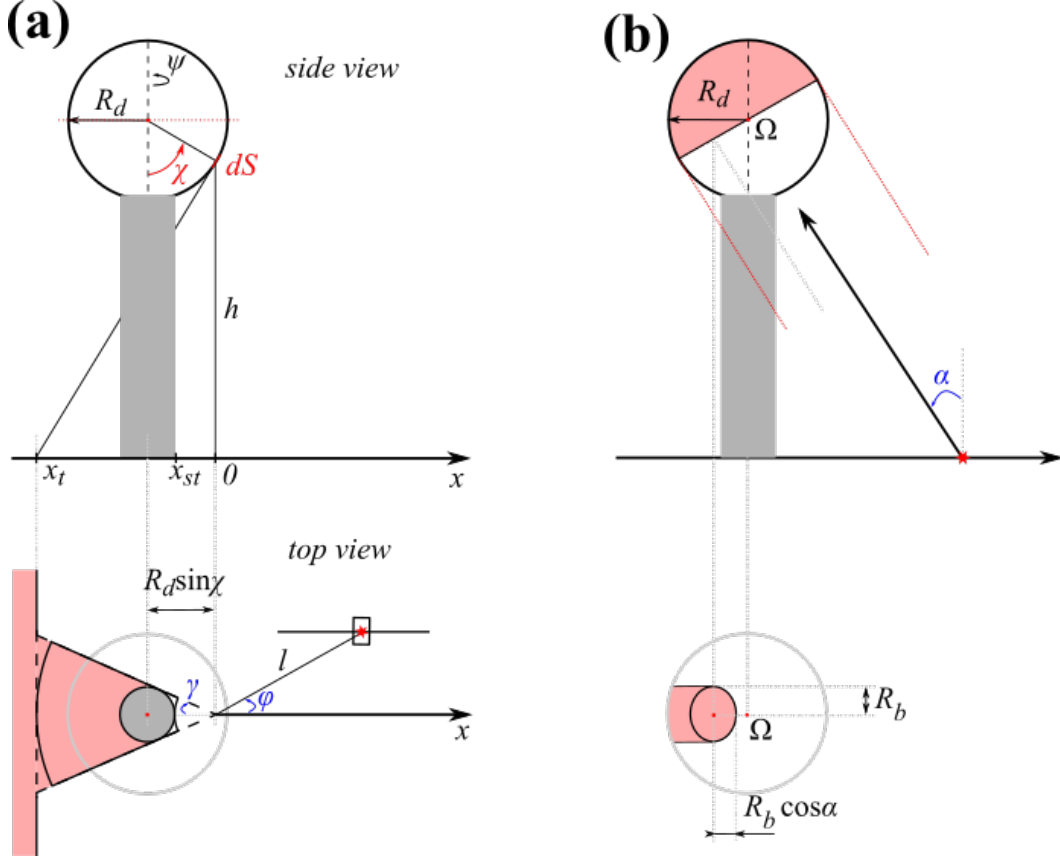


Figure 3.4: Geometry for the calculation of the currents re-emitted towards the droplet. Red stars mark the position of a substrate re-emitter. (a) Lambertian re-emission. In the top view, pink shading shows the substrate area shadowed by the NW stem for element  $dS$  of lower hemisphere in corresponding side view. Full and dashed lines border the integration domains used in approximations (1) and (2) of shadowing, respectively. (b) Specular re-emission for  $\beta \geq \pi/2$ . Pink shading shows part of spherical cap not visible from substrate re-emitters (top) and projection of NW stem within great circle normal to re-emitted beam (bottom).

To calculate the total re-emitted current  $I_r$ , we first consider a fixed surface element  $dS$  on the spherical cap at polar angle (latitude)  $\chi$ , azimuthal angle  $\psi$  and height  $h = H_{NW} - R_d(\cos \beta + \cos \chi)$  above the substrate (Figure 3.4(a), side view), and we sum the contributions to  $dS$  of all re-emitters on the substrate. Taking an origin at projection  $O$  of  $dS$  on the substrate, the position of a re-emitter is measured either in Cartesian coordinates (with axis  $x$  passing by the centre of the NW) or in polar coordinates  $(l, \varphi)$  (Figure 3.4(a), top view). We call  $\Phi(\theta, \varphi)$  the current re-emitted per unit area of substrate and unit solid angle, in direction defined by in-plane and

out-of-plane angles  $\varphi, \theta$ . In general, this distribution depends on the beam incidence angle  $\alpha$ . The total re-emitted current received by  $dS$  writes:

$$dI_r = \int_{A_{sub}} \Phi(\theta, \varphi) d\Omega dA_{sub} \quad (3.2)$$

In Eq. (3.2), the integral extends over the substrate area  $A_{sub}$  from which surface element  $dS$  is visible and  $d\Omega$  is the solid angle subtended by  $dS$  from the emitter position:

$$d\Omega = \frac{l \cos \varphi \sin \chi + h \cos \chi}{(l^2 + h^2)^{\frac{3}{2}}} dS \quad (3.3)$$

In our isolated NW approximation, we neglect the shadowing of the substrate by the other NWs as well as re-emission by their sidewalls and we can perform the calculation for a given incident beam direction, even though the substrate rotates during the experiments. The total re-emitted current  $I_r$  is then found by integrating  $dI_r$  over the spherical cap:

$$I_r = R_d^2 \int_0^{2\pi} d\psi \int_{\pi-\beta}^{\pi} \frac{dI_r}{dS} \sin \chi d\chi. \quad (3.4)$$

with  $dI_r/dS$  given by Eqs. (3.2) and (3.3).

To calculate  $I_r$ , we need to specify the *a priori* unknown angular distribution of re-emission. We fully test two hypotheses, already considered for various purposes in the literature, namely the Lambertian (cosine) distribution [96, 97, 128] and specular reflection [96, 98]. In the former case, the phosphorous species are re-emitted independently of their incidence angle. In the latter, they are reflected by the substrate at an angle equal to their fixed incidence angle  $\alpha$ . These are two extreme cases: specular re-emission corresponds to a purely mechanical interaction with the substrate whereas a Lambertian distribution is expected for molecules having reached equilibrium with it [136, 137]. In both cases, we assume that re-emission occurs at the point of incidence, thereby neglecting surface diffusion on the mask.

### Lambertian re-emission

Let us thus first consider the Lambertian case (superscript  $L$ ), for which

$$\Phi^L(\theta, \varphi) = \frac{F_e}{\pi} \cos \theta \quad (3.5)$$

Calculating  $dI_r^L$  from Eq. (3.2) requires specifying area  $A_{sub}$ . Element  $dS$  is exposed

to all substrate re-emitters except those blocked by the droplet itself or by the NW stem. Droplet blockage is simply set by the intersection with the substrate of the plane tangent to the droplet at  $dS$ : this limits re-emission to half-plane  $x \geq x_t$ , with  $x_t = -h \cot \chi$  the abscissa of the intersection (Figure 3.4(a)). Integration over this half plane using Eq. (3.3) and angular distribution (3.5) yields

$$dI_r^L = \frac{F_e}{2} (1 + \cos \chi) dS \quad (3.6)$$

As regards blocking of re-emission by the NW stem, in what follows, we limit ourselves to a droplet pinned to the TPL ( $R_b = R_{NW}$ ). According to our experiments, this covers by far the largest part of the consumption process, since the droplet depins only when its contact angle decreases to the Young's angle value. Then, for a surface element  $dS$  in the "northern" hemisphere of the droplet ( $\chi \geq \frac{\pi}{2}$  when  $\beta \geq \frac{\pi}{2}$ ,  $\chi \geq \pi - \beta$  when  $\beta \leq \frac{\pi}{2}$ ) there is no extra shadowing by the NW stem. In particular, when  $\beta \leq \frac{\pi}{2}$ , with only a partial northern hemisphere (and no southern hemisphere), integration of the elementary currents over the droplet surface simply gives

$$I_r^L = \frac{\pi}{2} F_e R_d^2 (1 - \cos \beta)^2 \quad (3.7)$$

When  $\beta \geq \frac{\pi}{2}$  and  $dS$  lies in the "southern" hemisphere ( $\pi - \beta \leq \chi \leq \frac{\pi}{2}$ ), stem shadowing depends on the position of the tangent plane. If  $x_t \geq x_{st}$ , with  $x_{st} = R_d (\sin \beta - \sin \chi)$  the abscissa of the NW edge (Figure 3.4(a)), there is none. However, in the usual case of slender NWs ( $H_{NW} \gg R_{NW}$ ) with  $\beta$  not too close to  $\pi$ , most surface elements are such that  $x_t < x_{st} - 2R_{NW}$  and the stem blocks re-emission from the shaded trapezoidal domain drawn in Figure 3.4(a) (top view), where  $\gamma = \arcsin(\sin \beta / \sin \chi)$ .

Underestimates and overestimates of this contribution, to be subtracted from  $dI_r^L$ , can be obtained analytically by approximating this domain. Writing this contribution as  $F_e \delta_i dS/2$ , Eq. (3.6) becomes;

$$dI_r^L = \frac{F_e}{2} (1 + \cos \chi - \delta_i) dS \quad (3.8)$$

with  $\delta_i = 0$  for  $\chi \geq \pi/2$ . The total re-emitted current now writes

$$I_{r,i}^L = \frac{\pi}{2} F_e R_d^2 [(1 - \cos \beta)^2 - I_i] \quad (3.9)$$

In Eqs. (3.8) and (3.9)  $i$  indexes various approximations of the integration domain  $A_{sub}$ . This domain can in particular be approximated as (1) the area limited by the

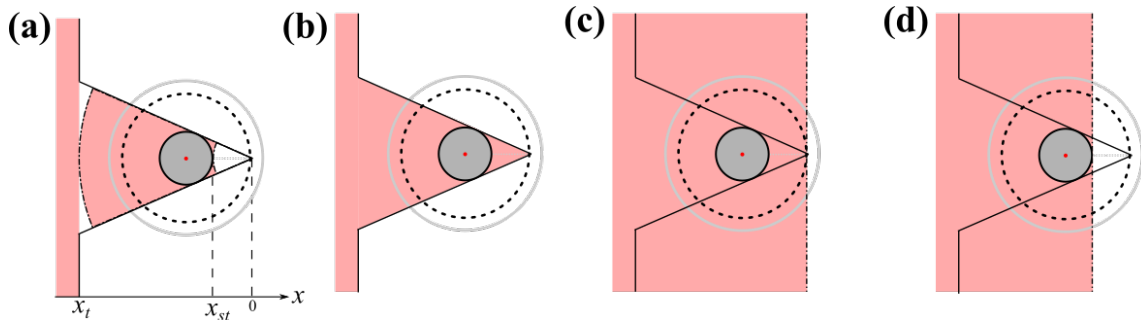


Figure 3.5: Schematics of the integration domain  $A_{sub}$  used in calculation of  $I_r^L$  within approximations (1) (a), (2) (b) and (3) (c), and that considered in Ref. [128] (d). Full grey circle shows the projection of the droplet on the substrate, the black dashed circle - that of the horizontal circumference on which the element  $dS$  lies. Grey filling shows the area under the NW stem. Pink filling shows the substrate areas excluded from integration in the various approximations.

arcs drawn in Figures 3.4(a) (top view) and 3.5(a), or (2) the triangle with apex at O extending to  $x_t$  (Figure 3.5(b)), respectively. Within approximation (1), we find:

$$\delta_1 = \delta_1^{(0)} + \delta_1^{(1)} \quad (3.10)$$

with

$$\delta_1^{(0)} = \frac{2}{\pi} \left[ \sin \beta \left( \chi - \frac{\pi}{2} + \sin \chi \cos \chi \right) + \gamma \cos^3 \chi \right] \quad (3.11)$$

$$\delta_1^{(1)} = \frac{2}{\pi} \left[ \sin \beta \left( \arctan \rho - \frac{\rho}{1 + \rho^2} \right) - \frac{\rho^2}{1 + \rho^2} \gamma \cos \chi \right] \quad (3.12)$$

and  $\rho(\chi) = |x_{st}|/h$  with  $h = H_{NW} - R_d(\cos \beta + \cos \chi)$ . For  $\rho \ll 1$ ,  $\delta_1 \simeq \delta_1^{(0)}$ . We then obtain the total re-emitted current  $I_{r,1}^L$  intercepted by the droplet by integrating the elementary currents (by doing so, we include spurious negative contributions (when  $x_t > x_{st}$ ), but these are very small and do not alter the fact that  $\delta_1$  slightly underestimates stem blockage). We find:

$$I_{r,1}^L = \frac{\pi}{2} F_e R_d^2 \left[ (1 - \cos \beta)^2 - I_1 \right] \quad (3.13)$$

In the bracket, the first term originates from Eq. (3.6) and  $I_1$ , due to re-emission blockage by the NW stem, writes:

$$I_1 = \frac{4}{\pi} \left[ \frac{4}{3} \sin \beta - \left(1 + \frac{\pi}{4}\right) \sin^2 \beta + \left(\frac{\pi}{8} - \frac{1}{3}\right) \sin^4 \beta + \frac{1}{4} (\pi - \beta) \right. \\ \left. + \sin \beta \cos \beta \left( \beta - \frac{\pi}{2} + \frac{1}{6} \sin^2 \beta - \frac{5}{12} \right) \right] + J_1 \quad (3.14)$$

with

$$J_1 = 2 \int_{\pi-\beta}^{\frac{\pi}{2}} \delta_1^{(1)}(\chi) \sin \chi d\chi \quad (3.15)$$

The term  $J_1$  depends on the ratio  $R_d/H_{NW}$  through  $\rho$ . Figure 3.6(a) shows its variation as a function of  $\beta$  for several values of  $R_d/H_{NW}$ . This term appears to be small with respect to  $I_1$  even for  $R_d = H_{NW}$  (although such a 'structure' can hardly be called a NW). For fully grown NWs, when  $R_d/H_{NW} \ll 1$ , which is the case in our experiments,  $J_1$  is negligible.

Within approximation (2), integration over the triangular domain (Figure 3.5(b)), for each element  $dS$ , can be performed exactly and yields:

$$\delta_2 = \frac{2}{\pi} \left[ \arctan(\tan \gamma \cos \chi) - \sin \beta \arctan \frac{1}{\tan \chi \cos \gamma} \right] \quad (3.16)$$

Summation over the spherical cap finally gives:

$$I_{r,2}^L = \frac{\pi}{2} F_e R_d^2 [(1 - \cos \beta)^2 - I_2] \quad (3.17)$$

with

$$I_2 = 2 \left[ 1 - \frac{2\beta}{\pi} - \cos \beta + \left(1 - \frac{2}{\pi}\right) \sin \beta \cos \beta \right] \quad (3.18)$$

Finally, a simpler but rougher approximation (3) is obtained by excluding, for each element  $dS$ , re-emission from the whole band located between the traces of the tangent plane and of the vertical passing at  $dS$  (Figure 3.5(c)). This yields

$$I_{r,3}^L = \frac{\pi}{2} F_e R_d^2 [(1 - \cos \beta)^2 - I_3] \quad (3.19)$$

with

$$I_3 = \pi/2 - \beta + \cos \beta (\sin \beta - 2). \quad (3.20)$$

An even coarser approximation (4) was proposed by Gibson and LaPierre [128] who limited re-emission to half plane  $x \geq x_{st}$  whatever the point on the sphere (Figure

3.5(d)). This approximation gives us the correction  $I_4$ .

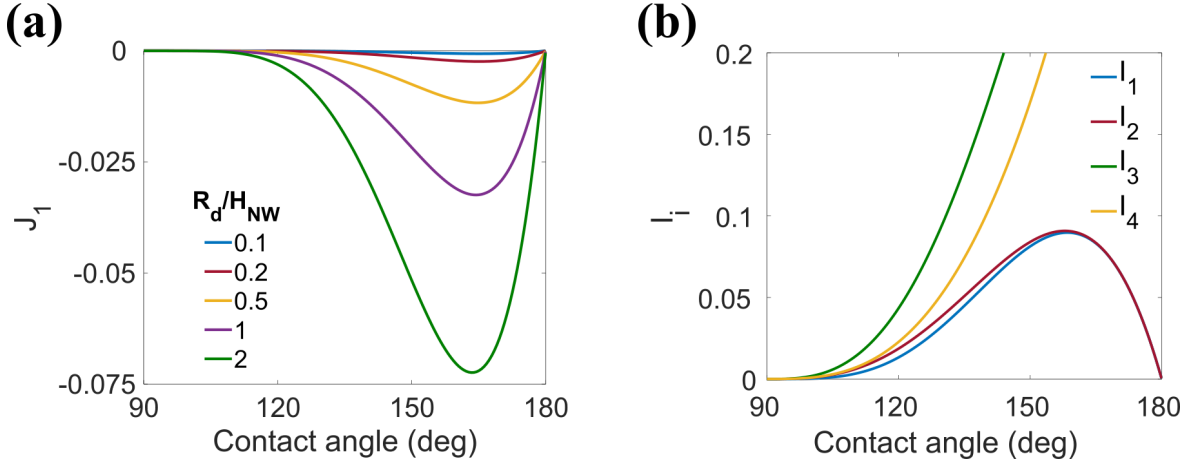


Figure 3.6: Variation with contact angle  $\beta$  of terms (a)  $J_1$  (Eq. 3.15) for several values of  $R_d/H_{NW}$  and (b)  $I_1$  (Eq. (3.14)),  $I_2$  (Eq. (3.18)),  $I_3$  (Eq. (3.20)) and  $I_4$  [128], which correct Lambertian re-emission for stem blockage.

Figure 3.6(b) compares the absolute values of corrections  $I_1$ ,  $I_2$ ,  $I_3$  and  $I_4$  as a function of contact angle. The rough corrections  $I_3$  and  $I_4$ , are close to  $I_1$  and  $I_2$  for  $\beta$  around  $90^\circ$ , but for larger  $\beta$  they give values 2-3 times higher, which leads to significantly underestimate of the re-emitted current  $I_r^L$ . On the contrary, the closeness of  $I_1$  and  $I_2$  for any  $\beta$  is very satisfactory, since they yield an overestimate and an underestimate of the re-emitted current, respectively. Hence, the real current, which seats in between, is approximated very well by either. On the other hand, these corrections may amount to more than 10% of the total for contact angles on the order of those encountered at the start of consumption (Figure 3.6(b)), which makes them necessary.

### Specular re-emission

In the case of specular re-emission (superscript  $S$ ), the species are reflected at an angle equal to the material source inclination angle  $\alpha$  (see Figures 2.1 and 3.2). The re-emitted current is then easily calculated by projecting the droplet-stem assembly in the plane normal to the re-emission direction, passing through the drop centre (Figure 3.4(b)). In this plane, a full spherical droplet projects as a circle of radius  $R_d$ , from which must be subtracted the area shadowed by the NW stem. The top surface of the stem projects as an ellipse with semi-axes  $R_b$  and  $R_b \cos \alpha$  and the NW shadow is generated by translating this ellipse along its short axis (Figure 3.4(b), bottom).

When  $\beta \geq \pi/2$ , the elliptical projection of the top surface of the stem is entirely enclosed in the circle of radius  $R_d$ . The area to be subtracted is then the union of a half-ellipse, a rectangle and a circular sector (Figure 3.4(b), bottom). When

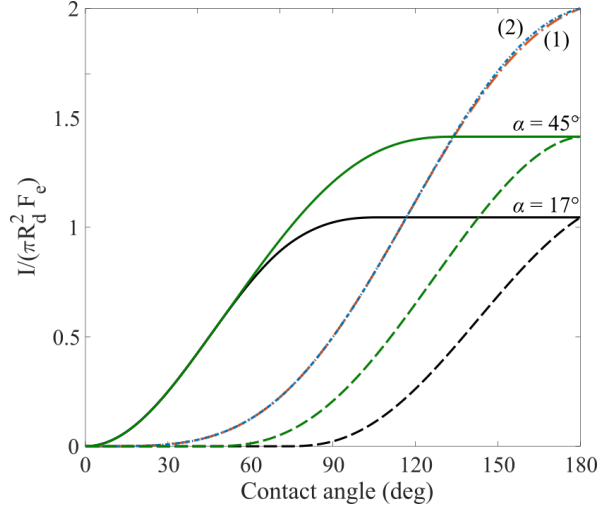


Figure 3.7: Currents of group V species collected by the droplet as a function of its contact angle  $\beta$ : direct contribution (full curves) and re-emission in the specular (dashes) or Lambertian (dash-dots) cases. Direct and specularly re-emitted currents are given for the two incident beam angles  $\alpha = 17^\circ$  (black) and  $\alpha = 45^\circ$  (green). Lambertian re-emission is calculated within approximations (1) (loose dash-dots, in red) and (2) (dense dash-dots, in blue). All currents are normalized by sphere section  $\pi R_d^2$  and material source flux  $F_e$ .

$\pi/2 - \alpha \leq \beta \leq \pi/2$ , the droplet projects as a circular segment and we have contributions only from the small area between its circular rim and the elliptical projection of the NW top facet. Finally, when  $\beta \leq \pi/2 - \alpha$ , the stem blocks the reflected beam entirely. The calculation of the various areas involved yields the following re-emitted current:

$$I_r^S = \frac{F_e R_d^2}{\cos \alpha} \begin{cases} \beta + \sin \beta \cos \beta (1 - 2 \sin \alpha) - \frac{\pi}{2} \cos \alpha \sin^2 \beta & \text{for } \beta \geq \frac{\pi}{2}; \\ \frac{\pi}{2} - \cos \beta \sqrt{\sin^2 \alpha - \cos^2 \beta} - \sin^2 \beta \cos \alpha \arccos(\cot \alpha \cot \beta) \\ - \arcsin \frac{\cos \beta}{\sin \alpha} & \text{for } \frac{\pi}{2} - \alpha \leq \beta \leq \frac{\pi}{2}; \\ 0 & \text{for } \beta \leq \frac{\pi}{2} - \alpha. \end{cases} \quad (3.21)$$

Figure 3.7 gives the variations of the direct and re-emitted currents calculated in the Lambertian and specular cases, as a function of the droplet contact angle  $\beta$ , for the  $P_2$  beam incidence  $\alpha = 17^\circ$  pertaining to our experiments, and for arbitrary incidence  $\alpha = 45^\circ$ , for comparison. Our two analytical approximations of Lambertian re-emission to the droplet, namely Eqs. (3.13)-(3.14) with  $J_1 = 0$  and Eqs. (3.17)-(3.18), give very close results. For specificity, in our further analysis, we shall use approximation (1).

### 3.3.3 Contribution of surface diffusion to droplet consumption

In our experiments, the contact angle and the droplet radius (symbols in Figure 3.11) decrease more rapidly than in calculations where we take into account only direct impingement and re-emission, whether Lambertian or specular. These two currents do not provide enough phosphorous to consume the droplet and the missing amount is significant.

We are thus led to consider the two extra channels of Ga consumption mentioned in the introduction of Section 3.3. The first one consists in a third P current into the droplet, due to migration up the sidewalls [69, 125, 132]. The second extra consumption channel does not involve phosphorous, but diffusion of Ga atoms out of the droplet [99]. Both processes can take place simultaneously.

To obtain the phosphorous diffusion current, we introduce a surface diffusion length  $\lambda_V$  and simply assume that all atoms impinging the sidewalls within a distance  $\lambda_V$  below the TPL are transferred to the droplet. This assumes that  $H_{NW} > \lambda_V$ , which also excludes any contribution from diffusion on the substrate. We thus only need to calculate the direct and re-emitted currents collected by the sidewalls.

The direct current is simply that intercepted by a vertical rectangle of width  $2R_{NW}$  and height  $\lambda_V$ , namely  $I_{dir} = 2F_e R_{NW} \lambda_V \tan \alpha$ . In case of specular reflection, the re-emitted current is the same, which gives a total P diffusion current

$$I_{dif}^S = 4F_e R_{NW} \lambda_V \tan \alpha \quad (3.22)$$

For Lambertian re-emission, all surface elements  $dS$  of the NW at a given height  $z$  are equivalent and receive phosphorous from the whole half plane bounded by the intersection with the substrate of the vertical plane tangent to the NW at  $dS$ . Integration on this half plane is the same as performed previously in the context of NW heating by Glas and Harmand [138] and yields current  $F_e dS/2$ , irrespective of  $z$ . The collecting area being  $2\pi R_{NW} \lambda_V$ , the diffusion current is

$$I_{dif}^L = F_e R_{NW} \lambda_V (2 \tan \alpha + \pi) \quad (3.23)$$

Dalacu *et al.* [97] repeated the calculation of Glas and Harmand [138] (in the context of material re-emission) and obtained the same result.

Finally, we turn to Ga back diffusion out of the droplet. To calculate this current, we use the transition state approach developed for NW growth by Krogstrup *et al.* [99]. The net group III current is the difference of the currents entering and leaving the droplet. The current entering the droplet is proportional to the density of Ga adatoms

on the sidewalls, just below the TPL, and depends exponentially on their chemical potential (measured with respect to the transition state energy). However, due to the lack of external Ga supply during droplet consumption, density and hence chemical potential are expected to be low. We thus consider only the reverse transition liquid  $\rightarrow$  adatom. The corresponding back-diffusion flux per unit length of TPL can be written

$$F_{bd} = B(T) x_{Ga} \exp\left(\frac{\mu_{l,Ga}}{k_B T}\right). \quad (3.24)$$

with  $x_{Ga}$  the atomic fraction and  $\mu_{l,Ga}$  the chemical potential of Ga in the droplet, and  $B$  a prefactor depending on the Ga frequency of attempt to cross the TPL and on the energy barrier. We write as usual  $\mu_{l,Ga}(x_{Ga}, T) = \mu_{l,Ga}^\infty(x_{Ga}, T) + \mu_{GT}$ , where the first term pertains to the infinite liquid phase and  $\mu_{GT}$  is a Gibbs-Thomson (GT) correction accounting for the small size of the droplet. In VLS growth, the group V concentration in the droplet is extremely low, and we expect the concentration of P in Ga to be even lower than that of As [40, 90, 101]. Thus,  $x_{Ga}$  is very near unity and  $\mu_{l,Ga}^\infty$  very close to the chemical potential of pure Ga. Then, apart from the GT term, we can group all the terms in Eq. (3.24) in a factor  $A(T) = B(T) \exp(\mu_{l,Ga}^\infty(1, T)/(k_B T))$  that depends only on temperature. Straightforward integration over the TPL yields the back diffusion current:

$$I_{bd} = 2\pi R_b A(T) \exp\left(\frac{\mu_{GT}}{k_B T}\right) \quad (3.25)$$

The GT correction is  $\mu_{GT} = \gamma_l \partial S_d / \partial N_l$ , with  $\gamma_l$  the surface tension of liquid Ga,  $N_l = \pi R_d^3 (1 - \cos \beta)^2 (2 + \cos \beta) / (3\omega_{Ga}^L)$  the number of (Ga) atoms, of atomic volume  $\omega_{Ga}^L$ , in the droplet and  $S_d = 2\pi R_d^2 (1 - \cos \beta)$  the surface area of the droplet. Since the droplet does not keep a fixed shape,  $\mu_{GT}$  must be evaluated at each step of the consumption process.

### 3.3.4 Desorption of P and Ga from the droplet

The liquid droplet continuously loses its two constituents by desorption. A fraction of the P atoms brought to the droplet by channels (i) to (iii) is thus lost for the formation of GaP. This reduces the rate of droplet consumption. On the opposite, Ga desorption obviously speeds up consumption. These two effects thus somehow compensate each other. However, we need to make sure that they are sufficiently weak to justify being omitted in our calculations. All evaluations are performed at a temperature of 600°C.

The P desorption current  $I_{des}$  is calculated as in the analysis by Glas *et al.* of the

self-catalyzed growth of GaAs NWs [90]. When one molecular species  $P_n$  dominates all the others, it is simply:

$$I_{des,P} = \frac{k_e n p_n S_d}{\sqrt{2\pi n M_{at} k_B T}} \quad (3.26)$$

with  $k_e \leq 1$  the Knudsen evaporation coefficient,  $S_d$  the droplet area,  $M_{at}$  the mass of a P atom and  $p_n$  the equilibrium pressure of species  $P_n$  with the liquid (extension to multiple vapor species is straightforward). At given temperature  $T$ , and neglecting small size effects,  $p_n$  depends only on the atomic concentration  $x_V$  of phosphorous in the droplet, which is unknown. We thus evaluate  $I_{des,P}$  for two arbitrary values of  $x_V$ , namely the concentration  $x_{eq}$  at equilibrium with GaP (surely an underestimate) and  $x = 3x_{eq}$  (a reasonable supersaturation, as judged from the case of GaAs [90]). Extending the calculations from GaAs [90] to GaP, using the appropriate thermodynamic data [139, 140], we first find that at our growth temperature of 600°C, the species having by far the highest vapor pressure, is  $P_2$  and that  $x_{eq} \simeq 8 \times 10^{-5}$  [141, 142], with  $p_2(x_{eq}) \simeq 5.3 \times 10^{-7}$  Pa. For our NWs with  $R_{NW} = 60$  nm (and in the worst possible case of  $k_e = 1$ ), this gives  $I_{des}$  varying from about 190 to 1000 at  $s^{-1}$  for contact angles spanning our experimental range (65 – 137°). The current is about 9 times larger for  $x = 3x_{eq}$  (Figure 3.8). As will be shown in Section 3.5, these currents are small with respect to the sum of those calculated for our four main pathways (i) to (iv).

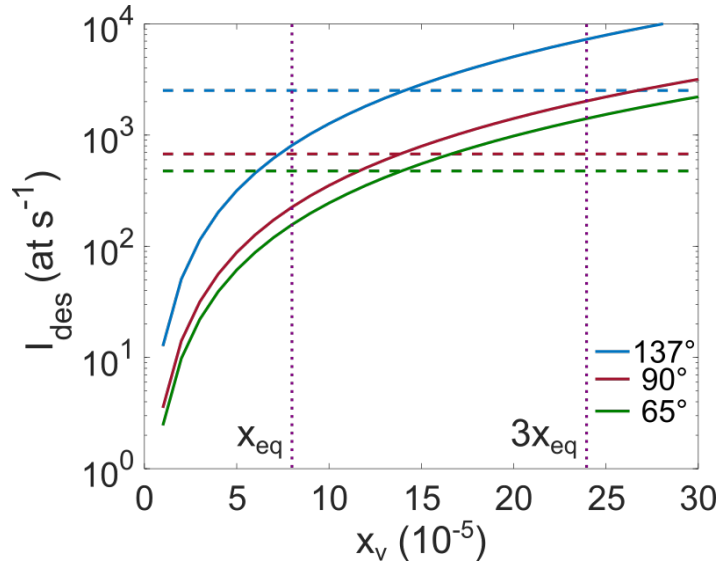


Figure 3.8: Desorption currents  $I_{des,P}$  (solid curves) and  $I_{des,Ga}$  (dashed lines) for selected values of contact angle  $\beta$ , as a function of phosphorous atomic concentration  $x_V$  in the droplet. The vertical lines mark the concentration  $x_V = x_{eq}$ , at which the liquid droplet and solid GaP are in equilibrium, and  $x_V = 3x_{eq}$ .

The corresponding current  $I_{des,Ga}$  is calculated in the same way, now considering

only the desorption of atomic Ga. The droplet being nearly pure Ga, the equilibrium pressure  $p_{Ga}$  is virtually independent of  $x_V$ . Using the same thermodynamic data, we find that  $p_{Ga} \simeq 2.8 \times 10^{-6}$  Pa, yielding  $I_{des,Ga}$  varying from about 510 to 2700 at  $s^{-1}$  over our range of contact angles (dashed lines in Figure 3.8).

Since  $I_{des,P}$  and  $I_{des,Ga}$  are of the same order but have opposite effects on consumption, as noticed before, they compensate each other efficiently. By calculating their difference, we find that the rate of droplet consumption is slightly increased for  $x = x_{eq}$ , by amounts ranging from 320 to 1700 at  $s^{-1}$ , and slightly decreased for  $x = 3x_{eq}$ , by amounts ranging from 1200 to 6400 at  $s^{-1}$ , the extreme figures still corresponding to our extreme contact angles. These figures confirm that, as far as droplet consumption is concerned, the joint desorption of P and Ga can be neglected as compared to pathways (i) to (iv), which together give a current of the order of  $10^5$  at  $s^{-1}$  (see Section 3.5).

### 3.4 Axial and radial growth during consumption - Experimental determination of the unknown model parameters

Our model includes two unknown parameters, namely the P diffusion length  $\lambda_V$  and prefactor  $A(T)$  for Ga back diffusion. To estimate these parameters, we devised complementary experiments based on the following remarks. During consumption, the Ga atoms lost by the droplet can either generate an axial solid volume  $V_{ax}$  by VLS growth, or diffuse to the sidewalls to form a radial volume  $V_{rad}$  by VS growth (Figure 3.9). Since the droplet is the only source of Ga,  $V_{ax}$  should correspond to the total phosphorous current  $I_{dir} + I_r + I_{dif}$  arriving to the droplet and  $V_{rad}$  to the Ga back diffusion current  $I_{bd}$ .

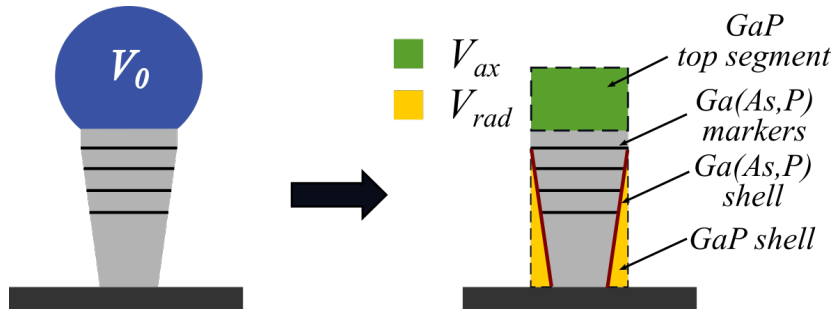


Figure 3.9: Schematics of the evolution of the NW during droplet consumption, which results in simultaneous axial and radial growth. The markers are indicated by black lines.

We performed specific experiments, at the same temperature, to measure these volumes. To this end, we insert 5 Ga(As,P) marker layers (each grown for 10 s) separated by GaP segments (grown for 50 s) during the last 5 min of a total 20 min growth. After a final 50 s GaP segment, the droplet is totally consumed by exposing the system to P only. In HAADF TEM images (see Section 2.2 in Chapter 2), the Ga(As,P) markers appear brighter than GaP due to a higher average atomic number (Figure 3.10(a-e)). We also observe a 2–3 nm-thick bright shell below the last marker (Figure 3.10(c)), indicative of a small Ga(As,P) radial growth during the terminal (marker) phase of NW growth. These bright thin vertical lines extend down to the NW foot (Figure 3.10(c-e)).

The droplet consumption results in the growth of a top segment with a length of about 4 to 4.5  $R_{NW}$  (Figure 3.10(b)). Its radius is almost equal to that of the last Ga(As,P) marker (it only diminishes slightly at the very top due to shrinking of droplet base at the end of consumption). This indicates that this top segment is grown in the VLS mode, without any significant radial VS growth, and thus corresponds to  $V_{ax}$ . In addition, a GaP shell forms. Below the last marker, its inner border is delineated by the thin Ga(As,P) shell formed before consumption, during marker growth (Figure 3.10(b)-(e)). Since this shell is hardly visible in the printed version, we mark it with a dashed line in the TEM images. Panels (b) and (c)-(e) in Figure 3.10 show that the thickness of the outer GaP shell varies from a few nm at the markers level to 13–15 nm at the NW foot. Its formation during droplet consumption (under P only) is confirmed by EDX analysis which clearly shows As-containing vertical traces corresponding to the inner Ga(As,P) shell, while no As is detected in the outer part of the shell (Figure 3.10(f)). Note that a back-diffusion of Ga all the way down to the NW foot, *i.e.* along 1.3 to 1.5  $\mu\text{m}$ , is compatible with estimates of Ga diffusion lengths of several microns during MBE growth of III-V NWs [88, 99, 143] but not with the short diffusion lengths which have been reported for GaP NWs [144]. We estimated  $V_{rad}$  as the volume between two cones, namely that of the initial back-tapered NW wrapped by the thin Ga(As,P) shell, and that bounded by the final GaP sidewall, the local GaP shell thickness being obtained by averaging those measured on the two sides of the NW.

Analysis of the volumes grown during droplet consumption shows that  $96 \pm 4\%$  of the initial droplet volume  $V_0$  is transformed into solid GaP. More precisely, we measure  $V_{ax} = (0.53 \pm 0.03) V_0 \tilde{\omega}$  and  $V_{rad} = (0.44 \pm 0.05) V_0 \tilde{\omega}$ , where  $\tilde{\omega} = \omega_{GaP}/\omega_{Ga}^L$  accounts for the fact that each Ga atom from the liquid gives a Ga-P pair (of volume  $\omega_{GaP}$ ) in the solid. Here,  $V_0$  is obtained from the narrowly distributed contact angles ( $\beta_0 \simeq 137 - 139^\circ$ ) measured by SEM on samples quickly removed from the growth

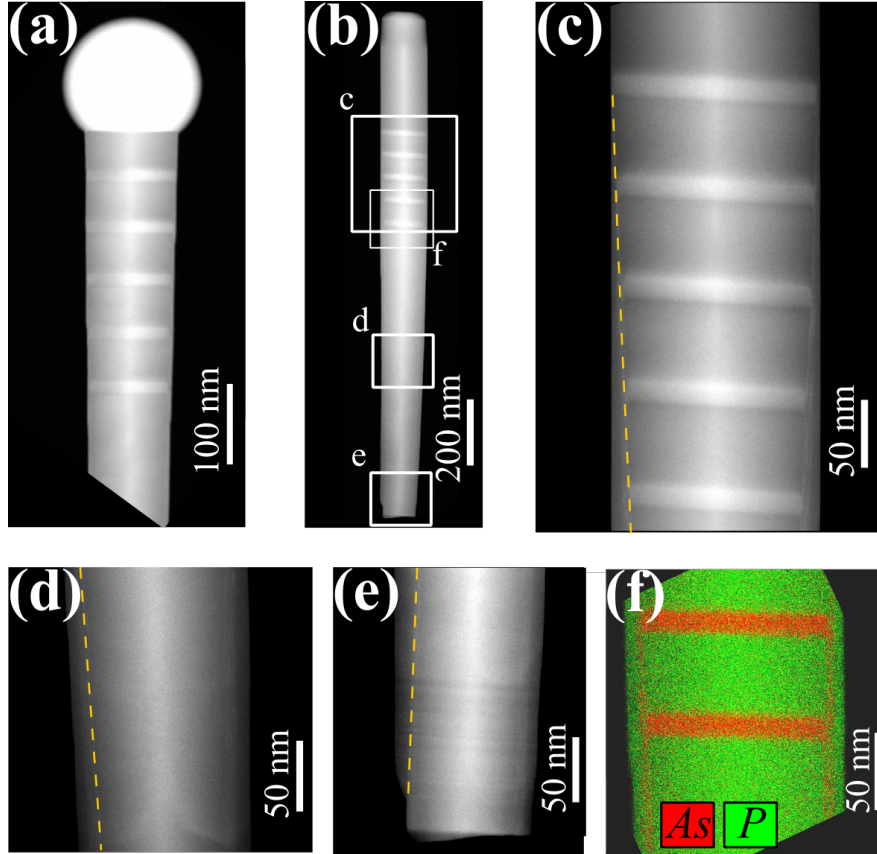


Figure 3.10: GaP NWs with Ga(As,P) marker layers inserted before droplet consumption. (a) HAADF TEM image of a NW before droplet consumption. The markers appear brighter than GaP. (b) Global HAADF TEM image of a NW after total droplet consumption. (c-e) Images of the areas indicated by the same letters in (b), showing the formation of a GaP shell along the whole NW. Dashed lines drawn at the left side mark the position of the inner Ga(As,P) shell. (f) Map of group V composition obtained by EDX spectroscopy over area (f) of panel (b), showing markers and thin As-containing shell layers parallel to NW axis.

chamber immediately after growth, with no exposure to phosphorus (Figure 3.10(a); see also Figure 3.1(b) and Table 3.1 in Section 3.2).

The NW segment grown above the last marker, is systematically shorter by about 8 % than the intermarker segments (Figure 3.10(a)), although all have been grown for the same time. This may indicate that during post-growth cooldown the temperature was sufficiently high for long enough to allow the droplet to dissolve a portion of the previously grown GaP solid, of volume  $V_m$ . If we assume that the gallium thus produced remains in the droplet, while phosphorous desorbs, the droplet volume increases by  $\Delta V_0 = V_m/\tilde{\omega}$ . Therefore, the observed droplet volume  $V_0$  in Figure 3.10(a) is larger than that immediately after stopping the growth. Nevertheless, this correction is very minor in comparison to the droplet volume, namely  $\Delta V_0/V_0 \simeq 0.01 - 0.02$ . Such a

volume increase leads a change of contact angle of  $\sim 0.2^\circ$ , which is much smaller than our accuracy of contact angle estimation. We thus conclude that the observed  $\beta_0$  can be safely taken as the contact angle at the end of NW growth. Also, recovering as solid GaP nearly the exact amount of liquid Ga estimated to be present in the droplet before its consumption strengthens our estimate of  $V_0$  and confirms that no significant loss of Ga occurs. Admittedly, the NWs might lose the bottom part of their stem when detached from the substrate for TEM analysis, but this fraction must be very small since the length of the TEM specimen closely corresponds to those measured by SEM for similar NWs still attached to their substrate. We thus believe that  $V_{rad}$  accurately measures the volume grown radially.

For back diffusion from the droplet to provide the amount of Ga necessary to form volume  $V_{rad}$ , the corresponding prefactor in Eq. (3.25) should be  $A = 6.85 \times 10^8$  at  $\text{nm}^{-1}\text{s}^{-1}$  at  $T = 600^\circ\text{C}$ . As regards axial growth, neither Lambertian nor specular re-emission, together with the direct current, provide enough phosphorous to create the observed volume  $V_{ax}$  by VLS growth. The direct and re-emitted P currents consume only 37% and 23% of  $V_0$  in the Lambertian and specular cases, respectively. What remains of  $V_{ax}$  has to be formed using phosphorous provided by sidewall diffusion. This requires phosphorous diffusion lengths  $\lambda_V$  of 80 nm and 400 nm for Lambertian and specular re-emission, respectively.

The phosphorous species impinging the NW sidewalls over diffusion length  $\lambda_V$  are thus used in two competing ways, namely diffusion to the droplet and radial growth. Our calculation of the diffusion current neglects the phosphorous lost to form the shell. However, this can only be a tiny fraction of the total. Indeed, we cannot detect any radial growth around volume  $V_{ax}$  (about 250 nm high). If so, for  $\lambda_V = 80$  nm, no P would be lost. Even with  $\lambda_V = 400$  nm, only a few percents would be lost with a shell 2-3 nm thick below  $V_{ax}$  and  $R_{NW} = 60$  nm. Anyway, our experimental  $\lambda_V$  can be taken as an effective diffusion length, accounting for a slight loss of phosphorous to radial growth. Note that the relative values of  $V_{ax}$  and  $V_{rad}$  must depend on the radius of the NW analysed. However, parameters  $\lambda_V$  and  $A$  are expected to depend only on temperature.

### 3.5 Dynamics of droplet consumption: model and experiment

With the model parameters determined in the previous section, we are now able to model self-consistently the evolution of the droplet geometry at the same tempera-

ture. From now on, all calculations are carried out using input parameters corresponding to our growth conditions, with  $R_{NW} = 60$  nm.

The number  $dN_V/dt = I_{dir} + I_r + I_{dif}$  of P atoms entering the droplet per unit time is obtained from the previous calculations, with  $I_r$  and  $I_{dif}$  calculated either for Lambertian (Eqs. (3.13),(3.14),(3.23)) or specular (Eqs. (3.21),(3.22)) re-emission. Assuming that these atoms are all used to form GaP (thereby neglecting desorption, as discussed in Section 3.3.4, or an unlikely enrichment of the liquid in P), this consumes the same number of Ga atoms stored in the droplet, which volume thus decreases by  $dV_i = dN_V \omega_{Ga}^L$ . In addition,  $dN_{III}/dt = I_{bd}$  Ga atoms leave the droplet per unit time by back diffusion, which reduces its volume by an extra  $dV_{bd} = dN_{III} \omega_{Ga}^L$ . The droplet volume  $V_d$  thus obeys equation

$$\frac{dV_d}{dt} = \frac{dV_i}{dt}(\beta, R_b) + \frac{dV_{bd}}{dt}(\beta, R_b) \quad (3.27)$$

where we stress that all currents depend on the instantaneous geometry of the droplet, defined by contact angle  $\beta$  and base radius  $R_b$ . However, a given decrease of droplet volume may be effected via a change of  $\beta$  or  $R_d$ , or both, and our model does not prescribe which particular combination of these changes will actually occur. To lift this ambiguity, we use our experimental results which, as described in Section 3.2, allow us to divide the droplet consumption process into three main stages. During stage I,  $R_b$  remains equal to  $R_{NW}$  and  $V_d$  decreases entirely via a decrease of  $\beta$ . Stage I ends when  $\beta$  reaches about  $\pi/2$ . Then (stage II), the NW starts tapering but the droplet remains pinned to the edge between tilted and top facets; we assume a fixed tapering angle  $\eta = 47^\circ$  (Figure 3.1(e)). During this stage,  $R_b$  and  $\beta$  both vary. After  $\beta$  reaches the Young's angle  $\beta_Y$ , it remains fixed to this value but the droplet depins so that  $R_b$  shrinks and its volume further decreases until vanishing (stage III).

This succession of stages is not based only on our *ex situ* observations and is not specific to GaP. Indeed, Panciera *et al.*, recently investigating the self-catalyzed growth of GaAs NWs by *in situ* TEM, observed the very same regimes when making the droplet swell or shrink by varying the V/III flux ratio [93] (these experiments were subsequently modelled, without accounting analytically for all pathways considered here [145]). Various *ex situ* observations had previously shown a tapered section near the top of the NW associated with a group-V-rich regime and a flat top facet after total droplet consumption [37, 39, 70, 146], although others did not detect tapering [131].

Once these three stages are specified, our recursive procedure allows us to model the time evolution of droplet parameters  $\beta$ ,  $R_d$  and  $V_d$ . We solve numerically Eq. (3.27) using the *MATLAB* environment. We select a time step  $dt = 0.01$  s. At each step  $k$ ,

the currents contributing to droplet consumption are calculated according to the instantaneous droplet geometry, defined by parameters  $\beta(k)$ ,  $R_d(k)$ . The droplet volume  $V_d$  at step  $k + 1$  is then computed and parameters  $\beta(k + 1)$ ,  $R_d(k + 1)$  yielding this volume are selected depending on the current stage of the process (I, II or III). These operations are repeated until the droplet vanishes ( $V_d = 0$ ).

Throughout the three stages of the consumption process, the four currents are evaluated for the instantaneous values of contact angle  $\beta$  and droplet base radius  $R_b$ . Since the currents were calculated, explicitly or not, for a droplet pinned at the TPL of a cylindrical NW ( $R_b = R_{NW}$ ), let us examine briefly if the change of NW morphology at stages II (tapering) and III (droplet depinning) might invalidate this approach. Direct current and Ga back-diffusion, which depend only on droplet geometry, are unaffected by NW morphology. Re-emission is slightly overestimated when calculated for a NW of radius  $R_b$  because of blockage by portions of the stem broader than  $R_b$ ; however, re-emission is only a minor contribution at the small angles encountered at stages II and III (Figure 3.7). Finally, P diffusion will also be affected, in a complex fashion, due to the introduction of inclined and apical facets. However, in the modelling, whereas the three other contributions are accurately computed, P diffusion is effectively adjusted to produce the correct consumption rate. This is done rather crudely by introducing a single parameter  $\lambda_V$ , which might be slightly affected by the terminal changes of morphology.

The full curves in Figure 3.11 illustrate the evolution of droplet contact angle, droplet radius, base radius and droplet volume with time when all three phosphorus pathways (direct impingement, re-emission, diffusion) are active, together with Ga back diffusion. It appears that, at variance with the calculations omitting diffusion (dashed and dash-dotted curves in Figure 3.11), these four currents consume the right amount of Ga to account for our experimental data (symbols in Figure 3.11). During stage I, the volume of the droplet can only change via a reduction of the contact angle, and during stage III via a shrinking of its base. At stage II, the droplet behaviour is more complex since  $\beta$  and  $R_b$  vary simultaneously.

We performed all calculations under two extreme alternative re-emission hypotheses, since the actual re-emission angular pattern is unknown. Our experiments can be fitted with both, albeit using very different P diffusion lengths. The value  $\lambda_V \simeq 400$  nm found for specular re-emission, about five times the Lambertian value ( $\lambda_V \simeq 80$  nm), seems unlikely large. As seen in Figure 3.7, at least for group V beam incidence  $\alpha$  below  $45^\circ$  (which accounts for most MBE setups), specular reflection delivers a much lower current to droplets with large contact angle. Moreover, Lambertian re-emission

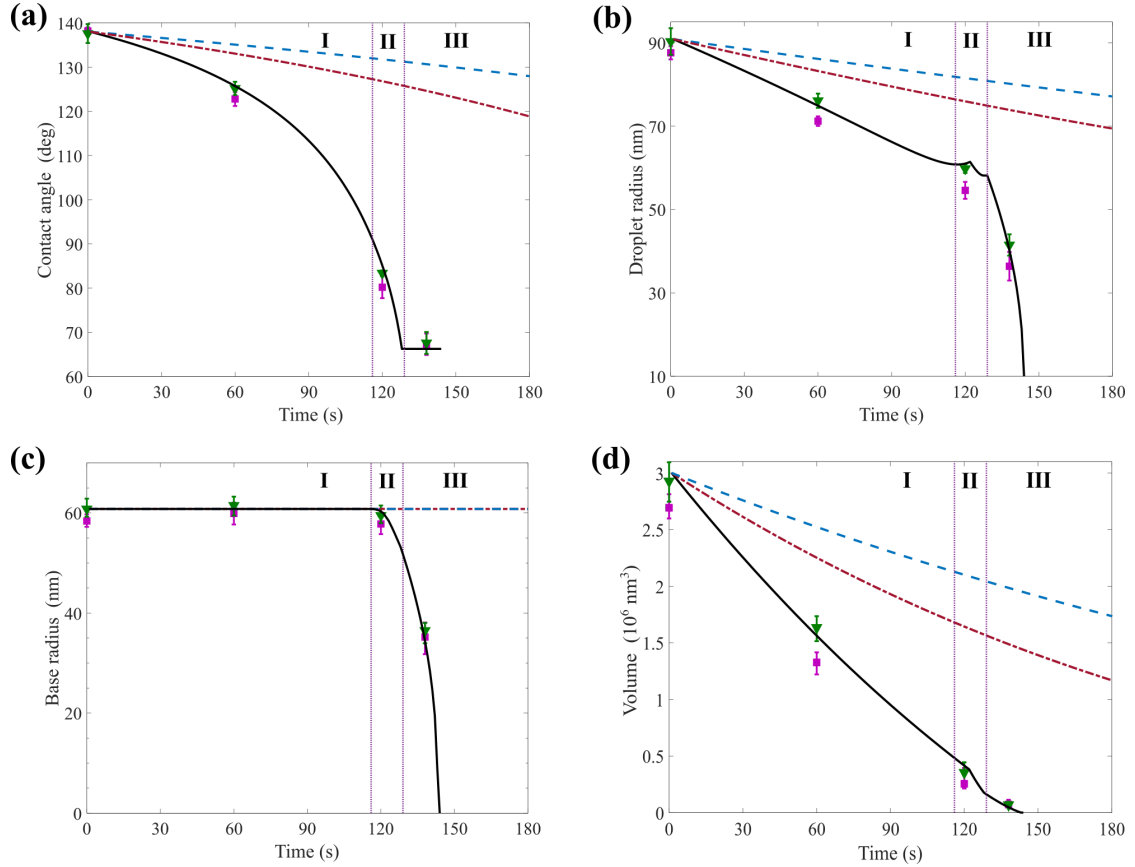


Figure 3.11: Variation of the droplet contact angle  $\beta$  (a), radius  $R_d$  (b), base radius  $R_b$  (c) and volume  $V_d$  (d) during consumption. Symbols give the experimental values for pitches of  $1 \mu\text{m}$  (squares) and  $5 \mu\text{m}$  (triangles), averaged over several NWs. The curves show the results of calculations considering only direct impingement and re-emission [specular (dashed) or Lambertian (dash-dotted)], or with phosphorous and gallium diffusion in addition (full curve).

operates until total consumption of the droplet. Since the specular re-emission currents depend on the source inclination angle whereas the Lambertian currents do not, performing experiments at different source angles might clarify this question.

### 3.6 Changing at will the droplet dimensions

Our model predicts accurately the consumption time needed to reduce to desired values the contact angle or base radius of a droplet seating on the top of a NW of given radius, exposed to a known group V flux. To be able to stop the consumption at the right time, it is necessary to understand how the different pathways considered contribute to this consumption and how accurately they need to be controlled.

To this end, we analyse the droplet fractions consumed in the different possible ways. Figure 3.12 shows the evolution of each current with time during consumption.

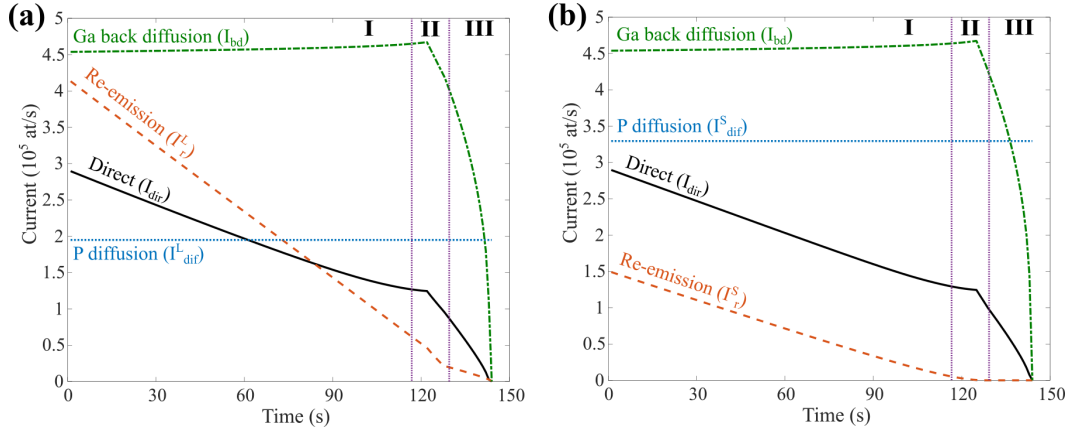


Figure 3.12: Variation of direct  $I_{dir}$ , re-emitted  $I_r^{L(S)}$  and diffusion  $I_{dif}^{L(S)}$  currents of P and back diffusion current  $I_{bd}$  of Ga during droplet consumption, under assumptions of Lambertian (a) and specular (b) re-emission of group V from the substrate.

For large contact angles, at the beginning of consumption, the contributions from the four material pathways are of the same order. When the contact angle decreases, the phosphorous impingement currents diminish (and even vanish in the specular case), making Ga and P diffusion (which are  $\beta$ -independent except for barely noticeable small size effects at very small  $R_b$ ) the most effective mechanisms for emptying the droplet. During stages II and III, Ga back diffusion diminishes due to the decrease of  $R_b$  but P diffusion remains constant. The corresponding current (Eq. (3.25)) depends only on droplet base radius and temperature, whereas the phosphorous currents (Eqs. (3.1), (3.22), (3.13), (3.21), (3.23)) all scale with external flux  $F_e$ . This gives two different means to control the droplet consumption rate, namely via substrate temperature and via the external phosphorous flux. In addition, the final droplet size might be affected by the residual group V species that linger in the MBE chamber even after the closure of all valves and shutters [101].

Obviously, an accurate control of droplet geometry requires low consumption rates. In Figure 3.12, the currents are calculated for our experimental phosphorous flux of  $1.07 \times 10^{19}$  at  $\text{m}^{-2} \text{s}^{-1}$ , equivalent to a planar growth rate of  $\sim 0.43 \text{ nm s}^{-1}$ , which is already quite high. While reducing the droplet contact angle to values, required for the WZ structure formation, can be performed easily, even under such high fluxes, stopping the droplet consumption at a very small base radius might be tricky. To do this, one will aim to stop the droplet consumption at the end of stage II or even at stage III (see Figure 3.11(c)), where the droplet base radius  $R_b$  decreases rapidly. At these small diameters and contact angles, the droplet is mostly consumed via Ga back diffusion, which decreases with  $R_b$ , and via phosphorous diffusion.

To obtain lower consumption rates, one can decrease the incoming phosphorous

flux, which however will not affect the contribution from Ga back diffusion. Another option would be to reduce Ga back diffusion. This might be done by diminishing the temperature, but the understanding of the temperature dependence of the back diffusion current requires an additional study. Furthermore, it will be necessary to consider, how Ga back diffusion depends on the external phosphorous flux and if this process can occur at all without the presence of phosphorous species on the NW sidewalls. If this was the case, it would be possible to consume the droplet by Ga back diffusion current only, without providing any group V flux. This would also be useful in the fabrication of crystal phase heterostructures, since it will allow one to avoid axial NW growth, which is known produce the stacking faults and polytypism during the consumption [37, 39, 131]

### 3.7 Summary and conclusions

To conclude, in this Chapter we presented a comprehensive model of the consumption of a group III droplet seating on top of a III-V NW when only group V atoms are provided. The model is based on series of experiments on Ga droplets on top of self-catalyzed GaP NWs, exposed to P. We find that, beside the direct impingement of group V species and their re-emission from the substrate, group V diffusion to the droplet and group III back diffusion from the droplet, along the NW sidewalls, both contribute significantly to the consumption process. We established a general method to measure the parameters governing these two fluxes. We derived analytical expressions for all re-emitted and diffusion currents as a function of instantaneous droplet geometry, which we then used to model the decrease of the droplet volume over time. Our experimental data can only be correctly fitted if the four consumption pathways are included.

Our model allows one to predict the time needed to reduce the droplet to a given geometry, under a given group V flux and starting from a known geometry. Controlling the droplet contact angle is key to selecting at will the crystal phase of III-V NWs [93] and fabricating crystal phase heterostructures [25, 147, 148]. On the other hand, lateral confinement in radial heterostructures requires tailoring the droplet base radius. While dedicated *in situ* TEM experiments offer unprecedented opportunities to achieve such control in a single NW, it is highly desirable to attain the same objectives reproducibly and blindly in arrays of identical NWs grown on a crystalline substrate in a standard epitaxy equipment. Our model, which is generic at least for III-V NWs, grants such control, in particular by predicting precise timings for the two extreme stages of consumption, where one of the two geometrical parameters of the droplet (contact angle

or base radius) varies while the other remains constant. As will be shown in the next Chapter, the implementation of our model makes it possible to consume partially the droplet and stop this process, once the droplet reaches the desired geometry.

# Chapter 4

## Towards diameter-modulated nanowires

### 4.1 Modulation of nanowire diameter - State of the art

As discussed in the previous Chapter, most of NW properties are controlled by the droplet size and shape. Precise control of the growth condition allows one to perform deterministically the modulation of NW composition [28,101,149] and crystal structure [25,27,91,93,95,147,148,150,151] during VLS growth. As for diameter modulations, *i.e.* multiple and, possibly, periodic diameter change with more or less sharp transitions, which can modify photonic, electronic and thermal characteristics of a NW, and thus present a particular interest for photonic, plasmonic and metamaterials [111–113], an explicit procedure, that would allow one to vary the NW geometry locally at will during growth, is yet to be demonstrated.

On the other hand, several groups proposed a method of controllable diameter variation, which is based on post-growth NW etching [30,31,112,152]. In particular, VLS-grown Si NWs were doped selectively according to the desired modulation profile and then thinned locally by preferential chemical wet etching (Figure 4.1(a)). The diameter variation follows the doping profile due to the doping-level dependence of etching rate [153]. A similar method was applied to III-V NW; for instance, GaAs segments of GaAs/GaP axial heterostructures were selectively etched [154]. In this case, the selectivity was due to the material selectivity of the etching rates of a bromine solutions: the etching rate of GaP appears to be much lower than that of GaAs. Another possibility is to use a selective area etching, where the diameter modulation profile is defined by the pattern, written in a PMMA resist which is deposited over the

NWs after the growth [155]. However, even though these methods can give a precise control of the NW local geometry, present several drawbacks, such as an increased roughness of the etched surface. Also, these procedures require a complex preparation of the NWs (*e.g.* PMMA resist patterning and multistage chemical treatment). Post-growth treatments, which take place out of the growth chamber, complicates the use of diameter-modulated structure for further epitaxial growth, for instance, to form a shell. There is thus an interest to modulate in a controllable fashion the geometry of a NW during VLS growth itself.

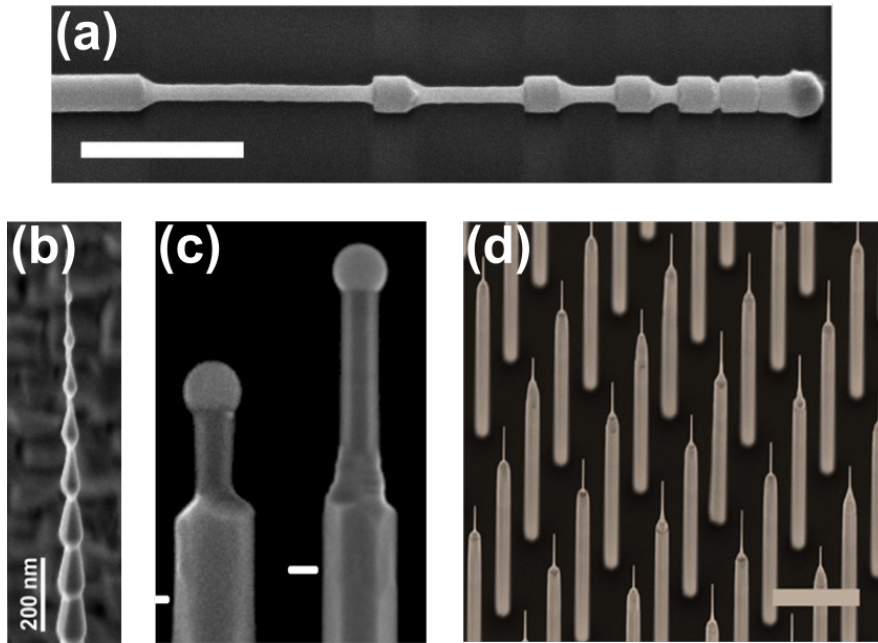


Figure 4.1: Collage of TEM images of diameter-modulated NWs, obtained by various authors using different techniques. (a) Si NWs chemically etched after growth. The diameter modulation is due to the doping-dependence of the etching rate. Adapted from [30]. (b) Spontaneous diameter modulations in InP NWs. Adapted from [156]. (c) Examples of thin GaAs NW segments, grown after complete droplet consumption and further regrowth. Adapted from [37]. (d) Array of GaAs NWs with thinner segments on their tops, grown by multistep variation of the V/III ratio. Adapted from [39].

Indeed, the first diameter modulation was observed by Givargizov [157] for Si and Ge NWs, shortly after the first demonstration of VLS growth. The NW diameter changed periodically by a factor up to 3 or 4 between thin and thick parts. This effect was observed only for the NWs with a diameter below 500 nm and the onset of the oscillations was attributed to the changes of the surface energies at the initial stage of growth, when the NW rises from the substrate. The oscillations themselves were explained by the positive feedback of the droplet curvature to its supersaturation due to the Gibbs-Thomson effect: the decrease of the NW radius causes the increase of

the droplet curvature and therefore the decrease supersaturation, which, in turn, yield a droplet contact angle increase and further increase of the droplet curvature. This processes repeat until the droplet surface area decrease to some value, at which the material current, entering the droplet via vapour-liquid interface becomes smaller than that of the growth at the liquid-solid interface. The NW radius shrinking stops, and all the processes then repeat in reverse. Although the author determined the dependence of the occurrence of the oscillations on the mean NW diameter, temperature and vapor pressure, the amplitude and period of oscillations was found to be unique for each NW. The possible control of the process was not discussed further.

The formation of similar structures was reported more recently by Oliviera *et al.* [156, 158] in Au and Ag-catalyzed InP NWs (Figure 4.1(b)). Here, the oscillations were explained by the deformation of the TPL as the droplet starts to wet the sidewalls, which induces a change of its contact angle. These diameter oscillations were found to correlate with the crystal structure of the NW: the thick and thin segments exhibit ZB and WZ crystal structure, respectively. Again, the diameter changes were reported as spontaneous and their control was not discussed.

Attempts to perform a controllable local diameter reduction were carried out using *in situ* selective area thermal annealing. This was demonstrated for GaSb/InAsSb NWs, where the NWs was selectively etched at the heterojunction due to the presence of less thermally stable  $\{111\}$ A facets at the heterointerface [159]. Post-growth thermal NW decomposition, initially proposed for uniform NW thinning [26], appears to result in tapered NWs in regular arrays [160] and can be anisotropic due to local structural defects (such as twins and stacking faults) [161].

As for controlled NW diameter change in a single VLS growth run, Priante *et al.* [37] and Somaschini *et al.* [120] independently reported the controlled regrowth of a thin GaAs NW segment on the top of a thick stem. In these studies, the initial catalyst droplet was totally consumed by exposure to As, and was then re-created under Ga and As fluxes with the same effective V/III ratio as during the stem growth (Figure 4.1(c)). Although the diameter reduction of the NW top segment was achieved, long regrowth times result in a significant diameter increase of the thin part by VS growth, so that it becomes almost equal to that of the stem. Lately, several studies achieved the growth of a thinner segment of a stable diameter [39, 162]. There, the idea of a NW diameter control by a droplet was fully employed: prior to the top segment growth, the droplet was partially consumed by variation of the V/III ratio (Figure 4.1(d)). It is also was reported that the thin segment presents dominantly the WZ crystal phase, which is associated with the fact that the droplet on the top of the thin segment has a contact

angle close to  $90^\circ$ , as has been shown in later studies [93]. The stable geometry was attributed to self-stabilization of droplet diameter according to the V/III flux ratio. The growth of the thick segment on the top of a thin stem has been demonstrated so far only in InAs/InSb axial heterostructures [163–165]. In these studies the widening of the top InSb segment was due to an extensive VS radial growth, and thus cannot be controlled by the droplet.

So, most of diameter modulated structures obtained in a single growth run, occur spontaneously. While the growth of a thin segment on top of a thick stem can be performed in a single-material NW, as demonstrated in Refs. [37,39,120,162], the growth of a segment thicker than the stem was demonstrated only in NW axial heterostructures. However, it is highly desirable to perform both of these changes deterministically and to control precisely the final dimensions of the diameter-modulated NW. Such control is delicate since, considering the impossibility of direct and real-time observation of these processes in standard epitaxy systems, there is a risk of not reducing enough the diameter of the droplet or on the contrary to consume it entirely or, in case of the droplet inflation, to make it slide on the NW sidewalls. In the next sections, we present results of the local reduction and increase of the NW diameter in a controllable fashion. The procedures, which implement the change of a NW diameter, are primarily based on our enhanced understanding of the droplet dynamics, discussed in Chapter 3.

## 4.2 Reducing the nanowire diameter

Let us first address the growth of a thin GaP segment on the top of a GaP stem. To this aim, we used the growth sequence presented in Figure 4.2.

The experiments were performed on patterned Si(111) substrates covered with a 46 nm thick layer of silica ( $\text{SiO}_x$ ) at a substrate temperature of  $600^\circ\text{C}$ . The pattern and substrate pre-growth treatment were the same as described in Section 2.3.2 of Chapter 2. Each growth run started with Ga droplet pre-deposition during 2 min. The Ga flux was set to  $3.46 \times 10^{18}$  at  $\text{m}^{-2} \text{s}^{-1}$ , which corresponds to 2D growth rate of  $0.140 \text{ nm}^{-1} \text{ s}^{-1}$  on GaP(100), and was maintained at the same value at all growth steps, where it was used. The Ga and  $\text{P}_2$  fluxes were then simultaneously provided for 20 min in order to grow the NW stem. The phosphorous flux was adjusted to  $4.5 \times 10^{18}$  at  $\text{m}^{-2} \text{ s}^{-1}$  so as to obtain a V/III atomic flux ratio of 1.3. For *partial droplet consumption*, the NW was exposed to the sole  $\text{P}_2$  flux, corresponded to a V/III flux ratio of 3 (*i.e.*  $1.04 \times 10^{19}$  at  $\text{m}^{-2} \text{ s}^{-1}$ ). The consumption time  $t_c$  was adjusted according to the model presented in Chapter 3, to obtain a droplet with base radius below 20 nm. The *thin*

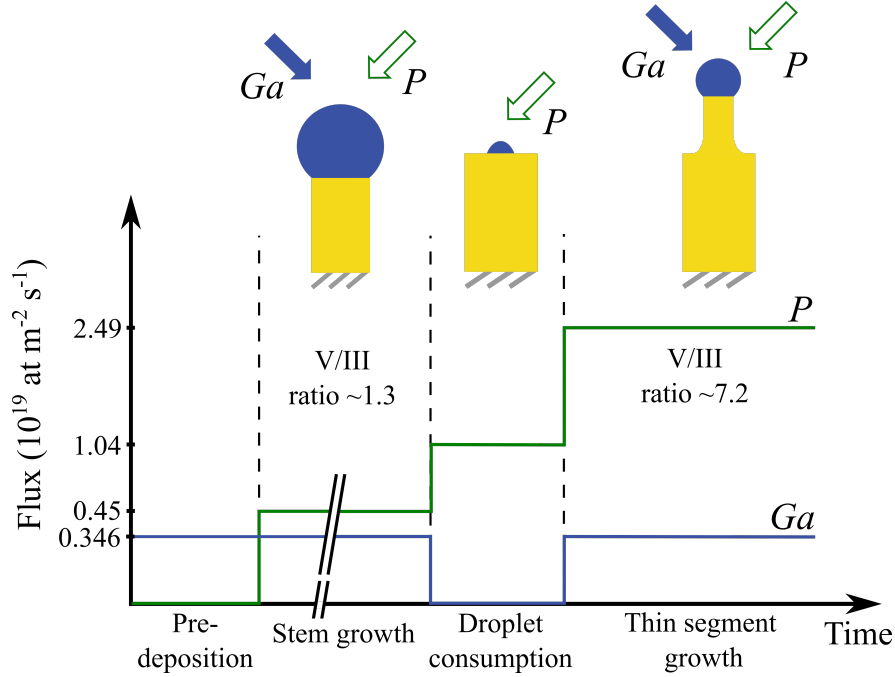


Figure 4.2: Schematics of the growth sequence for the growth of a NW with a thin top section.

*segment* was then grown under both Ga and P<sub>2</sub> fluxes at a V/III ratio of 7.2 (*i.e.* P<sub>2</sub> flux was  $2.49 \times 10^{19}$  at  $\text{m}^{-2} \text{s}^{-1}$ ). The fluxes were interrupted by closing the material source shutters and, for the phosphorous flux, adjusted by gradually opening or closing the valve, in order to obtain the most abrupt variation. Each growth was terminated by closing all shutters and valves abruptly, and turning off the oven for rapid cooling.

Table 4.1: Measured and calculated morphologies of GaP NWs stem and thin top segment, grown in arrays with various pitches.  $R_{NW}$ : the top NW stem radius before the droplet consumption;  $R_b^{est}$ : the base radius of the droplet after its partial consumption, estimated using the model of the droplet dynamics from Chapter 3;  $R_f^{ext}$ : the measured radius of the top thin segment.

Pitch (nm)	300	500	1000	2000
$R_{NW}$ (nm)	$57 \pm 3$	$67 \pm 3$	$69 \pm 2$	$71 \pm 2$
$R_b^{est}$ (nm)	0	16	19	21
$R_f^{exp}$ (nm)	$23 \pm 6$	$22 \pm 3$	$21 \pm 3$	$22 \pm 3$

To adjust the consumption time  $t_c$ , a test calibration sample, which included the pre-deposition and NW growth steps, was grown. This sample provides the NW geometry at the end of the stem growth, namely base radius  $R_b$  (which is equal to NW radius  $R_{NW}$ ) and droplet contact angle  $\beta$ . These values were then introduced into the model of the droplet dynamics in order to calculate the time  $t_c$ , required to deflate the droplet to desired dimensions.

The first row of Table 4.1 reports the NW radius  $R_{NW}$  for several pitches, measured before the droplet consumption. The contact angle  $\beta$  is  $137^\circ \pm 1^\circ$  for all the pitches. Based on these values, we set the droplet consumption time to  $t_c = 195$  s. Upon the exposure of NWs with radius  $R_{NW}$  to a phosphorous flux of  $1.04 \times 10^{19}$  at  $\text{m}^{-2} \text{s}^{-1}$ , the droplet base radius should decrease to value  $R_b^{est}$  given in Table 4.1, depending on initial NW radius. Such a droplet should have a contact angle  $\beta$  close to the Young's angle  $\beta_Y \simeq 65^\circ$  and be depinned from the stem sidewalls, which corresponds to Stage III of the droplet consumption (see Figure 3.12(a) on page 52, Section 3.5 of Chapter 3).

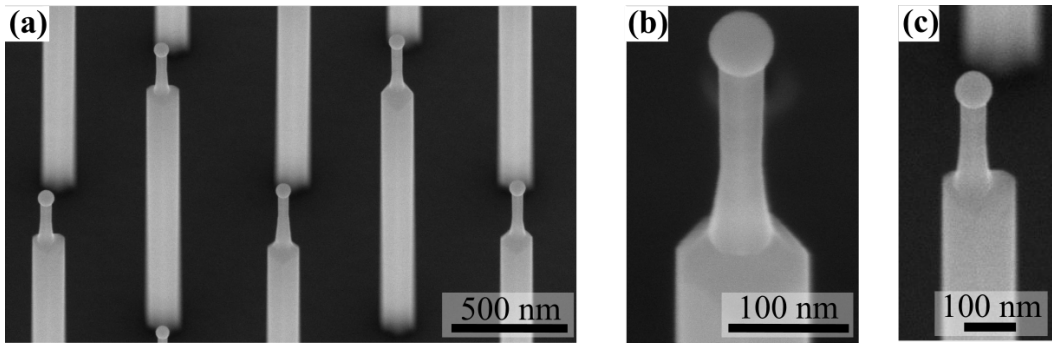


Figure 4.3: SEM images of GaP nanowires with a thinner top part: (a) General view of an array. (b) Regrowth during 5 min results in a thin segment of length 300 nm and diameter 35 nm. (c) A NW with a thin segment of a similar dimensions, but not centred at the top of the stem.

Further growth under the V/III flux ratio of 7.2 for 5 min results in a thin GaP segment with a length of 250-300 nm (Figure 4.3) and radius  $R_f^{exp}$ , given in Table 4.1. The contact angle of the droplet on the top of the thin segment is  $136^\circ \pm 1^\circ$ . We assume, that during this step the droplet can vary its contact angle and base radius, but without significant volume increase, since the growth occurs at high V/III ratio. The enlarge of the volume may only be caused by the gallium sidewall diffusion current increase, since the other direct and re-emitted gallium currents scale with the droplet contact angle in the same manner as phosphorous ones. The final radius of the thin segment should thus be smaller than the droplet base radius at the end of consumption. For instance, apical droplet of the same volume with base radius of 20 nm and contact Young's angle of  $65^\circ$  would have the base radius of 13 nm for the contact angle of  $136^\circ$ . On the other hand, thin segment will be affected by the radial growth, which will increase its radius, and thus the droplet base radius. Actually, the measured thin segment radii are slightly larger than those, predicted by the model (Table 4.1). This difference is however less than dispersion of the measurements, at least for the NWs, grown in the arrays with pitches of  $1 \mu\text{m}$  and  $2 \mu\text{m}$ . The interface between the thin and thick segments is sharp,

but the top part of the thick segment exhibits some tapering. This tapering is the one mentioned to occur at stage II of droplet consumption (see Section 3.5 of Chapter 3). Moreover, some thin segments are not centred on the thick segment (Figure 4.3(c)), which could be explained by a motion of the droplet after depinning. This has recently been observed during the *in situ* growth of GaP NWs [166].

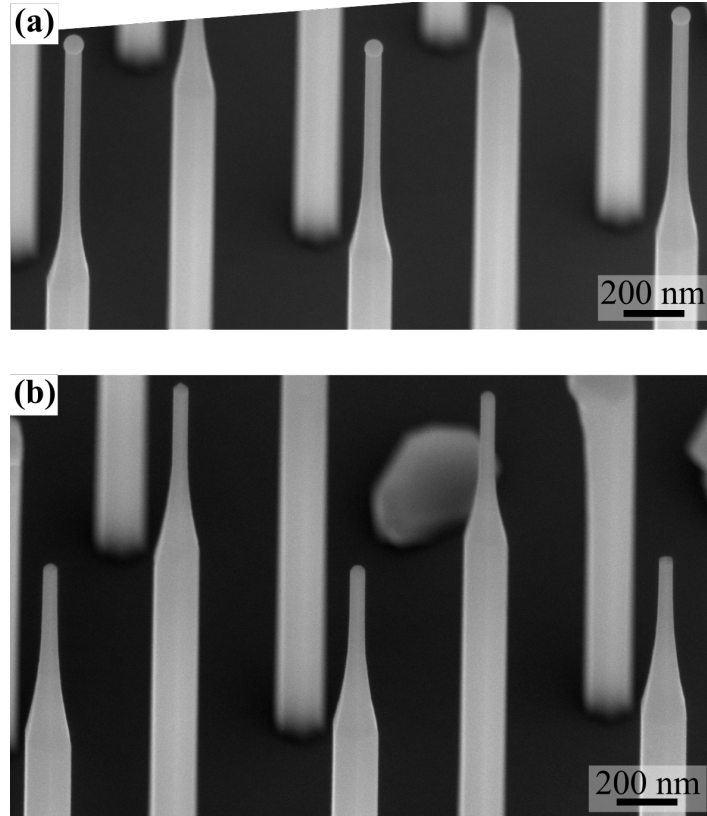


Figure 4.4: SEM images of GaP nanowires with thinner top part after 10 min of regrowth. Such a thin segment has the length of 700 nm and the diameter of 50 nm. Some NWs (a) still have the catalyst droplets on their top, but on the top of the others (b) the droplets are consumed.

If the thin segment is grown for longer (10 min in Figure 4.4), radial growth becomes significant. This is very pronounced around the thin/thick segments interface: the radius  $R_f^{exp}$  of the upper part of the thin segment increases to 25-30 nm, while closer the interface (which is not sharp any more and is hidden in the intermediate tapered section) it becomes equal to that of the thick stem. This could be explained by a Ga accumulation on the inclined facets, which would enhance radial growth. Even accounting for radial growth, the radius of the NW is reduced by a factor of three from top to bottom, except at the interface, where it changes continuously.

Although the thin top segment is grown at high V/III flux ratio, the droplet contact angle is almost equal to that typically observed at a low V/III flux ratio. It is  $136^\circ \pm 1^\circ$

for the apical droplets after 5 min of growth at a V/III ratio of 7.2 (Figure 4.3), and decreases to  $129^\circ \pm 2^\circ$  for a NW with a longer thin segment ((Figure 4.4)(a)). In both cases, the thin segments exhibit a uniform radius over a length of several hundreds of nm. This is different from the observations of Kim *et al.* [39], who proposed that the radius of the thin top part stabilizes when the droplet shrinks to the contact angle around  $90^\circ$  due to its continuous consumption under excess of group V species. In our experiments, the continuous consumption also takes place, which is the reason of the different droplet contact angles after 5 and 10 min of thin segment growth, but a stable NW radius can be achieved in both cases. Nevertheless, some NWs do not present any droplet on their top after longer growth (Figure 4.4(b)). This could indicate that, even the stable growth is possible at high V/III flux ratio, the droplet can be consumed faster in some particular cases due to an excess of group V species.

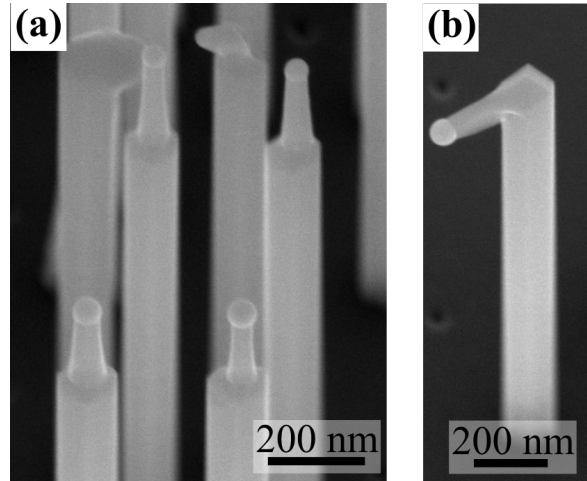


Figure 4.5: Examples of NWs with degraded morphology occurring during the growth of the thin segment.

Interestingly, for the small pitch of 300 nm, our model predicts the total consumption of the droplet, while some NWs exhibit the growth of a thin top segment (Figure 4.5(a)). But in contrast to the larger pitches, the dispersion of the radii of the top thin segments is high. In addition, the NWs sometimes exhibit a degraded morphology, such as the growth of a thin segment along the  $\langle 110 \rangle$  sidewall facet normal (Figure 4.5(b)). As stated before, our model does not take into account the complex effects of mutual shadowing and re-emission from neighbours, which have a significant impact on the droplet consumption and on the thin segment growth in short-pitch arrays. The preservation of the droplet under conditions where it is expected to be totally consumed, can originate either from a significantly lower amount of phosphorous impinging the droplet during the consumption, or from droplet recreation under simultaneous exposure to Ga and  $P_2$  fluxes, as shown in Ref. [37]. Also, the closeness of radii to those

in arrays with larger pitch could mean that, apart from the initial droplet base radius, the radius of a thin segment could be defined by droplet shape stabilization at given V/III flux ratio, as proposed in Refs. [39, 144].

To summarize, in this section, we demonstrate a reduction of the NW diameter by controlled partial droplet consumption. The resulting radius of the top thin segment are almost equal to the base droplet radius after partial consumption, predicted by our model of the droplet dynamics. In addition, we show, that a stable radius of the top thin segment at high V/III flux ratio can be achieved for large droplet contact angle. This fact can foster the future crystal phase engineering of the thin segment.

### 4.3 Enlarging the nanowire diameter

If, instead of delivering only group V flux to consume the droplet, we provide Ga in excess of P, then the droplet will inflate rather than shrink. To this end, after growing the NW stem, one can reduce the group V flux to achieve a V/III ratio below 1. The droplet then receives considerably less group V species than group III species, the excess of which enlarges the droplet volume. As already mentioned, the droplet volume can be changed through variation of two parameter, namely base radius  $R_b$  and contact angle  $\beta$ . Several studies predict, that the growth at V/III flux ratios below one should result in an unlimited increase of both parameters [38, 167]. In any case, the experimental preservation of the droplet on the top of the NW is not a trivial task under such conditions, since it can slide on the NW sidewalls, and the growth of a vertical NW will not be possible. But if one succeeds in stabilizing the droplet under group III-rich growth conditions, further growth should lead to the formation of a thicker segment. In this section, we present our attempts to achieve such a stable growth of GaP NWs with a thick top segment.

To study the NW radius enlargement, we performed experiments following the growth sequence showed in Figure 4.6. The growth started with the Ga droplet pre-deposition on patterned Si(111) substrates for 2 min, which was followed by 20 min of NW growth. During NW growth, the phosphorous flux was adjusted to  $7.27 \times 10^{18}$  at  $\text{m}^{-2} \text{s}^{-1}$ , so as to provide a V/III flux ratio of 2.1. To increase the droplet volume we then decreased the phosphorous flux, while keeping the same gallium flux as during the stem growth. Therefore, the V/III flux ratio diminishes. These conditions were kept for a certain time  $t_{in}$ , which was also varied. Then, the phosphorous flux was set back to its initial value to grow a thicker segment. In all the experiments, the Ga flux was kept at  $3.46 \times 10^{18}$  at  $\text{m}^{-2} \text{s}^{-1}$  (corresponds to an equivalent 2D growth rate of 0.140

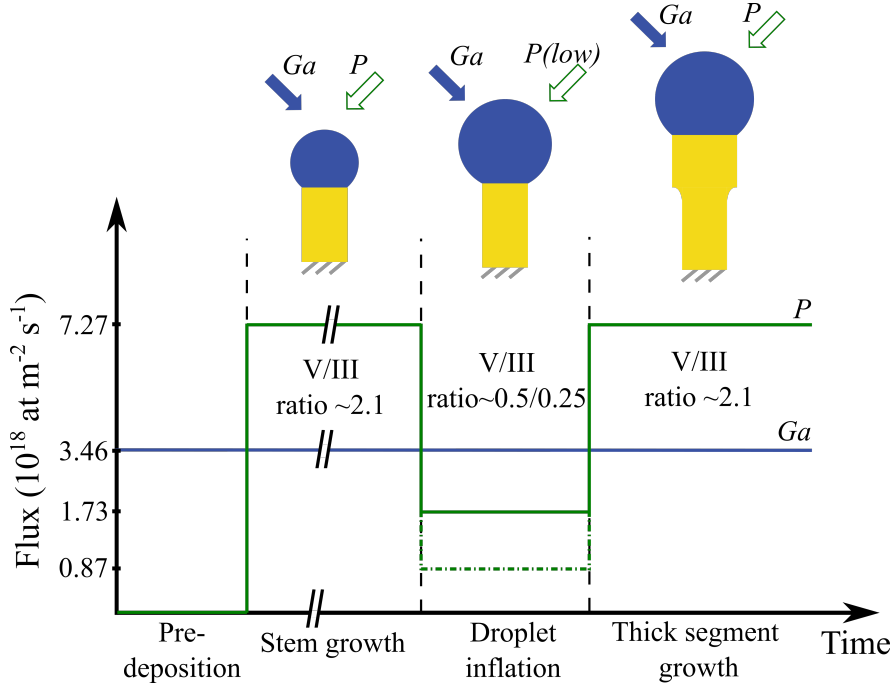


Figure 4.6: Schematics of the growth sequence for a NW with a top thick stem.

$\text{nm}^{-1} \text{ s}^{-1}$  on GaP(100), same as in the previous section). The substrate temperature was of  $600^\circ\text{C}$ . The growth was terminated by closing all shutters and valves abruptly, and turning off the oven for rapid cooling.

We first study how the droplet changes geometry under excess Ga. To this end, we performed a series of experiments, consisting of only the first three stages of the sequence in Figure 4.6. After Ga pre-deposition and stem growth, the  $\text{P}_2$  flux was reduced to achieve the Ga-rich conditions, *i.e.* V/III flux ratio below 1. We tested V/III flux ratios of 0.5 and 0.25, which correspond to the phosphorous fluxes of  $1.73 \times 10^{18}$  at  $\text{m}^{-2} \text{ s}^{-1}$  and  $8.65 \times 10^{17}$  at  $\text{m}^{-2} \text{ s}^{-1}$ , respectively, and these conditions were maintained for various time  $t_{in}$ .

Before the droplet inflation (*i.e.* for  $t_{in} = 0$ ), the as grown NWs are slightly back-tapered, with a radius of 35-40 nm at the bottom and 55-60 nm at the top, and a length of 900-950 nm (Figure 4.7(a)). Same as in Section 3.2 of Chapter 3, the droplet contact angle  $\beta$  is  $138 \pm 2^\circ$ . The exposure of the NW to Ga and  $\text{P}_2$  fluxes with a V/III ratio of 0.5 during  $t_{in} = 4$  min leads to an increase of the droplet volume (Figure 4.7(b)). Its contact angle  $\beta$  increases to  $147 \pm 2^\circ$ , while its base radius  $R_b$ , which is equal to the top NW radius, remains almost the same. The NWs still exhibit a slight back-tapering. Interestingly, doubling the exposure time to  $t_{in} = 8$  min at V/III ratio of 0.5 leads to an increase of the top NW radius, and, hence, of the droplet base radius  $R_b$ , while the droplet contact angle  $\beta$  remains the same (Figure 4.7(c)). On the other

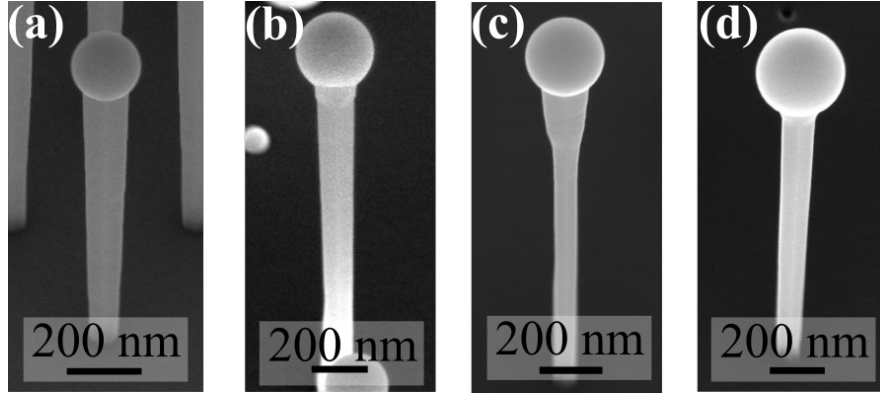


Figure 4.7: SEM images of the droplet after inflation for various times. The apical droplet (a) immediately after the growth of the stem with  $\beta \approx 138^\circ$  and (b) after being inflated for 4 min at a V/III ratio of 0.5, with  $\beta \approx 147^\circ$ . Longer inflation during 8 min (c) enlarges the NW radius, but the droplet contact angle remains the same. Reducing the V/III ratio to 0.25 leads to a droplet with  $\beta \approx 158^\circ$  after 8 min of exposure.

hand, the droplet contact angle continues to increase and reaches  $158 \pm 1^\circ$  on the NWs subjected to gallium and phosphorous fluxes with a V/III ratio of 0.25 during  $t_{in} = 8$  min (Figure 4.7(d)).

We speculate that the catalyst droplet, exposed to fluxes with a V/III ratio below 1, changes volume firstly by adapting its contact angle  $\beta$ , and for each V/III ratio there is a stable contact angle  $\beta_s$ . This behaviour of the droplet is different from that proposed by Tersoff [167], who predicted the unlimited increase of droplet contact angle under V/III ratios below unity. The existence of such a stable contact angle can be explained by the equilibration of the net currents, entering and leaving the droplet, due to its change with droplet inflation. It is known, that during the VLS growth the Ga atoms are mostly delivered to the droplet by sidewall diffusion [87, 100]. The phosphorous species are mainly provided by the direct and re-emitted current, and the latter is almost twice larger than the direct current for the large droplet contact angles (see Figure 3.7, page 41). Therefore, the increase the droplet contact angle will increase the phosphorous direct and re-emitted current, entering the droplet. On the other hand, Ga diffusion current will remain the same, since it depends only on the NW radius, which is stable, at least during the increasing the droplet contact angle. So at a certain contact angle  $\beta_s$ , the Ga currents, enlarging the droplet, and phosphorous currents, reducing its volume by formation of GaP solid, becomes equal, and the droplet stops to inflate. In addition, a further contribution to the droplet contact angle stabilisation could originate from the Ga back diffusion from the droplet, but it is not sure that this process operates under group-III-rich conditions. This would require an additional study.

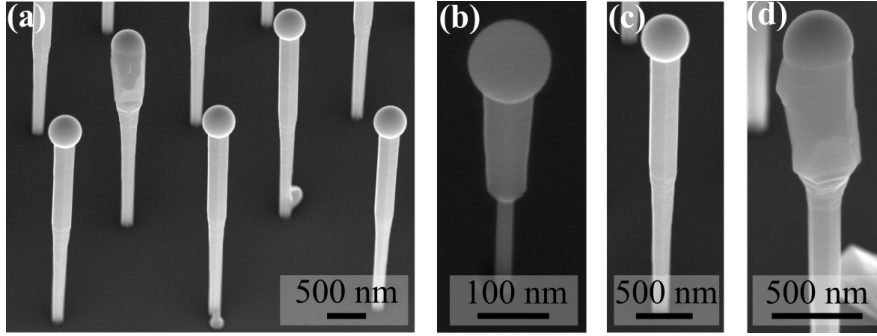


Figure 4.8: SEM images of the GaP NWs with a thicker segment above the narrower one. (a) General view of an array with apical droplets enlarged after 8 min of growth at low V/III flux (effective ratio of 0.5). After 8 min of regrowth under the initial V/III flux ratio of 2.1, the NWs with a thin stem equal to  $R_f = 11$  nm (b) enlarge relatively more ( $R_e = 34$  nm,  $R_e/R_f \approx 3$ ) than those with a thick stem equal to  $R_f = 75$  nm (c), for which  $R_e = 120$  nm ( $R_e/R_f \approx 1.5$ ). (d) An example of a nanowire with degraded morphology occurring during the growth of the thick segment.

To stabilize the radius of the thick top segment, after the droplet inflation for 8 min at V/III ratio of 0.5, the phosphorous flux was changed back to the value used during the stem growth (V/III ratio of 2.1). Growth during 8 min in such conditions results in the formation of NWs with a segment with larger radius  $R_e$  above a stem with smaller radius  $R_f$  (Figure 4.8). The NWs with a narrow stem exhibit a sharp stem/thick segment transition (Figure 4.8(b)), while in those with a thicker stem the transition extends over several tens of nanometers (Figure 4.8(c)). Even though during the growth of the thick segment the V/III flux ratio is set back to 2.1, the droplet contact angle keeps almost the same value  $\beta = 144 \pm 2^\circ$  as during the inflation stage. This is further evidence to support our assumption of the existence of a stable  $\beta_s$ . Although the NWs are grown in arrays, which usually produces uniform ensembles, some NWs display an enormous radial growth at the transition between thin and thick segments, and above (Figure 4.8(d)). The contact angle of the apical droplet on top of such NWs is much lower, namely  $\beta = 93 \pm 2^\circ$ .

Since our patterned substrates contain holes with various radii, we are able to study the variation of radius of the thick top segment  $R_e$  with the stem radius  $R_f$ . Interestingly, the radius  $R_e$  is not independent on  $R_f$ , as could be expected if the radius of the thick segment stabilised only according to the V/III flux ratio. Moreover, this dependence is not linear (Figure 4.9(a)). For the smaller stem radii  $R_f$ , the NW can double or even triple its radius for the thick segment. Our maximum enlargement ratio  $R_e/R_f$  of 3 is observed for the NW with  $R_f = 11$  nm (Figure 4.8(b)). For NWs with a thick stem, the enlargement ratio is limited to 1.5 ( $R_f = 75$  nm,  $R_e = 120$  nm; Figure 4.8(c)). The dependence of the enlargement on the thin segment radius is

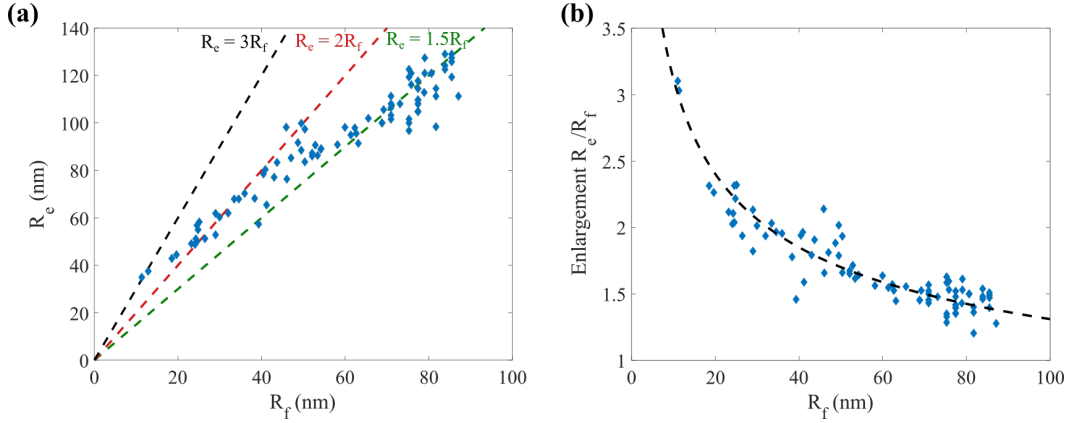


Figure 4.9: (a) Variation of the radius of the top thick segment  $R_e$  with the stem radius  $R_f$ . The dashed lines give the possible examples of an hypothetical linear dependence of  $R_e$  on  $R_f$ . (b) Variation of enlargement ratio  $R_e/R_f$  with stem radius  $R_f$ . Symbols give the experimental values. The dashed curve gives the fitting with a power law  $R_f^{-K}$  with  $K \approx 1/3$ .

shown in Figure 4.9. Actually, the enlargement ratio seems to depend continuously on the stem radius, with a power law ( $\propto R_f^{-K}$  with  $K \approx 1/3$ ). Note however that the NWs with the thinnest stems display a modest back-tapering. The stable radius of the thick segment can thus be larger and the final enlargement ratio can increase.

This effect can be related, again, to the equilibration of the net currents, and probably to the Ga diffusion current, which increases with the NW radius. Since the Ga diffusion length depends on the orientation of the NW facet [168], the Ga surface diffusion currents, entering the droplet, when it is pinned to the inclined sidewalls (close to the stem/thick segment interface) and when it is seated on the top of the NW with vertical sidewalls, may be different. In addition, it is clear that the Ga atoms having reached on the sidewalls of the stem can diffuse over the the stem/thick segment interface, especially in the case of the sharp transition. Therefore, the top thick segment radius  $R_e$  increases until the thick segment becomes long enough to provide the Ga current sufficient to stabilise the droplet volume.

## 4.4 Conclusions

To summarize, in this Chapter we developed procedures which allow one to reduce or enlarge locally the NW radius at will. Based on the understanding of the droplet dynamics during its consumption, discussed in Chapter 3, we can reduce deterministically the droplet base radius and then restart the growth. Such a growth sequence leads to form a NW significantly thinner than the stem. We achieved a sharp radius change

and managed to keep a thin segment over up to 300 nm length. The apical droplet of this segment recovers the same contact angle as during stem growth, although this angle was reduced to the much smaller Young's angle during the partial consumption. However, longer thin segments exhibit significant radial growth near the interface, and the radius then changes continuously over a length of several tens of nm.

If, instead, the NW is exposed to both group III and group V fluxes with a V/III ratio below one, the catalyst droplet inflates. At first, the droplet enlarges by increasing its contact angle  $\beta$ . Once  $\beta$  reaches a stable value, which depends on the V/III flux ratio, the NW radius starts to increase. Changing the fluxes again to provide a V/III ratio above one stabilizes the radius of the thick segment. Such a growth procedure results in the formation of a thicker NW segment on the top of a stem. The broadening achieved in such a transition appears to depend on the thin stem radius, with higher enlargement for NWs with thinner stems. The NW radius can triple for the very thin stems, while those with thicker stems have a top radius only 1.5 times larger. The transition between the thin and the thick segments is sharp for thin stems, but smoothly extended over a certain length for thick stems.

An important point is that these operations can be performed blindly in a standard MBE growth equipment. Although additional studies are necessary to fully understand the processes leading to the stabilization of the droplet geometry during inflation, we have demonstrated the possibility to realize sharp radius changes in a NW of a single material in both directions, from thick to thin and thin to thick. The combination of two these procedures will lead to formation of a diameter-modulated NW in a single growth run. It was unfortunately impossible to achieve this combination during the limited duration of this PhD.

# Chapter 5

## Geometrical limits for defect-free growth of core/shell nanowires

As discussed in Chapter 1, many NW applications require the core structure to be wrapped by a shell [6–8, 11, 12, 28]. Such a shell, often mismatched in order to modify the energy levels of the inner structure by applying some strain, should be grown defect-free. Although the fabrication of core/shell NWs has been extensively studied over the last years, the formation of a high-quality shell is still challenging. To shed more light on the problem of dislocation-free growth of core/shell NWs, in this Chapter, we address the limits and conditions of shell growth, which may lead to elastic or plastic relaxation of NW.

Firstly, we review the theoretical and experimental findings on the problem of elastic and plastic relaxation of a mismatched core/shell NW, published so far. We then introduce which type of interface misfit dislocations we will consider, and calculate the geometrical limits for the introduction of these dislocations, on the example of a GaAs/GaP core/shell NW. To do so, we use two approximations of the elastic properties of the system, namely elastic isotropy and transverse isotropy around the growth axis. We then compare our calculations with experimental results on GaAs/GaP core/shell NWs grown with various core radii and shell thicknesses. We discuss the optimisation of the experimental conditions, which we made to achieve the growth of a shell of high quality. Finally, we discuss which types of dislocation we observe and the differences with our models.

## 5.1 State of the art: Elastic and plastic strain in core/shell nanowires

When modelling the elastic or plastic strain state of a core/shell NW, one can make different assumptions. The NW shape, in general a more or less regular hexagonal cylinder, can be approximated as a circular or perfect hexagonal cylinder. The latter approximation has been so far treated only numerically. On the contrary, the problem of the strain and stress distribution in a NW with circular cross-section can be solved analytically. This treatment gives a more comprehensive understanding of the problem and the results are obtained more rapidly.

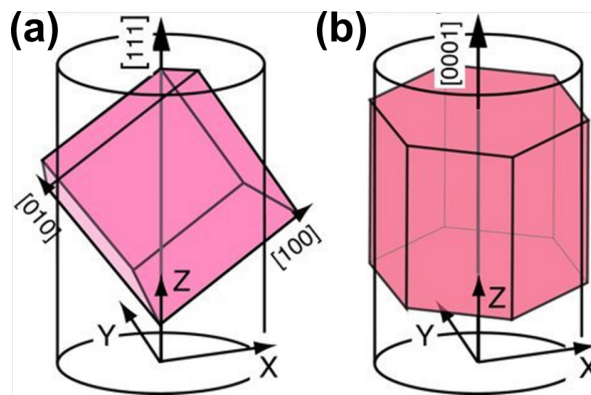


Figure 5.1: Schematic illustration of (a) a cubic ZB and (b) a hexagonal WZ unit cell with respect to the NW coordinate system with Z axis along the NW growth direction. The X, Y and Z depict the NW coordinate system, the other arrows show the crystallographic direction of ZB and WZ lattices. From [169]

In addition to the shape, the elastic properties of the NW materials should be defined. We limit ourselves to linear elasticity. The simplest approximation is to assume the core and the shell to be elastically isotropic. If one wishes to account more realistically for the anisotropy of the elastic properties of the core and the shell material, the crystallographic direction of the NW growth axis should be specified. As discussed in Section 1.2 of Chapter 1, III-V NWs can exhibit either ZB or WZ crystal structure and usually grow along the  $[111]$  or the  $c$  ( $[0001]$ ) axis, respectively (Figure 5.1). The elastic properties of the WZ structure exhibit the transverse isotropy about the  $c$ -axis. For the ZB structure along a  $[111]$  direction, the transverse anisotropy of the elastic properties is only an approximation. In both cases, it is customary to define a coordinate system with axis  $Z$  aligned with the NW growth axis.

Finally, regardless of cross-section and elasticity scheme chosen, the core/shell NW is often assumed to be infinite along its growth axis  $Z$ . This is a good approximation since the NW length is usually large compared to its diameter and one is not interested

in the strains at the NW top and bottom, unless one studies axial heterostructures.

### 5.1.1 Elastic strain state

We start by considering the case of a coherent core/shell interface, free of dislocations: strain relaxation is thus purely elastic. The problem of the strain state of two coaxial cylinders is not specific of NWs. Warwick and Clyne [170], extending the calculation of Mikata and Taya [171], developed an analytical model for a set of coaxial fibers subjected to thermal expansion or to external forces, in the assumption of transverse elastic isotropy. Trammel *et al.* [172], applying this model to core/shell Si/Ge NWs, considered transverse isotropy about the [001] direction and mentioned that quantitative conclusions for NWs grown along the [111] direction would be different. The same model was used in various studies of the elastic strain state of a WZ NW with [0001] axis [173–176], where transverse isotropy holds exactly, and adapted for isotropic NWs and for transversely isotropic ZB NWs about [001] and [111] axes [174, 176]. However, in these cases, the transverse isotropy is only an approximation. Raychaudhuri *et al.* [174] used the improper assumption of uniform strain components in the core and the shell, and the stiffness constants used in the calculation do not appear to be adapted to the claimed [111] NW growth direction.

There are several studies by Gutkin and co-workers [177–183] and other groups [184–186] of the strain distribution in core/shell system, in the frame of isotropic elasticity. The calculation, developed initially for mismatched core and shell with the same elastic constants [177–179, 182, 183, 186], was then extended to the case of two elastically different materials [180, 184, 185]. In addition, besides the cylindrical core/shell structure, some authors considered a cylindrical NW embedded in an infinite matrix [181] or the unlikely case of cylindrical NW with a rectangular core [183].

Ferrand and Cibert [106] provided a comprehensive study of the strain state of a circular cylinder core/shell NW, considering the ZB NW with [001] and [111] axes and the WZ NW with [0001] axis. In all three cases, the authors compared the analytical solutions in the transverse isotropic approximation and the numerical solution accounting for anisotropic elasticity. For ZB NWs with [111] growth axis in the anisotropic elasticity assumption, there are non-zero shear components of the strain, which are negligible in the core, but exist in the shell. Nevertheless, the authors showed that the transverse isotropic approximation reproduces excellently the results of the numerical solution for anisotropic elasticity.

Numerical calculations allow one easily to account for elastic anisotropy as well as for a hexagonal NW cross-section. A number of studies treated the problem of the

strain distribution in core/shell NWs of ZB structure with the [111] axis [169, 187–190] and of WZ structure with the [0001] axis [169, 191], applying finite elements and/or valence force field methods. Grönqvist *et al.* [188], in their joint finite elements and valence force field study of a hexagonal cross-section ZB NW, showed that tensile strain components dominate and that the shear components are small, yet not negligible. The same was concluded by Boxberg *et al.* [169] in their comprehensive treatment of ZB and WZ core/shell InAs/InP NWs with a circular cross-section: the shear strains in the shell are nonzero for a cubic NW, but zero for a WZ NW. They also noted that there is no significant quantitative differences in the tensile strains in NWs of different crystalline structures. Recently, Arjmand *et al.* [192] developed analytical and finite element calculations for a GaAs/InAs core/shell system along a [001] direction with circular or hexagonal cross-section. The authors used isotropic elasticity in the analytical calculation and accounted for elastic anisotropy in the numerical calculations. The comparison of the two solutions gave a good agreement, due to the fact that shear stress components are either negligible or equal to zero.

### 5.1.2 Plastic strain state

As in the cases of thin films on bulk substrates [193–196] and axial NW heterostructures [109, 197, 198], the strain in the core and the shell can be accommodated by the introduction of dislocations. Most of the aforementioned studies did not limit themselves to the calculations of the elastic strain state of a core/shell NW, but also dealt with such plastic relaxation [172–182, 186, 190, 192, 199, 200]. The aim of this kind of modelling is usually to find the limits of core/shell dimensions which would lead to plastic relaxation.

In doing so, one usually uses the Matthews-Blakeslee's criterion [194] adapted to the NW case. According to this criterion, the plastic relaxation occurs once the total energy of a system with one dislocation becomes lower than that of the coherent system. In the case of the growth of a thin film on a bulk substrate (2D case), the elastic energy scales linearly with the film thickness, whereas the energy of the thin film with the dislocation varies logarithmically with the film thickness. Therefore, the introduction of a dislocation is energetically favourable once the film thickness exceeds some critical value. This critical thickness depends on the elastic properties of the substrate and film materials, and on the type of the dislocation.

For the NW geometry, considering the core as the substrate and the shell as the thin film, this principle leads to the idea of a critical shell thickness, above which a dislocation will be formed, for a given core radius. But in contrast to the 2D case,

where the substrate thickness is almost infinite in comparison to that of the film, in a core/shell NW the core radius can be of the same order as the shell thickness and it is not fixed. So, reversing the Matthews-Blakeslee's criterion, for a given shell thickness, even very large, the introduction of a dislocation will be favourable only if the core radius surpasses some critical value. In other words, there exists some core radius, which allows the formation of a shell of infinite thickness without introduction of dislocations [110]. Of course, this critical radius depends on the elastic properties of the core and the shell, and it can be very small. In addition, the type of the dislocations and their position in the core/shell system affect the value of the radius for infinite defect-free shell growth.

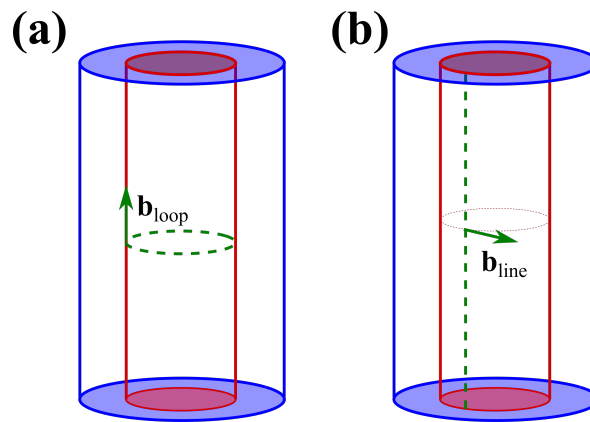


Figure 5.2: Schematics of a dislocation loop (a) and a straight off-axis dislocation (b) in a core/shell NW heterostructure.

Although the actual processes of plastic strain relaxation in core/shell structures are fairly complex [182, 201–204], in principle the strain can be relieved by forming two simple types of dislocation [110, 173, 174, 186, 205]. They are namely a dislocation loop, lying in the plane normal to the growth axis (Figure 5.2(a)) and a straight edge dislocation at the core/shell interface (Figure 5.2(b)). The Burgers vector of the loop dislocation  $\mathbf{b}_{loop}$  lies along the NW growth axis and that of the edge off-axis dislocation  $\mathbf{b}_{line}$  lies in the plane perpendicular to the NW growth axis. The loop and the edge dislocations thus relax the strain in the axial and normal tangential directions, respectively.

The partial relaxation of a core/shell system by the introduction of a dislocation loop has already been studied [173, 175, 176, 179, 186, 201]. The theoretical and experimental results of Salehzadeh *et al.* [176] indicated that loops should appear first. Indeed, they relieve the axial strain, which is present in both the core and shell, while radial and tangential strains are much weaker in the core. In the case of real ZB NWs grown in the [111] direction, several authors [201, 202] argue that the loops cannot glide

in the (111) plane since their Burgers vectors necessarily have components out of this plane. The loops should thus lie in inclined  $\{111\}$  planes.

Different assumptions for the Burgers vectors and elastic parameters of the core and the shell have led various authors to find rather different values of the NW geometrical limits for the introduction of a first dislocation loop, even for similar core-shell misfits. For instance, the limits computed by Salehzadeh *et al.* [176], who considered the Burgers vector to be a half the lattice constant along the Z axis ( $b = 0.35$  nm for an InAs/InP core/shell NW), are larger than those reported in Refs. [173, 174] for  $b$  equal to the lattice constant along the c [0001] direction in nitride WZ crystals. Haapamaki *et al.* [175], using the same value of the Burgers vector (the lattice constant along the growth axis) obtained critical dimensions almost 10 times smaller. In contrast to these studies, where the authors accounted for different elastic parameters of the core and the shell, in Refs. [179], [180] the calculations were performed for elastically identical core and shell. For the same core/shell misfit, the authors found slightly smaller geometrical limits than in Ref. [173, 174]. On the other hand, with elastically identical core and shell, Nazarenko *et al.* [186] reported an extremely large shell thickness for the introduction of a first dislocation loop (more than 100 nm for a core of 300 nm at a misfit of 2.7%). Interestingly, almost all of these studies [173–176, 186] claimed that their calculations reproduce the experimental results. However, only a limited range of dimensions were investigated experimentally.

As for the straight edge dislocation, we have several studies. In their theoretical analysis Smirnov *et al.* [183] showed that, independently of the NW dimensions, the optimal position of the straight dislocation is at the core/shell interface. This is to be expected and also in agreement with several previous analytical and finite elements calculations by Arjmand *et al.* [192] and Gutkin *et al.* [181] (the last study actually considered a wire embedded in an infinite matter).

Raychaudhuri *et al.* [173] stated the possibility of partial strain relaxation via the formation of a pure edge dislocation along the [0001] axis in WZ NWs, but not in ZB NWs grown along [111] direction, where such a dislocation is not stable [193]. Straight dislocations were actually observed at the core/shell interface in WZ InAs/GaAs core/shell NWs by Popovitz-Biro *et al.* [206].

As for the geometrical limits for the introduction of a first dislocation, in Ref. [173] the authors compared loops and straight dislocations and concluded that the straight edge dislocations should appear before the loops in WZ NWs. The opposite conclusion was reached by Nazarenko *et al.* [186] who found the loops to appear first due to their lower energy. However, the straight dislocation was considered to be located in the

shell, but not at the core/shell interface. Analysing only straight off-axis dislocations, Gutkin *et al.* [177] concluded that if the core radius and the shell thickness are of the same order, the dislocation either never forms, or, strangely, that its formation is energetically favourable only in a certain range of shell thicknesses; in particular, a thick shell should grow coherently. A similar surprising conclusion was made in Ref. [192]. The authors carried out extensive calculations for the off-axis straight dislocation along the [001] cubic axis, but predicted that for NWs with thin cores it is easier for a dislocation to form in a thinner shell, than in a thicker one. Nevertheless, the authors remarked that in practice the shell growth occur layer by layer, so dislocations may start to form in the thinner shell.

To try to clarify these questions, in the next sections, we develop calculations for the loop and straight off-axis dislocation and derive the geometrical limits for the introduction of each type of the dislocation. These limits are then compared with experimental results for a wide range of core and shell dimensions, in the case of GaAs/GaP core/shell NWs.

## 5.2 Elastic strain state of a core/shell nanowire

Before discussing the relaxation by introduction of a dislocation, let us first determine the elastic strain state of a core/shell mismatched NW with a coherent interface. As discussed in the previous section, this problem has been already solved in several studies under various assumptions on the geometry and elasticity of the system. Nevertheless, in our comparison of the total energies of the elastically and plastically relaxed core/shell NWs, we need to calculate both of them, and analytical formulae for the total energies have not been published so far even for the coherent situation. In addition, to compute the energy of a straight dislocation at the core/shell interface of the NW, we shall use the Peach-Koehler approach, which requires one to know the distribution of the stress field in the core/shell NW with a coherent interface (see Section 5.3.1). To this end, we now briefly outline the calculation scheme of the distribution of the strain, stress and elastic energy of a NW with a coherent core/shell interface.

In the present study, we ignore the faceting of the NW and approximate it as two infinite coaxial cylinders with radii  $R_c$  and  $R_s = R_c + H$ , for core and shell respectively (Figure 5.3). As for the elastic properties of the core (superscript  $c$ ) and the shell (superscript  $s$ ) materials, we consider linear elasticity and first use the simplest assumption (i) of the elastic isotropy of both. Each material has lattice constant  $a_0^n$  and its elastic properties can be characterized by shear modulus  $\mu^n$  and Poisson's ratio

$\nu^n$ , where  $n$  stays for  $c$  or  $s$ . The misfit thus writes:

$$\epsilon_0 = \frac{a_0^s - a_0^c}{a_0^c}. \quad (5.1)$$

However, the III-V materials, which we deal with in this study, are known to be elastically anisotropic and the isotropic approximation can only give qualitative conclusions. On the other hand, some structures can exhibit an elastic symmetry around certain crystallographic directions. For instance, WZ crystals are transversely isotropic about the [0001] axis [207]. On the contrary, ZB crystals are not transversely isotropic around the [111] axis, but transverse isotropy can be used as an approximation [106, 208]. This constitutes our assumption (ii), where the core and the shell materials have in-plane lattice constants  $a_r^n$  and lattice constants  $a_z^n$  along the [111] or [0001] axes. The core and shell elastic properties are given by the stiffness constants  $C^n$ . We assume equal misfits in plane and along NW axis:

$$\epsilon_0 = \frac{a_r^s - a_r^c}{a_r^c} = \frac{a_z^s - a_z^c}{a_z^c}. \quad (5.2)$$

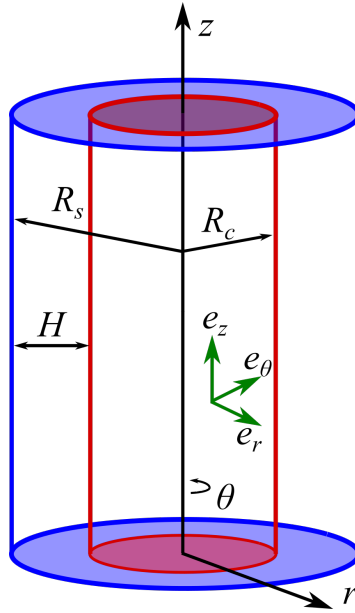


Figure 5.3: Geometry of a core/shell NW with radius  $R_s$ , core radius  $R_c$  and shell thickness  $H$  in the cylindrical  $(r, \theta, z)$  coordinate system.

Let us define a cylindrical coordinate system  $(r, \theta, z)$  with  $z$  the NW axis (Figure 5.3). Because of the geometrical and elastic axisymmetries (in both cases (i) and (ii)), the elastic strain does not depend on  $\theta$ , and because the NW is infinite along its axis, it does not depend on  $z$  either.

To calculate the distribution of elastic strain, we follow the two-step equilibration

process, proposed long ago by Eshelby [209] and applied to NWs in Ref. [172]. Initially, core and shell are in their stress-free (SF) states and are incoherent to each other. At the first step, the system is put in an intermediate coherent state by applying uniform forces (per unit area)  $F_i$  ( $i = r, \theta, z$ ) proportional to  $\epsilon_0$ . For convenience, we choose this intermediate state as the SF state of the core. The associated strains are

$$\begin{aligned}\epsilon_{rr}^{s,(1)} &= \epsilon_{\theta\theta}^{s,(1)} = \epsilon_{zz}^{s,(1)} = -\epsilon_0, \\ \epsilon_{rr}^{c,(1)} &= \epsilon_{\theta\theta}^{c,(1)} = \epsilon_{zz}^{c,(1)} = 0.\end{aligned}\tag{5.3}$$

The forces applied to the core are zero, while those applied to the shell can be found from Hooke's law, appropriate to cases (i) or (ii).

In the second step, we apply opposite forces and let the system relax to its final state while preserving the coherency of the core/shell interface. The corresponding strains  $\epsilon_{ij}^{n,(2)}$  are calculated from the displacements, using the usual formulae [210]. Since the NW is infinite, the axial displacement is zero and there is only a non-zero radial displacement, which we take as [106, 177]:

$$u_r^n = A^n r + \frac{B^n}{r},\tag{5.4}$$

with constants  $A^n$  and  $B^n$  for the core and the shell.

To determine these constants, we account for the following constraints:

1.  $u_r$  must remain finite on the NW axis, hence  $B^c = 0$ .
2. To preserve coherency, the step (2) displacements should be continuous at the interface:

$$u_r^c|_{r=R_c} = u_r^s|_{r=R_c}\tag{5.5}$$

3. The stresses developed at step (2), are those induced by the opposite of the forces applied at step (1). So, at the core/shell interface:

$$\sigma_{rr}^{c,(2)}|_{r=R_c} = \sigma_{rr}^{s,(2)}|_{r=R_c} - F_r^{s,(1)}|_{r=R_c}.\tag{5.6}$$

4. Since the NW is in mechanical equilibrium, the forces on the free surfaces should be zero. Therefore, for the outer NW surface

$$\sigma_{rr}^{s,(2)}|_{r=R_s} + F_r^{s,(1)}|_{r=R_s} = 0,\tag{5.7}$$

Coefficients  $A^c$ ,  $A^s$  and  $B^s$  are determined from the linear system (5.5) - (5.7). Although these coefficients can be derived in analytical form, their expressions are rather cumbersome, especially in the case of transverse isotropy, where the Hooke's law includes five different stiffness constant (see Section 5.4 of the current Chapter). The analytical expressions for these coefficients can be found in Ref. [177] for isotropic elasticity and in Ref. [106] for transverse isotropic elasticity. We solve this linear system numerically in the elastic isotropy and transverse elastic isotropy cases. Obviously, the coefficients depend on the dimensions of the core/shell structure, as well as on the misfit  $\epsilon_0$  and on the elastic properties of the materials.

Finally, the total elastic strain with respect to the initial stress-free state writes

$$\epsilon_{ij}^n = \epsilon_{ij}^{n,(1)} + \epsilon_{ij}^{n,(2)} \quad (5.8)$$

The total stresses  $\sigma_{ij}^n$  are found from the strains using Hooke's law.

Once the coefficients are calculated, the distribution of strain can be determined by substituting Eqs. (5.4) and (5.3) in Eq. (5.8). Figure 5.4 illustrates the distribution of the strain components for a GaAs/GaP core/shell NW with respect to the initial SF state in approximation (i). The shell lattice constant is smaller than that of the core by 3.6%. The panels (a)-(c) depict the strain components of the NW with a core radius of 10 nm and a shell thickness of 5 nm, and the panels (d)-(e) those of the NW with a core radius of 10 nm and a shell thickness of 20 nm.

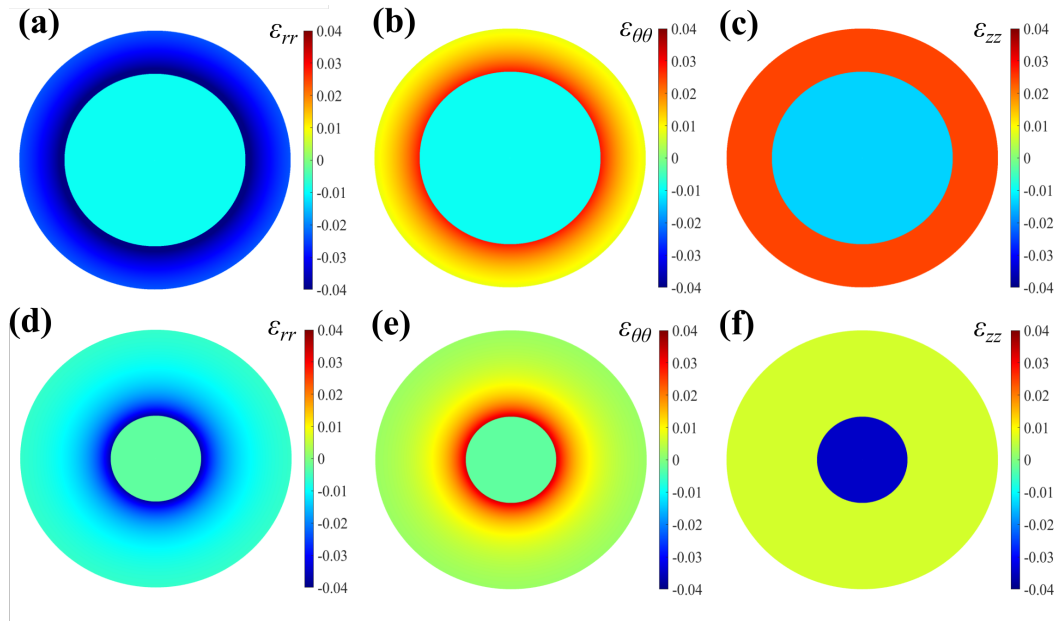


Figure 5.4: Distribution of the strain components  $\epsilon_{rr,\theta\theta,zz}$  in GaAs/GaP core/shell NW with core radius  $R_c = 10$  nm and shell thickness  $H = 5$  nm (a-c) and  $H = 20$  nm (d-f) within isotropic elasticity approximation. The lattice misfit is 3.6%

The GaAs core having a larger lattice constant is under uniform compression in all directions. The radial  $\varepsilon_{rr}$  and tangential  $\varepsilon_{\theta\theta}$  strain components in the core are uniform as expected due to the symmetry. The shell region is under tensile strain in axial and tangential direction, while it is compressed in the radial directions. This results from of Eq. (5.7). The in-plane strains  $\varepsilon_{rr}$  and  $\varepsilon_{\theta\theta}$  are mostly localized in the shell region and decrease rapidly in the shell away from the interface, over a distance of the order of the core radius  $R_c$  (panels (a), (b), (d), (e) in Figure 5.4). On the other hand, the axial strain  $\varepsilon_{zz}$  is shared between the core and the shell. For a modest shell thickness (*e.g.*  $H/R_c = 0.5$ , Figure 5.4(c)), the shell region accommodates much more strain than the core. In the extreme case  $H \ll R$ , this geometry resembles the 2D case, with the strain mainly localized in the shell (which plays the role of a thin film on the thick substrate). When shell thickness increases (*e.g.*  $H/R_c = 2$ , Figure 5.4(f)), the axial strain localizes mainly in the core.

Let us now calculate the total energy associated with this strain state. Since we assume a NW of infinite length, it is appropriate to characterize it by the energy per unit length along the axial direction,  $W_{NW}^{coh} = W_c + W_s$ , where  $W_c$  and  $W_s$  are the total energies per unit length of core and shell, respectively. They write:

$$\begin{aligned} W_c &= \frac{1}{2} \int_0^{2\pi} \int_0^{R_c} \sigma_{ij}^c \varepsilon_{ij}^c r dr d\theta, \\ W_s &= \frac{1}{2} \int_0^{2\pi} \int_{R_c}^{R_s} \sigma_{ij}^s \varepsilon_{ij}^s r dr d\theta. \end{aligned} \tag{5.9}$$

Here, the summation over  $i, j = r, \theta, z$  is implied.

Similarly to the 2D case, the total elastic energy increases with the shell thickness and at some critical shell thickness  $h_{crit}$  it becomes high enough for the formation of a dislocation to be energetically favourable. As discussed in Section 5.1.2, for a fixed shell thickness, it also exists a critical core radius  $r_{crit}$ , above which the dislocation will be introduced. The reason of the existence of such a critical radius can be seen in Figure 5.4. The in-plane strain components in the elastically strained shell extend only over a distance of the order of the core radius  $R_c$ . For a very large shell thickness ( $H \gg R_c$ ), the axial strain is hence mostly accommodated by the core. In this case the total elastic energy scales with  $R_c^2$ , independently of the shell thickness  $H$ . Thus, for thin enough cores the elastic energy of the coherently grown system can be lower than that of the system with a dislocation. To this energy one has to add the dislocation core energy  $W_{dc}$  to obtain the total energy of the system.

## 5.3 Partial relaxation by dislocation formation

As mentioned in Section 5.1.2, we consider the possible relaxation of the core/shell NW by introduction of two types of dislocation. The formation of a dislocation modifies the strain field in the NW and thus changes the elastic energy. Let us discuss, how a dislocation changes the elastic energy and how these changes can be quantified.

In general, the elastic energy stored in a NW with a dislocation can be written as:

$$W_{NW}^{disl} = W_{NW}^{coh} + W_{self} + W_{gain}. \quad (5.10)$$

Here  $W_{NW}^{coh}$  is the elastic energy of the coherent NW (calculated in Section 5.2),  $W_{self}$  is the self-energy cost the dislocation (*i.e.* the strain energy of the dislocation in the SF material) and  $W_{gain}$  accounts for the energy lowering due to the effective misfit reduction by the dislocation. The last two terms in Eq. (5.10) should be specified for each type of dislocation.

### 5.3.1 Straight edge dislocation

Let us first consider a straight dislocation formed off-axis at the core/shell interface. This position seems the most efficient as regards relaxation. Since we assume a NW of infinite length along its growth direction, the strain distribution will be uniform along the growth axis. We can thus calculate the self-energy of the straight dislocation  $W_{self}^{line}$  in the frame of the plain strain problem, using the Airy stress function method [210]. This analytical method allows one to place the straight dislocation at the core/shell interface as well as to calculate the strain and stress distributions in presence of several dislocations [211]. Gutkin *et al.* [177] proposed an Airy stress function for such a dislocation at position  $(R_c, \theta_0)$  in a cylinder of radius  $R_s$ . Due to the geometrical and elastic symmetry, all positions at the core/shell interface are equivalent. For simplicity, we place a dislocation at  $(R_c, \theta_0 = 0)$  (Figure 5.5(a)). The Gutkin/Romanov Airy stress function then writes:

$$\chi = \frac{K_{line}}{4\pi} b_{line} \sin \theta \left[ r \ln \frac{\alpha^2 r^2}{\beta^2 R_s^2} + \frac{R_s^2 \alpha^2}{r \beta^2} \right] \quad (5.11)$$

where  $\alpha^2 = R_c^2 - 2R_c r \cos \theta + r^2$ ,  $\beta^2 = R_c^2 - \frac{2R_c R_s^2}{r} \cos \theta + \frac{R_s^4}{r^2}$  and  $K_{line}$  is a coefficient related to the elastic properties and the crystal structure of the NW material. The modulus of the Burgers vector  $\mathbf{b}_{line}$  is taken as  $a_s/\sqrt{2}$ . This corresponds to the smallest lattice translation in cubic materials.

The corresponding stress components can be found by derivating of the Airy func-

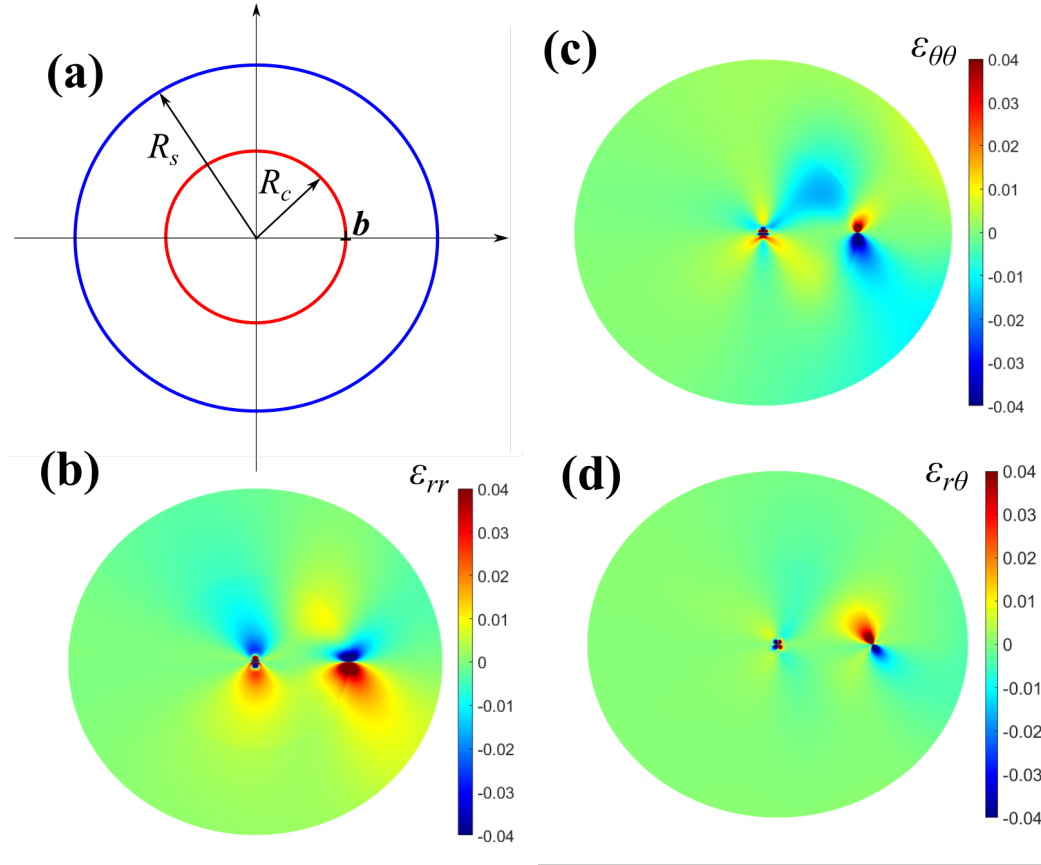


Figure 5.5: (a) Off-axis position  $(R_c, \theta_0)$  of a straight dislocation in a core/shell NW. (b)-(d) Distribution of the strain components  $\varepsilon_{ij}$  in a GaAs/GaP core/shell NW with core radius  $R_c = 10$  nm and shell thickness  $H = 10$  nm, within isotropic elasticity approximation. The lattice misfit is 3.6%

tion  $\chi$ , and strains  $\varepsilon_{ij}^{n,disl}$  are computed using the Hooke's law. Note that the introduction of a single off-axis dislocation breaks the cylindrical symmetry, which results in non-zero shear components  $\sigma_{r\theta}$  and  $\varepsilon_{r\theta}$ .

Figure 5.5(b-d) depicts the distribution of the strain components in the core/shell NW with the straight dislocation at the core/shell interface. The strains are calculated using the approximation (i) of isotropic elasticity. The strain is mostly concentrated around the dislocation, going to infinity at the dislocation position. Strangely, the proposed Airy stress function also gives a huge concentration of strain at the NW axis. As discussed in Section 5.1.2, the authors of Ref. [177], using this Airy stress function to calculate the total energy of a core/shell NW with an off-axis dislocation, surprisingly concluded that the formation of such a dislocation is favourable only in some intermediate range of shell thickness, if the core radius and shell thickness are of the same order. The distribution of neither strain nor stress were however given. Considering these problems, the use of the Airy stress function (5.11) should be reconsidered.

A much simpler option, albeit less satisfactory in principle, is to compute the self-energy  $W_{self}^{line}$  by using the formula for a 2D film on a substrate with the film thickness replaced by the shell thickness  $H$  [193]:

$$W_{self}^{line} = \frac{K_{line}}{4\pi} b_{line}^2 \ln \frac{H}{r_0} \quad (5.12)$$

where  $r_0$  is the cut-off radius that eliminates the mathematical singularity. This cut-off radius is introduced to exclude the highly disturbed core region where elasticity cannot be applied. For fcc semiconductor materials this value is often set to  $r_0 = b_{line}/4$  [193, 212, 213]. One adds the energy per unit length of the dislocation core [193], which may be taken as:

$$W_{dc} = K_{line} \frac{b_{line}^2}{4\pi}. \quad (5.13)$$

For the energy lowering due to the presence of a dislocation  $W_{gain}$ , Peach and Koehler [214] proposed to compute it as the opposite of the work performed by the coherent strain field upon moving the dislocation from the edge of the system to its final position. This method has been applied to the analysis of the dislocation positions and energies in Stranski-Krastanow GeSi islands [215–217] and in NW heterostructures with an axial composition gradient [218]. Indeed, a dislocation line extending in the  $\mathbf{l}$  direction with Burgers vector  $\mathbf{b}_{line}$  plunged in the stress field  $\hat{\sigma}$  experiences the Peach-Koehler force [214]:

$$\mathbf{F} = \mathbf{b}_{line} \cdot \hat{\sigma} \times \mathbf{l}. \quad (5.14)$$

$W_{gain}$  is calculated as the work performed by force  $\mathbf{F}$  while moving the dislocation from the outer surface  $s$  to the inner dislocation position  $c$  along path  $\mathbf{p}$ . This energy writes:

$$W_{gain} = - \int_s^c \mathbf{F} d\mathbf{p} \quad (5.15)$$

It is important to note that  $W_{gain}$  is independent of the integration path  $\mathbf{p}$ . On the other hand,  $W_{gain}$  varies with the final position of the dislocation  $c$ .

For our straight dislocation with Burgers vector  $\mathbf{b}_{line}$  normal to  $Z$  (Figure 5.6(a)), from Eq. (5.15) the work done by the Peach-Koehler force to move this dislocation from the outer NW surface to the interface can be calculated for instance by choosing a simple path along the  $Y$  axis (at  $X = 0$ ):

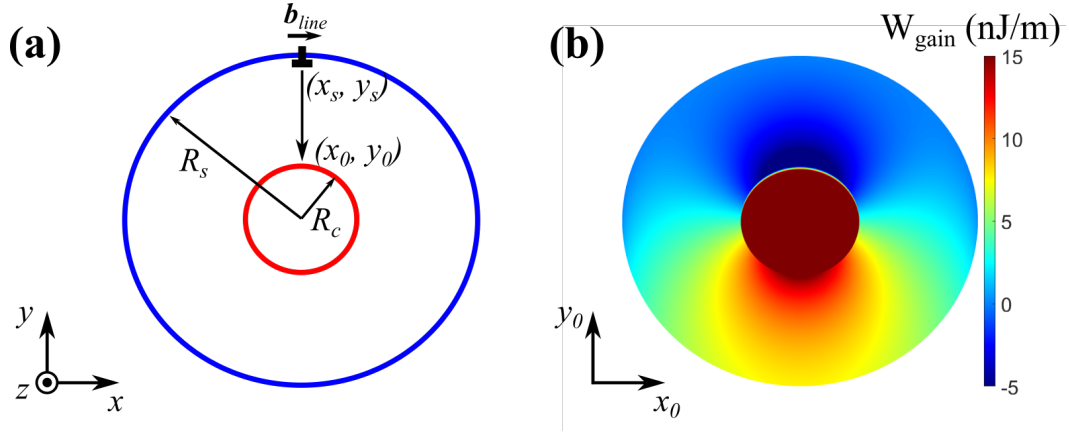


Figure 5.6: (a) Schematics of the displacement of the straight dislocation with Burgers vector  $\mathbf{b}_{line}$  from the outer surface to an arbitrary point in the core/shell NW. (b) Distribution of the elastic energy lowering  $W_{gain}(x_0, y_0)$  for dislocation motion from the fixed point  $(x_s, y_s)$  on the NW outer surface to an arbitrary point  $(x_0, y_0)$  in the NW. The values of  $W_{gain}(x_0, y_0)$  are given for the case of a GaAs/GaP core shell NW with core radius  $R_c = 10$  nm and shell thickness  $H = 20$  nm.

$$W_{gain}^{line}(x_0, y_0) = -b_x \int_{y_s}^{y_0} \sigma_{xx} dy - b_y \int_{y_s}^{y_0} \sigma_{xy} dy \quad (5.16)$$

with  $b_x, b_y$  are the components of the Burgers vector  $\mathbf{b}_{line}$  along the  $X$  and  $Y$  directions. Figure 5.6(b) shows the distribution of  $W_{gain}^{line}(x_0, y_0)$  for the straight dislocation motion with Burgers vector  $\mathbf{b}_{line} = (a_0^s/\sqrt{2}, 0)$ , when the dislocation is moved from the fixed point on the outer surface to an arbitrary point in the core/shell GaAs/GaP NW. As can be seen, the largest reduction of the elastic energy is obtained when the dislocation is placed at the NW core/shell interface. The minimum of the sum of  $W_{gain}^{line}$  and  $W_{self}^{line}$  gives the most efficient position of the dislocation. Because the self-energy decreases when the dislocation is moved towards the outer NW sidewall, it will be slightly displaced from the interface inside the shell.

### 5.3.2 Dislocation loops

For the dislocation loop with Burgers vector  $\mathbf{b}_{loop}$  along the NW growth direction, the self-energy writes [179]:

$$W_{loop} = \frac{K_{loop}}{2} R_c b_{loop}^2 \left( \ln \frac{8R_c}{r_0} - 2 + J(R_c, H) \right) \quad (5.17)$$

where  $K_{loop}$  is a coefficient related to the elastic properties of the NW material (see Section 5.4 of this Chapter), and  $r_0 = b_{loop}/4$  is the cut-off radius that eliminates a

mathematical singularity at the dislocation core. The first two terms in the brackets give the self-energy of the dislocation loop in an infinite media [193] and the last term is the correction factor due to the finite cylinder geometry [179]. As in the case of the straight dislocation, we add the energy of the dislocation core (Eq. (5.13) with proper energy coefficient  $K_{loop}$ ). The modulus of the Burgers vector  $\mathbf{b}_{loop}$  is taken as  $a_s/\sqrt{3}$ , which corresponds to the thickness of a ML along [111] cubic and [0001] hexagonal directions (see Section 1.2 of Chapter 1).

The energy lowering  $W_{gain}^{loop}$  due to the presence of the dislocation can be calculated using again Peach-Koehler approach, as done for the straight off-axis dislocation in the previous section. The details of these calculations and the expression for  $W_{gain}^{loop}$  in a core/shell NW with elastically isotropic and core and shell with identical elastic constants are presented in Ref. [179].

## 5.4 Crystalline structure of nanowires

To calculate the elastic energies, corresponding to a particular strain state of a core/shell NW, we should specify the elastic properties of the core and shell materials. Let us assume a NW with the core and the shell both of ZB structure. The stiffness tensor  $\hat{C}$  of this cubic crystal contains three independent parameters. In Voigt notation for cubic axis, it writes:

$$\begin{pmatrix} C_{11} & C_{12} & C_{12} & 0 & 0 & 0 \\ C_{12} & C_{11} & C_{12} & 0 & 0 & 0 \\ C_{12} & C_{12} & C_{11} & 0 & 0 & 0 \\ 0 & 0 & 0 & C_{44} & 0 & 0 \\ 0 & 0 & 0 & 0 & C_{44} & 0 \\ 0 & 0 & 0 & 0 & 0 & C_{44} \end{pmatrix} \quad (5.18)$$

The anisotropy of the cubic structure is clear (usually,  $C_{44} \neq \frac{C_{11}-C_{22}}{2}$ ), which results in the developing of non-zero shear components of the strain  $\varepsilon_{ij}, i \neq j$  and the stress  $\sigma_{ij}, i \neq j$  [169]. For isotropic elasticity (approximation (i)), we assume  $C_{44} = \frac{C_{11}-C_{22}}{2}$ , which gives shear modulus  $\mu$  and Poisson's ratio  $\nu$  [84, 193]:

$$\begin{aligned} \mu &= \frac{C_{11} - C_{12}}{2} \\ \nu &= \frac{C_{12}}{C_{11} + C_{12}} \end{aligned} \quad (5.19)$$

Recently, Arjmand *et al.* [192] compared the analytical solution for the strain state

of the coherent core/shell NW in isotropic approximation (i) with a finite element simulation, accounting for the cubic elastic anisotropy. The authors showed that the shear stresses  $\sigma_{r\theta} = \sigma_{z\theta} = 0$  and  $\sigma_{rz}$  are negligible.

But, as mentioned in Section 1.1 of Chapter 1, the ZB III-V NWs usually grow in a [111] direction. To account for this, and thus model the strain state of a NW with the  $Z$  axis along a [111] cubic direction (as in Figure 5.1(a) on page 70), the stiffness tensor (5.18) must be expressed in the relevant axes. This operation is well known, and consists in the multiplication of initial stiffness tensor by rotational matrix, corresponding to the desired directions [193, 208]. Without going into details, we transform the stiffness tensor (5.18) into the basis defined by  $x = [1\bar{1}0]$ ,  $y = [11\bar{2}]$  and  $z = [111]$ , as in Refs. [106, 188, 207]. The stiffness tensor writes [106]:

$$\begin{pmatrix} C'_{11} & C'_{12} & C'_{13} & C'_{14} & 0 & 0 \\ C'_{12} & C'_{11} & C'_{13} & -C'_{14} & 0 & 0 \\ C'_{13} & C'_{13} & C'_{33} & 0 & 0 & 0 \\ C_{14} & -C'_{14} & 0 & C_{44} & 0 & 0 \\ 0 & 0 & 0 & 0 & C'_{44} & C'_{14} \\ 0 & 0 & 0 & 0 & C'_{14} & \frac{C'_{11}-C'_{12}}{2} \end{pmatrix} \quad (5.20)$$

For our analysis of the total elastic energies, we neglect  $C'_{14}$  due to its quite small relative value ( $C'_{14}/(C'_{11} + 2C'_{12}) \approx -0.05$  for GaAs and GaP). As shown by Ferrand and Cibert [106], such an approximation reproduces excellently the numerical results, wherein the  $C'_{14}$  term is included.

Table 5.1: Values of the elastic parameters of GaAs and GaP of [001]-oriented and [111]-oriented ZB structures. For [001] orientation the stiffness constants  $C_{ij}$ , and shear modulus  $\mu = (C_{11} - C_{12})/2$  and Poisson's ratio  $\nu = C_{12}/(C_{11} + C_{12})$  for isotropic elasticity approximation are given [219, 220]. For [111] orientation the stiffness constant  $C'_{ij}$  are calculated from those for [001] orientation using the rotation rules [106, 193]. All values, except Poisson's ratio  $\nu$  are given in GPa.

<b>ZB [001]</b>	$C_{11}$	$C_{12}$	$C_{44}$	$\mu$	$\nu$	
GaAs	119.0	53.8	59.5	32.8	0.31	
GaP	140.5	62.1	70.3	39.2	0.31	
<b>ZB [111]</b>	$C'_{11}$	$C'_{12}$	$C'_{13}$	$C'_{14}$	$C'_{33}$	$C'_{44}$
GaAs	145.6	44.9	36.1	-12.5	154.5	41.5
GaP	171.6	51.7	41.4	-14.7	182.0	49.6

We can now determine the energetic coefficients appearing in Eqs. (5.17), (5.13), (5.11) and (5.12). In isotropic elasticity, the coefficients  $K_{loop}$  and  $K_{line}$  can be expressed in terms of shear modulus  $\mu$  and Poisson's ratio  $\nu$  [193]:

$$K_{line} = K_{loop} = \frac{\mu}{1 - \nu}. \quad (5.21)$$

To consider the anisotropy of elastic properties of ZB NWs, we use the approach proposed by Eshelby *et al.* [221] and Foreman [222] to calculate the energy coefficient for a dislocation with a Burgers vector of a given orientation in an anisotropic media. For the straight dislocation with Burgers vector along  $[1\bar{1}0]$  direction in  $[111]$  oriented ZB structure, the elastic properties of which are defined by the stiffness tensor (5.20), we find the energy coefficient  $K_{line}$ :

$$K_{line} = (C'_{11} + C'_{12}) \left[ \frac{C'_{66} (C'_{11} - C'_{12})}{C'_{11} (C'_{11} + C'_{12} + 2C'_{66})} \right]^{1/2} \quad (5.22)$$

where  $C'_{66} = \frac{C'_{11} - C'_{12}}{2}$ .

In the next section, we compare the total energies of the core/shell GaAs/GaP NW in the elastic and plastic strain states, using the values of the elastic constants summarized in Table 5.1.

## 5.5 Geometrical limits for dislocation formation

We can now compute the geometrical limits for the formation of each type of dislocation. To do so, we compare the elastic energy of the coherently strained NW with that of the NW partially relaxed by the introduction of a first dislocation. We focus on the formation of the first dislocation, either loop or straight, and carry out the analysis separately for each type of dislocation. Since in our model we assume a NW of infinite length, we compare the total energies per unit length. In the case of the loop, we compute the energy over a length large with respect to the NW radius  $R_s$ , namely  $L = 100 R_s$ , from which we then calculate the energy per unit length. We compute the geometrical limits for the introduction of a first dislocation loop within the approximation (i) of elastically isotropic core and shell, and those for the straight off-axis dislocation in the two approximations of isotropy and transverse isotropy about  $[111]$  ZB direction.

Figure 5.7(a) plots the total energy of the NW without dislocation (solid curve) and with a first loop (dotted curve) or straight dislocation (dashed curve), as a function of the shell thickness, for a fixed core radius  $R_c = 15$  nm. The intersection points (shown by the arrows) represent the shell thickness above which it is energetically favourable for the NW to form a dislocation rather than increase the shell thickness coherently. These points give the critical shell thickness  $h_{crit}$  below which a shell will

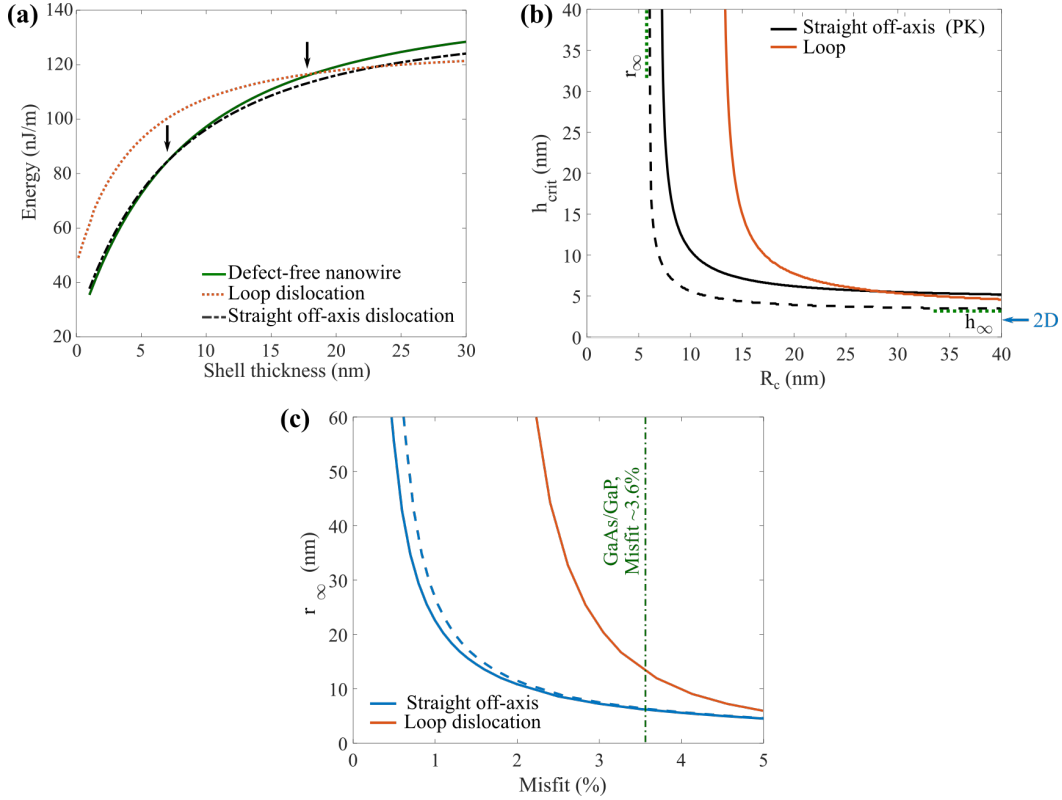


Figure 5.7: (a) Total energy of GaAs/GaP core/shell NW with or without loop or straight off axis dislocation, as a function of the shell thickness. The core radius is fixed at  $R_c = 15$  nm, Burgers vector is  $b_{loop} = a_0^s/\sqrt{3}$  for the loop dislocation and  $b_{line} = a_0^s/\sqrt{2}$  for the straight dislocation. The arrows show the critical shell thickness  $h_{crit}$  above which the introduction of a dislocation is energetically favourable. (b) Calculated geometrical limits for dislocation-free growth of the GaAs/GaP core/shell NW. The full curves show the limits for the isotropic elasticity approximation, the dashed curve those for a ZB NW grown in the [111] direction. Limits for the introduction of each type of dislocation are treated separately.  $r_\infty$  is the NW radius below which an arbitrary thick dislocation-free shell can be formed.  $h_\infty$  is the maximum shell thickness that can be formed around an arbitrary thick core without introduction of a dislocation. (c) Core radius  $r_\infty$  as a function of the lattice mismatch between the core and the shell materials.

grow without defects on a NW with a given core radius. Performing the same energy analysis for various sets of core radii and shell thicknesses leads to a complete set of geometric limits for the NW coherent growth. We perform the calculation numerically by varying the core radius and the shell thickness by steps of 0.1 nm. The results are for a NW comprised of a GaAs core and a GaP shell. In Figure 5.7(b), the black curves show the critical thickness as a function of the core radius for the straight off-axis dislocation and the red curve shows the same quantity for the loop dislocation. For the straight dislocations, the full curve gives the limits computed in the isotropic elasticity approximation, and the dashed one those for a transversely isotropic ZB NW with a

[111] axis. The vertical asymptote of each curve gives the core radius  $r_\infty$  below which a core/shell NW will grow coherently regardless of the shell thickness. For instance, in the case of isotropic elasticity, this critical radius for infinite dislocation-free shell thickness is  $r_\infty = 12.9$  nm for the loop dislocation and  $r_\infty = 6.8$  nm for the straight off-axis dislocation. With the more realistic assumption of a core/shell NW grown along a [111] direction, these limits are smaller, which results from the difference of the elastic constants. For the straight off-axis dislocation, it is  $r_\infty = 5.9$  nm.

The existence of such a core radius results from the core/shell structure ability to distribute the strain between the core and the shell. As shown in Section 5.2, the strain in the shell localizes over a distance comparable to the core radius. Also, with the shell thickness increasing, most of strain passes to the core. Since the core volume stays constant, the total elastic energy of the core/shell system no longer changes with the shell thickness. For sufficiently thin cores, the elastic energy stored in the core and in the shell region around it will never exceed that resulting from the formation of a dislocation. Thus, the area below the curves on the Figure 5.7(b) defines the combination of core/shell dimensions that yield a dislocation-free growth. The relative positions of the curves associated with the loop and the straight dislocation imply that strain should be first relieved by the formation of a straight dislocation.

The asymptotes of the curves at large  $R_c$  in Figure 5.7(b) gives the shell thickness  $h_\infty$  that can be grown around an arbitrary thick core without forming a dislocation. With the core radius increasing, this value converges to the critical thickness of a 2D thin film grown on a bulk substrate, which is of 3.6 nm for GaP grown on GaAs substrate [223]. Under the assumption of elastic isotropy, we find  $h_\infty = 4.9$  nm for the loop dislocation and  $h_\infty = 5.5$  nm for the straight off-axis dislocation. For the [111]-oriented NW, this value decreases to 3.8 nm for the straight off-axis dislocation.

Evidently, the value of  $r_\infty$  depends primarily on the lattice misfit  $\epsilon_0$  between the core and the shell materials, since the elastic energy comprises terms scaling with  $\epsilon_0^2$  or  $\epsilon_0$ . Figure 5.7(c) reports the variation of  $r_\infty$  as a function of lattice mismatch between the core and the shell material. Full curves relate to elastically isotropic materials and the dashed curve to [111]-oriented ZB. Interestingly, the radius for infinite dislocation-free shell thickness, being different for loop and straight dislocation in the NWs with low misfit, tends to a single value for the two types of dislocations at large misfit.

## 5.6 Actual growth of mismatched core/shell nanowires

In order to compare our calculations with experimental results, we have grown a series of specific GaAs/GaP core/shell NWs. In each experiment, the growth conditions were adjusted in order to obtain an adequate variation of core and shell dimensions.

### 5.6.1 General procedure for core/shell nanowire growth

Figure 5.8 illustrates the various steps in the formation of a core/shell structure. The core growth is similar to that discussed in the previous chapters, starting with Ga droplet pre-deposition (Figure 5.8(a)) and further NW growth in the VLS mode (Figure 5.8(b)). The catalyst droplet is then consumed by providing only the group V flux (Figure 5.8(c)). This leads to the formation of a top segment as well as of a thin shell due to the presence of group III back diffusion, as shown in Section 3.4 in Chapter 3.

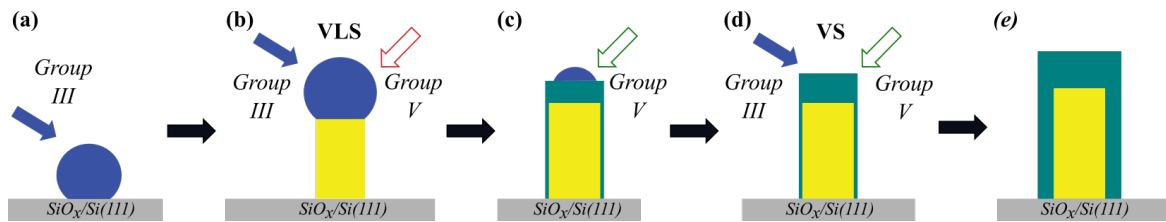


Figure 5.8: Schematics of the growth sequence of a core/shell NW.

A shell of controlled thickness is then grown in the VS mode under both group V and group III fluxes (Figure 5.8(d)). During this step, the NW also undergoes a small axial growth (Figure 5.8(d)). The substrate temperature and the V/III flux ratio can be set to values different from those used during the core growth. In the next sections, we will discuss each step of the core/shell NW growth and describe the influence of growth conditions on the dimensions, composition and crystal quality of the core and the shell.

### 5.6.2 Growth of the thin core

As predicted by the theory (see Section 5.5), NWs with an extremely thin core can be overgrown with an arbitrary thick mismatched shell without the formation of any dislocation. In the VLS growth mode, the NW diameter is mostly defined by the initial diameter of the catalyst droplet. But the growth of NWs with very thin radii, which subsequently serve as cores, is quite challenging.

In order to obtain thin cores, we investigated the growth of GaAs and GaP NWs on a Si(111) substrate covered by a native  $\text{SiO}_x$  layer. The details of the substrate

preparation can be found in Section 2.3.1 of Chapter 2. In order to vary the distribution of NW diameter, we change the amount of Ga atoms provided during the pre-deposition step and the V/III flux ratio during NW growth. Since the growth occurs on a non-patterned substrate, there is no preferential area for droplet formation. Assuming a uniform distribution of Ga adatoms on the substrate, we can thus characterize the pre-deposition by the mean total surface density of Ga atoms deposited. This value is calculated by simple multiplication of the equivalent 2D growth flux by the time of pre-deposition.

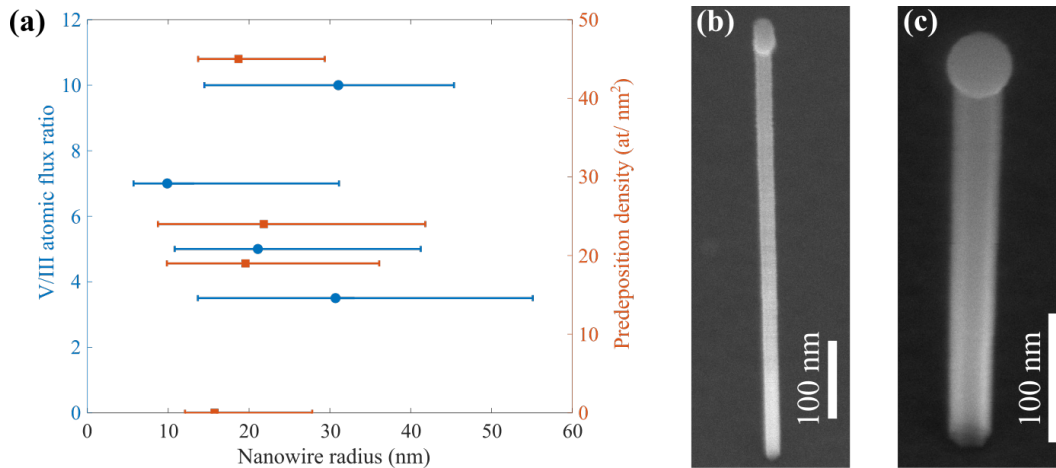


Figure 5.9: Growth of a thin core: (a) NW radius dependence on the V/III flux ratio (blue circles and lines, left axis) and on Ga atom pre-deposition density (red squares and lines, right axis). The symbols represent the median value of  $\sim 70$  NWs analysed for each set of growth conditions and the lines the width of the distribution. The samples with varying V/III flux ratios were grown at a fixed Ga pre-deposition atom density of  $19 \text{ at/nm}^2$ . The samples with varying Ga pre-deposition atom density were grown at a fixed V/III flux ratio of 5. The growth time was 10 min for all the samples. (b) SEM image of a GaAs NW with a radius of 11 nm. (c) SEM image of a GaP NW with a radius of 16 nm.

At fixed pre-deposition atom density, an increase of the V/III flux ratio reduces the mean NW radius and increases the proportion of NWs with small radius (blue circles and lines in Figure 5.9(a)). Half of the GaAs NWs grown at a V/III ratio of 7 exhibits a radius below 11 nm. On the other hand, the density of NWs decreases at higher V/III flux ratio, and drops significantly at a V/III flux ratio of 10. This low density also affects the distribution of NW radii, increasing its median value. The variation of pre-deposition atom density affects marginally the NW radius (red squares and lines in Figure 5.9(a)). Less pre-deposition leads to slightly thinner NWs, but at the same time decreases the density of droplets. Without pre-deposition, the distribution of the NW radius does not change much.

Figure 5.9(b,c) shows SEM images of a GaAs and a GaP NW, grown with pre-

deposition of 19 at/nm<sup>2</sup> and at the V/III flux ratio of 7. Interestingly, the catalyst droplet on the top of NWs with radius below 13 nm partially falls on the sidewalls (Figure 5.9(b)), while thicker ones (Figure 5.9(c)) do not exhibit this feature.

### 5.6.3 Catalyst droplet consumption and shell growth

As discussed in Chapter 3 for GaP NWs, the catalyst droplet consumption under phosphorous leads to axial and radial growth, creating a top NW segment and a thin unintentional shell several nanometres thick. A careful choice of the droplet crystallization conditions is crucial for growing a shell of given thickness and composition. For the GaAs cores used in this particular study, we tested droplet consumption under either As or P.

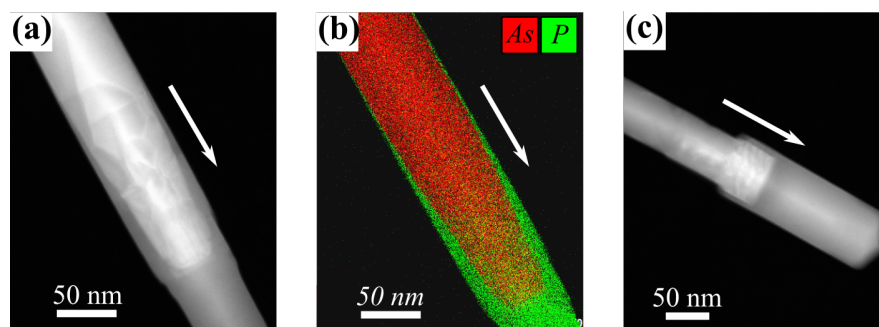


Figure 5.10: Catalyst droplet crystallization during the GaAs/GaP core/shell NW growth: (a) HAADF TEM image of a NW with droplet crystallized under As flux. (b) EDX map of a chemical composition of the same NW. (c) HAADF TEM image of the NW with droplet crystallized under P flux. The GaAs core appears bright, the GaP top layer and shell darker. White arrows indicate the NW growth direction

The droplet consumption can produce either core or shell material. If the droplet is consumed under arsenic, we observe the growth of a tapered additional core segment with a truncated top due to droplet shrinking during consumption. On the contrary, after droplet consumption under phosphorous, the core ends with a flat top. Figure 5.10 shows the example of these two types of catalyst consumption for GaAs/GaP core/shell NWs. In these samples, after the GaAs core growth at the V/III flux ratio of 7, the Ga droplet was consumed by providing during 30 min either only As, and thus forming a top segment of GaAs (panels (a) and (b) of Figure 5.10), or only P, then forming a top segment of GaP (panel (c) of Figure 5.10). This relatively long consumption time was chosen in order to insure the total droplet consumption. Since the droplet is the only source of Ga atoms, an excessive consumption time does not affect at all the dimensions of the grown segments.

The tapered core end results in the formation of an unintentional shell of inhomogeneous thickness around it (Figure 5.10 (a)), which can make the final shell thickness less controllable. On the contrary, the droplet consumption using a group V species different from that of the core creates a uniform shell around the core top (Figure 5.10 (c)). The formation of a non-uniform shell can disturb our analysis of the shell thickness at which a first dislocation is formed. We thus use the second consumption technique.

Contrary to the core, grown in VLS mode, the NW shell is usually grown in VS mode. To favour VS growth, the catalyst droplet is totally consumed and the V/III ratio is set to a large value (*e.g.* V/III = 10 in our experiments). The shell growth is thus limited by group III species. The shell growth rate (in nm s<sup>-1</sup>) is given by

$$v_s = \frac{v_{2D}}{\pi} (\tan \alpha + \delta). \quad (5.23)$$

Here,  $v_{2D}$  is a planar growth rate,  $\alpha = 32^\circ$  is the incidence angle of the Ga source cell (see Chapter 2). The additional contribution from the species re-emitted from the substrate is taken into account by the term  $\delta$ , which is  $\delta = \frac{\pi}{2}$  for Lambertian re-emission and  $\delta = \tan \alpha$  for specular re-emission (see Chapter 3). The factor  $\pi$  in Eq.(5.23) accounts for the circular section of the NW and for the sample rotation, since the NW sidewalls are exposed to the flux only intermittently.

The substrate temperature during droplet consumption and shell growth has a significant influence on NW morphology and composition. It is known that a higher substrate temperature improves the shell morphology, giving smoother sidewall facets, and that it also prevents the parasitic material deposition on the substrate [224]. However, we have found several drawbacks of a high temperature shell growth in the case of GaAs/GaP core/shell structures. The GaP shell grown around the GaAs core after the droplet consumption by a P flux at substrate temperature of 600°C (Figure 5.11(a, b)) exhibits a degraded morphology. As seen from the EDX map (Figure 5.11(b)), the GaP deposition results in Ga(P, As) alloy domains on the sidewalls. Thus no uniform shell is formed. On the contrary, if the substrate temperature is reduced to 500°C before droplet consumption and shell growth, the NW exhibits a uniform shell with a sharp GaAs/GaP interface (Figure 5.11(c, d)).

Moreover, during shell growth at a substrate temperature of 600°C, the catalyst droplet precedently consumed can be re-created even at a V/III ratio of 10. Panel (e) in Figure 5.11 shows a TEM image of such a NW. The presence of the droplet renders the VS shell growth very inefficient, since most of the Ga material is consumed by axial VLS growth. Decreasing the substrate temperature to 500°C allows one to avoid the

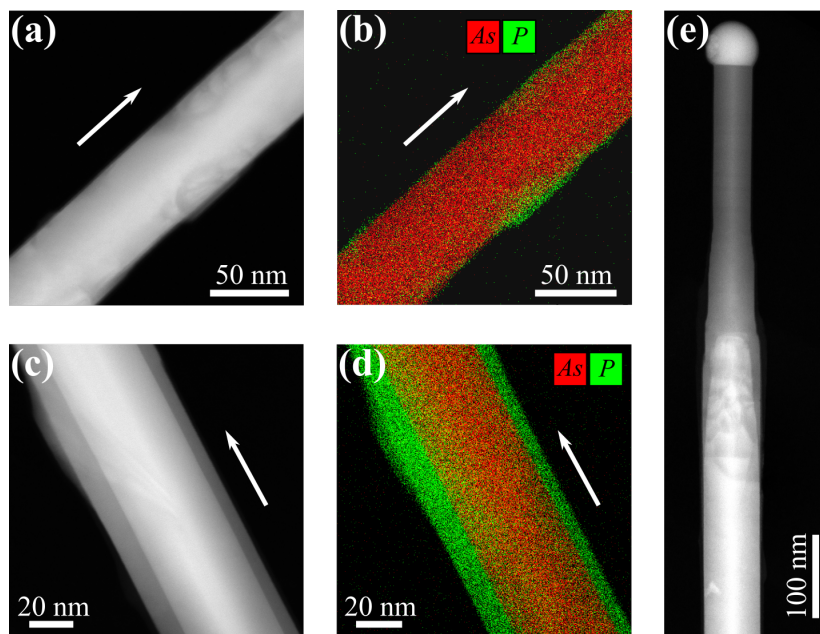


Figure 5.11: Effect of substrate temperature on the shell formation in GaAs/GaP core/shell NWs. (a) HAADF TEM image of a NW, where the catalyst droplet has been consumed by P at a substrate temperature of 600°C. The GaP shell was grown during 1 min 30 s. (b) EDX map of the GaAs/GaP NW imaged in (a), showing the formation of GaP domains partially intermixed with the GaAs core, during shell growth. (c) HAADF TEM image of a NW, where the catalyst droplet has been consumed by P at a substrate temperature of 500°C. The GaP shell was grown during 5 min. (d) EDX map of the GaAs/GaP NW imaged in (c), showing the formation of a uniform GaP shell. (e) HAADF TEM image of a GaAs/GaP NW with the droplet re-created during shell growth. In the HAADF TEM images, the GaAs core appears bright, the GaP shell darker. The arrows show the [111] NW growth direction.

droplet recreation and thus favours the VS shell growth mode.

#### 5.6.4 Summary of the conditions of GaAs/GaP core/shell nanowire growth

The growth of GaAs/GaP core/shell structures was performed in our MBE system (see Chapter 2) on both non-patterned and patterned Si(111) substrates. The details of the preparation of both types of substrates can be found in Sections 2.3.1 and 2.3.2 of Chapter 2.

The substrate was first exposed to a Ga flux. For the non-patterned substrates, the Ga deposition time was 8 s, which gives an average atom pre-deposition density of 19 at/nm<sup>2</sup>. For the patterned substrate, the pre-deposition step lasted 120 s at the same Ga flux, in order to fill the holes of the pattern with Ga. Then, the As shutter was opened for 10 min to grow the GaAs NW core by VLS. Prior to GaP shell

formation, the catalyst droplet was totally consumed by providing only phosphorous. The consumption of the droplet leading to shell formation allows us to form a core with a flat top. The shell growth duration was varied in order to obtain a different shell thickness in each experiment. The growth was terminated by closing all shutters and valves abruptly, and turning off the oven for rapid cooling.

In all the growth steps, the Ga flux was kept equivalent 2D growth rate of  $0.11 \text{ nm s}^{-1}$ , as measured by RHEED on GaAs(100). In order to vary the GaAs core radius, the  $\text{As}_4$  flux was adjusted to obtain V/III flux ratios from 2.1 for thick cores to 7.15 for the thinnest ones. For the shell formation, the  $\text{P}_2$  fluxes were set to a V/III atomic flux ratio of 10 in all the samples. The substrate temperature was fixed at  $600^\circ\text{C}$  during the pre-deposition step and the formation of the core, and decreased to  $500^\circ\text{C}$  for the crystallization of the catalyst droplet and shell formation.

## 5.7 Observation of dislocations in core/shell nanowires

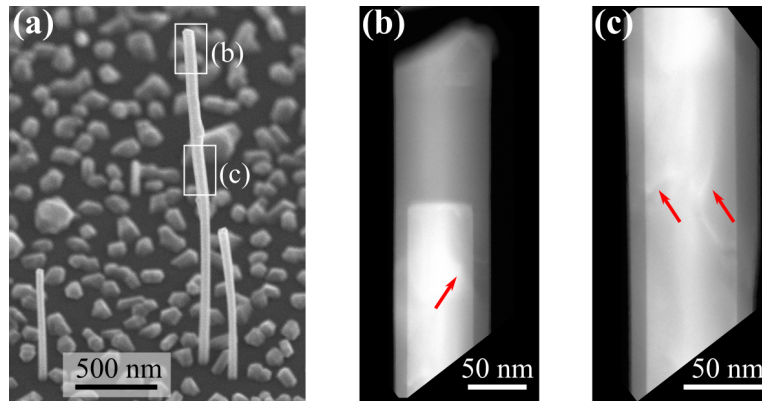


Figure 5.12: GaAs/GaP core/shell NWs grown on a Si substrate. (a) SEM overview of the NWs on the substrate. The GaAs/GaP NWs are slightly distorted because of the stress created by the mismatched GaP shell. The parasitic growth of GaP on the substrate occurs because of low-temperature shell growth. (b-c) HAADF TEM images of the areas indicated by the same letters in (a), showing the formation of a GaP shell along the NW. The dislocations appear brighter; some of them are shown by red arrows.

The growth sequence described in the previous section yields NWs with a length of  $2 - 3 \mu\text{m}$  (Figure 5.12(a)). As discussed in Section 5.6, across each sample we observe a variation of NW core radius, albeit with a uniform shell thickness for all NWs. The relatively low substrate temperature during shell growth results in a modest parasitic deposition of GaP on the substrate (Figure 5.12(a)). The total NW length can vary significantly in a sample, without much effect on the final core/shell lateral

dimensions. The presence of shorter NWs could result from delayed nucleation during the axial growth step. Since the growth occurs on a non-patterned Si substrate with a thin native  $\text{SiO}_x$  layer, nothing can prohibit new NWs to nucleate at any time during growth. Such NWs will be shorter due to the reduced effective growth time.

After SEM observation, some NWs were transferred to a copper grid to be characterised by HAADF TEM (Figure 5.12(b,c)). The images reveal NWs with a core with flat top and radius of 27 nm, and a shell thickness of 12 nm. We also observe the formation of dislocations (shown by red arrows) .

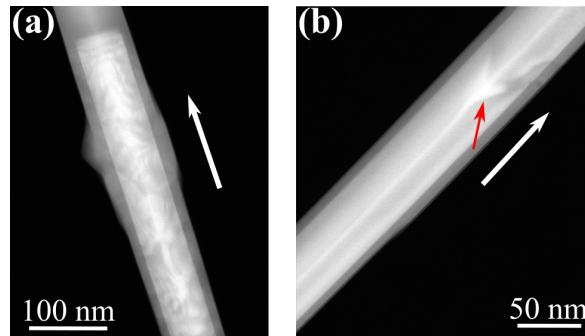


Figure 5.13: Complex (a) and isolated (b) dislocations formed in a core/shell GaAs/GaP NW. Red arrow shows a dislocation.

The real dislocations forming in the core/shell NWs appear more complex than the straight and loop defects considered in our model (see Section 5.3). Figure 5.13(a) shows the example of a GaAs/GaP NW with a core radius of 29 nm and shell thickness of 16 nm. In some NWs we observe an isolated dislocation (Figure 5.13(b)). But even in this case, the dislocation is not simply a loop or a straight line. However, it might be the first dislocation introduced at the beginning of plastic relaxation.

In order to locate the dislocation cores and to determine their Burgers vectors  $\mathbf{b}$ , the NWs were observed using the weak-beam (WB) technique. In WB imaging, the specimen is tilted so that most of the lattice planes, except those very close to the dislocation core, are rotated away from the Bragg condition. Thus, the peaks of the contrast give precisely the position of the dislocation. Forming images successively using three different diffraction vectors  $\mathbf{g}$  allows one to determine the Burgers vector  $\mathbf{b}$  of a particular dislocation [225].

Figure 5.14(a) shows the HAADF TEM image of a GaAs/GaP core/shell NW with dislocations, taken along a  $[1\bar{1}0]$  zone axis. To image the dislocations in this NW, we use the WB technique with  $\mathbf{g} = 220$  and  $\mathbf{g} = 004$ . The contrast peaks related to dislocations are visible with  $\mathbf{g} = 004$  (some of them are indicated by red arrows in Figure 5.14(c)), but disappear in the image taken with  $\mathbf{g} = 220$  (Figure 5.14(b)).

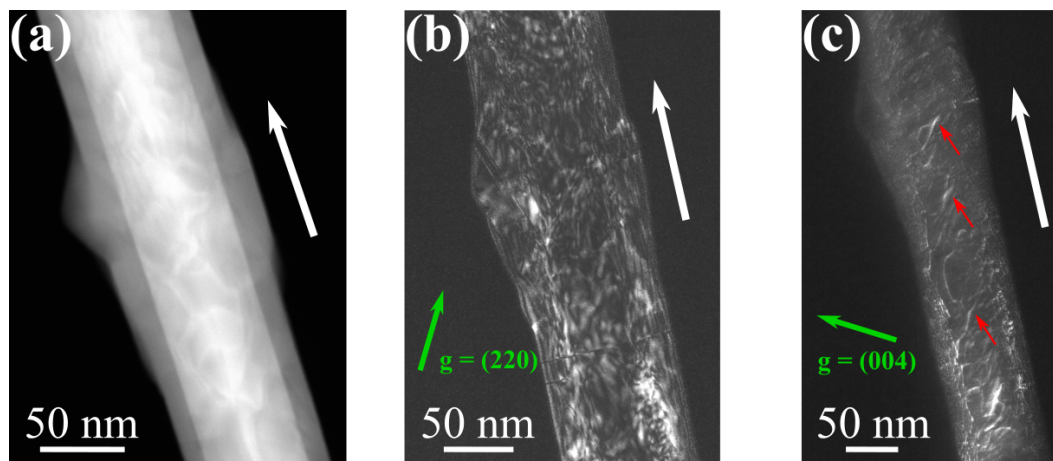


Figure 5.14: Dislocations in a GaAs/GaP core/shell NW. (a) HAADF TEM image of the NW taken along the  $[1\bar{1}0]$  zone axis. (b,c) WB images of the same NW taken with  $g = 220$  and  $g = 004$ . The small red arrows indicate the  $60^\circ$  dislocations visible with  $g = 004$ , but not with  $g = 220$ . The large white arrows show the  $[111]$  NW growth direction.

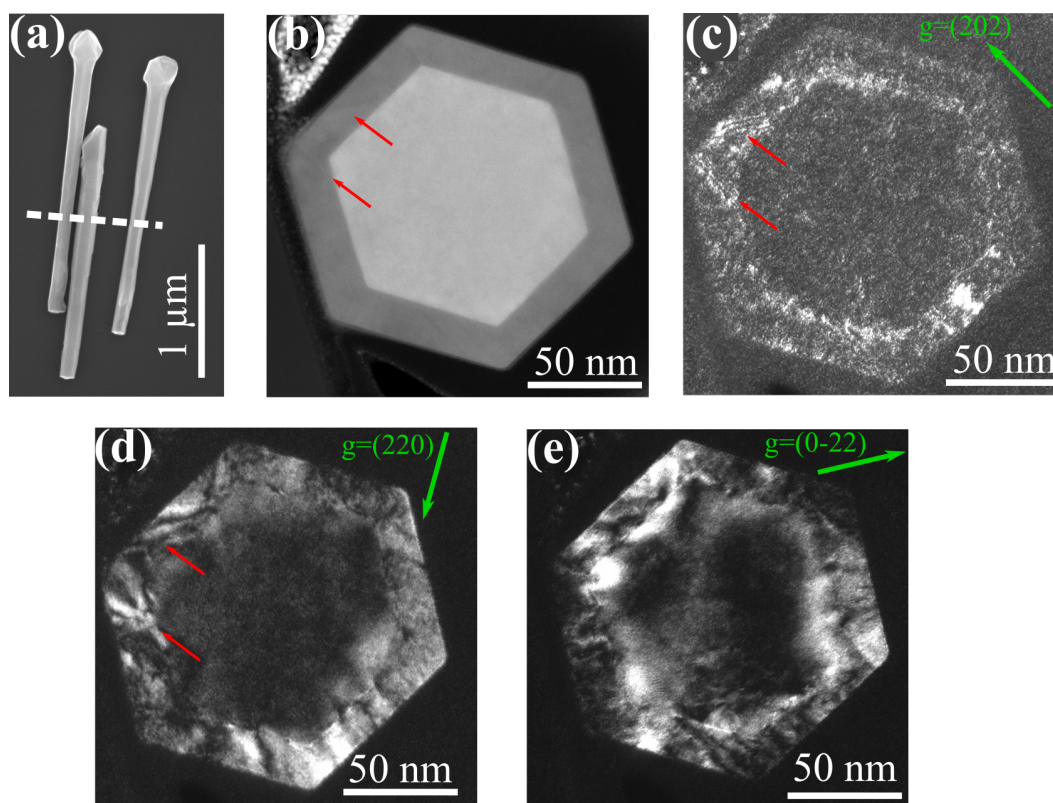


Figure 5.15: TEM Cross-section study of GaAs/GaP core/shell NWs. (a) General SEM image of NWs transferred to a Si carrying wafer. The white dashed line indicates the FIB cut direction. (b) HAADF cross-section TEM images of a GaAs/GaP NW segment taken along the  $[111]$  zone axis. (c-e) WB cross-section images taken with  $g = 202$  (c),  $g = 220$  (d) and  $g = 022$  (e). The red arrows indicate some dislocations.

According to the extinction criterion [225], we found the Burgers vector to lie along a  $\langle 011 \rangle$  direction, which corresponds to a  $60^\circ$  dislocation [193, 194]. These Burgers vectors are the same as those of the inclined loops observed in Ge/Si core/shell NWs by Dayeh *et al.* [202].

Dislocations with the same Burgers vectors are visible in cross-section geometry using WB TEM imaging. To this end, prior to the TEM observation, the NWs were transferred to a silicon wafer and covered with carbon. A thin slice, perpendicular to the NW axis (Figure 5.15(a)) was then cut by focused ion beam (FIB) in our dedicated dual beam microscope FEI ThermoFisher SCIOS. The contrast peaks corresponding to dislocations are visible in the images taken with  $\mathbf{g} = 202$  and  $\mathbf{g} = 220$  (Figure 5.15(c, d), respectively), but disappear in the image taken with  $\mathbf{g} = 0\bar{2}2$  (Figure 5.15(e)). This again indicates dislocations with Burgers vectors along  $\langle 011 \rangle$ .

## 5.8 Comparison of the calculated and experimental geometrical limits for plastic relaxation

As shown in the previous section, the real dislocations in core/shell NWs are quite complex. We did not observe any dislocation which would correspond to a single loop or straight line, as used to compute the geometrical limits for the introduction of a first dislocation in Section 5.5. The comparison is thus difficult. Nevertheless, we performed a comprehensive study of GaAs/GaP core/shell NWs (misfit 3.6 %) with various combinations of core radius and shell thickness. Blue squares and red diamond data points in Figure 5.16(a) correspond to NWs without and with dislocations, respectively. The triangles show the NWs where isolated dislocations could be observed.

Clearly, the  $(R_c, H)$  plane can be divided into 2 domains. The top right area gives the sets of core/shell dimensions at which dislocations are formed, and the bottom left area the dimensions at which defect-free growth is possible. In our experiments, we managed to grow a coherent GaP shell with thickness of 40 nm in NWs with a 11 nm core (Figure 5.16(b)). The green dashed curve outlines the boundary between these domains and thus gives the experimental critical shell thickness  $h_{crit}^{exp}$  above which a dislocation will be formed, as a function of core radius. As expected,  $h_{crit}^{exp}$  decreases with the core radius  $R_c$  increase. This critical thickness is precisely defined by the experimental points in the region  $R_c = 20 - 30$  nm but allows us to estimate only roughly the critical radius for the growth of a dislocation-free shell of arbitrary thickness, namely  $r_\infty^{exp} \approx 15$  nm.

To compare the experimental and calculated limits for dislocation introduction, we

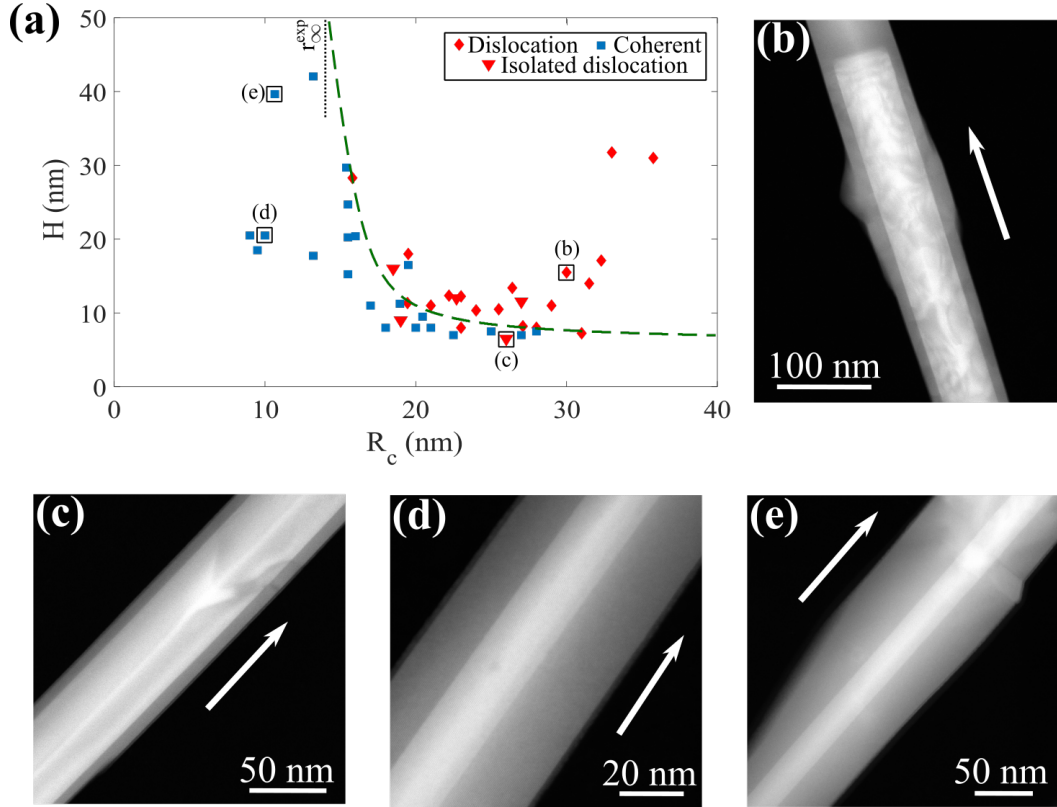


Figure 5.16: Experimental geometrical limits for GaAs/GaP core/shell defect-free NW growth. (a) Plot of the core/shell dimensions for dislocation-free NWs (blue squares) and NWs with dislocations (red diamonds). The triangle symbols correspond to the NWs, where isolated dislocations are observed. The dashed curve gives the experimental critical shell thickness  $h_{crit}^{exp}$  for the introduction of dislocations (b-d) HAADF TEM images of GaAs/GaP core/shell NWs with dimensions indicated by the same letters in (a), showing the NW with (b-c) and without (d-e) dislocation formed. The arrows show the  $[111]$  NW growth direction.

plot our experimental curve together with theoretical estimates of core/shell geometrical limits for the formation of loop dislocations and straight off-axis dislocations (black and blue curves in Figure 5.17). The full curves show for the limits within our assumption (i) of elastic isotropy, and the dash-dotted curve that for a transverse isotropy about a  $[111]$  axis (assumption (ii))

Our theoretical curves follow the same trends as the experimental one. But given the different type of dislocations observed experimentally and used in calculations, there is no strict quantitative agreement. Our experiments clearly show that the NWs with thin cores can be grown without dislocations for shells thicker than predicted. With the core thickness increasing, the maximal shell thickness allowing the dislocation-free growth decreases and approaches that estimated theoretically. Our estimates for  $h_{crit}$  approaches asymptotically the critical values of the defect-free planar growth of

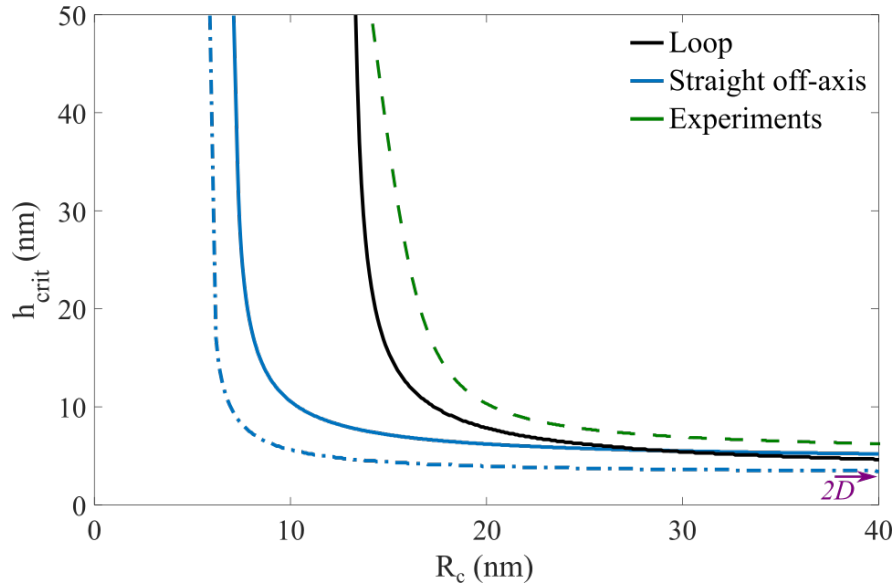


Figure 5.17: Experimental (green curve, from Figure 5.16(a)) and calculated (black curve for dislocation loops and blue curves for straight off-axis dislocations) limits for dislocation-free growth. For our theoretical estimations, the solid curves correspond to elastically isotropic NWs, the dash-dotted curve to transverse isotropy about the [111] growth axis. Magenta arrow shows the critical 2D GaP film thickness for dislocation-free growth [223, 226].

GaP on GaAs substrate, estimated theoretically ( $h_{crit} = 3.6$  nm) and experimentally ( $h_{crit} = 1.6$  nm) [223, 226].

## 5.9 Summary and conclusions

To summarize, in this Chapter we presented a joint theoretical and experimental study of the geometric limits for the formation of dislocations in core/shell NWs. We considered a single loop and a straight off-axis dislocation as candidates to relieve the strain. The geometrical limits for the introduction of a first dislocation were computed separately for each type of defect by comparison of the total energies of coherently strained NWs and NWs with one dislocation. The model was applied to GaAs/GaP core/shell NWs under two assumptions: elastically isotropic materials for the core and the shell, and transverse elastic isotropy around a [111] axis. The latter assumption gives smaller values of the core radius and shell thickness for the introduction of the first dislocation. Improving on the previously published results positioning a straight dislocation on the central axis of the NW, our calculations for a straight dislocation at the interface still give more stringent geometrical limits than for loop dislocations, for thin core radii. For the large core radii, the limits for both types of dislocations

converge to a value close to the critical thickness of a GaP film on the GaAs substrate.

Finally, we compared our calculations with experiments on GaAs/GaP core/shell NWs with various core radii and shell thicknesses. To avoid possible imperfections of the core/shell structures, such as tapered cores or core/shell interface degradation, we optimized the growth conditions, in order to obtain a sharp interface between the core and a shell of uniform thickness. The TEM analysis of our NWs reveals complex networks of dislocations. For the NWs with the thinnest cores, the calculations gives much smaller critical shell thicknesses for dislocation-free growth than observed in our experiments. For the NWs with core radii around 10 nm, we achieved the growth of a defect-free shell with a thickness of 40 nm. These results show that it is possible to grow much thicker defect-free shells than predicted by theory, which should be very useful for future experimental work and device applications.

# Chapter 6

## General conclusion and perspectives

In this final Chapter, we summarize the main results of the present study and give perspectives for future work. The first part of the study was devoted to understanding the dynamics of the droplet consumption. To this end, we performed experiments on the partial consumption of a Ga droplet seated on the top of a VLS-grown GaP NW. The NWs were exposed to a phosphorous flux for various times, which allowed us to investigate the evolution of the droplet geometry, namely contact angle, droplet radius and droplet base radius, during the consumption. To describe the dynamics of these parameters, we then developed analytical calculations for four possible channels of droplet consumption. To do so, we consider an axisymmetric cylindrical NW isolated on the substrate, which is subjected to three pathways of delivery of phosphorous atoms to the droplet. These are direct impingement on the droplet, re-emission from the substrate and surface diffusion of phosphorous adatoms on the NW sidewalls. For this last pathway, we account for adatoms reaching the sidewalls by direct impingement and by re-emission from the substrate. In addition, we consider the reduction of the droplet volume by back diffusion of Ga atoms from the droplet towards the NW base; this constitutes our fourth consumption channel.

When performing the calculation of the re-emitted currents, we test two extreme hypotheses for the angular distribution of re-emission. Namely, we compute the currents in case of specular re-emission, which corresponds to a purely mechanical interaction of the phosphorous dimers with the substrate, and Lambertian cosine distribution, which is expected for molecules having reached equilibrium with the substrate. For these currents we derived analytical formulae, which describe the current variations with change of droplet geometry and take into account the possible shadowing of the re-emission by the droplet itself and by the NW stem. To determine the unknown parameters of our model, namely the phosphorous diffusion length and a prefactor in the expression

for the gallium back diffusion rate, we devised complementary experiments. In these experiments, we inserted the Ga(As,P) marker layers during the NW growth. The presence of the markers allowed us to distinguish how the gallium from the droplet which forms solid GaAs distributes between the GaP top segment and a thin GaP overgrowth. We found that, in our experimental conditions, about 55 % of the droplet volume is consumed by the phosphorous currents (direct impingement, re-emission and diffusion) and about 44 % of the gallium left the droplet via back diffusion. From this we extracted the model parameters. In particular, we found that, to fit our experiments, the phosphorous diffusion length should be 80 nm and 400 nm for Lambertian and specular re-emission, respectively. The larger value for the specular re-emission is due to the fact that, for a given droplet contact angle, the re-emitted current is smaller than in case of Lambertian re-emission.

We demonstrated that our experimental results can only be satisfied if all four droplet consumptions channels are taken into account. The droplet consumption process can be divided into three stages. During stage I, the droplet base radius remains equal to the NW radius and the volume of the droplet decreases by a decrease of the contact angle. Once the contact angle reaches about  $\pi/2$ , the NW starts to taper, developing tilted facets, but the droplet remains pinned to the edge between tilted and horizontal top facets. During this stage II, the base radius of the droplet and its contact angle both vary. After the droplet contact angle reaches the Young's angle relative to the NW top facet, it remains fixed to this value but the droplet depins (stage III). The droplet volume then changes via a shrinking of the base radius until the droplet vanishes. Overall, with either Lambertian or specular re-emission, the diffusion of both species accounts for around two thirds of the total droplet consumption (63% and 76% of its initial volume, respectively). Ga back diffusion contributes significantly, consuming nearly half of the initial droplet volume.

Our model allows one to predict the time needed to reduce the droplet to a given geometry, under a given group V flux and starting from a known geometry. To have an accurate control of the droplet geometry, it is crucial to understand how the currents, affecting the droplet depletion can be controlled. Contrary to the phosphorous direct, re-emitted and diffusion currents, which depend directly on the external phosphorous flux, the dependence of gallium back diffusion on the growth conditions is not clear. An additional study would be necessary to clarify the temperature dependence of the back diffusion current. One would also need to find out if the presence of the phosphorous species promotes somehow gallium back diffusion, or if this process can take place independently. If this was the case, a droplet could be consumed completely or partially

by Ga back diffusion only, and thus without the formation of the axial top segment. This would be useful for abrupt changes of the NW crystal structure, which is known to depend on the droplet contact angle. On the other hand, suppressing completely the back diffusion would allow one to avoid the formation of the unintentional shell. This could be applied to the growth of complex NW structures combining axial and radial heterojunctions, in particular if one does not wish to grow a shell of the same material as the top segment.

As for the angular distribution of the re-emission of the group V species, our model cannot assert which is the actual scheme. Since the specular re-emission current depends on the source inclination angle whereas the Lambertian current does not, to clarify this point, it would be interesting to perform experiments at different source inclinations. In addition, this distribution could be different for the group III beam, which consists of atoms, and the group V beam, consisting of molecules.

Once we were able to reduce deterministically the droplet size, we studied how to reduce the local diameter of the NW in a controllable fashion. To this end, after the NW stem growth, we consume partially the droplet under phosphorous only. The duration of consumption was adjusted using our model so as to obtain a given droplet base radius. We then continue the growth in presence of both gallium and phosphorous fluxes at a high V/III flux ratio. This procedure results in a thin GaP segment on top of the thick stem. Although the droplet contact angle decreased to the Young's angle value of  $65^\circ$  during the consumption, after 5 min of growth of the thin stem it recovered its value of  $136^\circ \pm 1^\circ$ , the same as usually observed during the growth at lower V/III ratios. The radius of the thin segment  $R_f^{exp}$  is about of the same as the droplet base radius  $R_b^{est}$  after the consumption, albeit  $R_f^{exp}$  is expected to be smaller than  $R_b^{est}$  due to the increase of the contact angle of the droplet at constant volume. This larger radius can originate from the radial growth, which the thin segment exhibits. In addition, with the increase of the length of the thin segment, the gallium diffusion current to the droplet increases. This leads to the increase of the droplet volume.

After 5 min of growth of the thin segment, the interface, defined as the region over which the NW diameter changes at the base of the thin segment, is sharp, but the top part of the stem is tapered. Growth for 10 min however leads to further increase of the thin segment radius due to radial growth, which becomes significant at the thin segment/thick stem interface. The transition from the stem to the top segment now extends over a certain length. This effect is related to the accumulation of Ga on the inclined facets of the interface, which enhances radial growth. Nevertheless, the top part of the thin segment preserves a uniform radius over several hundreds of

nanometers.

If the apical droplet is exposed to an excess of gallium (*i.e.* a V/III ratio below one), it will inflate. But during the inflation the droplet can slide down on the sidewalls, so the inflation should be performed carefully in order to maintain the droplet on the top. To study the droplet inflation, we exposed the already grown GaP NWs to gallium and phosphorous fluxes at V/III ratios of 0.5 and 0.25 for various times. We found that, at variance with theoretical predictions, the droplet contact angle does not increase forever before sliding, but stabilize to a certain value  $\beta_s$ , which depends on the V/III ratio. Specifically,  $\beta_s$  is  $147^\circ \pm 2^\circ$  with a V/III ratio of 0.5 and increases to  $158^\circ \pm 1^\circ$  at a V/III ratio of 0.25. This stabilization of the contact angle could originate from the equilibration of the currents entering the droplet. An additional study is needed to find out if the group III back diffusion also contributes.

If the fluxes are restored to the values used during stem growth, the top segment radius  $R_e$  starts to increase and then stabilizes, whereas the droplet contact angle remains the same. By performing the growth of the top thick segment on stems with various radii  $R_f$ , we found that  $R_e$  is not independent on  $R_f$ . For the smaller stem radii  $R_f$ , the NW can double or even triple its radius at the level of the thick segment, while for NWs with a thick stem, the enlargement ratio  $R_e/R_f$  is limited to 1.5. In addition, the NWs with a narrow stem display a sharp stem/thick segment transition, while in those with a thicker stem the transition extends over a certain length. The difference in the radii of the top segment can be attributed to the differences of the gallium diffusion length on the differently oriented NW facets. To fully understand the origins of this effect, a further study should investigate the diffusion of gallium adatoms on the inclined sidewalls and the possibility of their diffusion over the stem/thick segment transition, especially when it is sharp.

We demonstrated that it is possible to realize sharp changes of the diameter in a NW of a single material in both directions, from thin to thick and the reverse. These operations can be performed blindly in a standard MBE equipment. The combination of these changes in a single NW would lead to diameter-modulated structures. Although this operation could look rather straightforward, some issues may arise. Supplementary studies should be devoted to the investigation of the mechanisms of radial growth at the stem/top segment transition and to the possibility to minimise or completely avoid it. In addition, since the growth of the top segments include the variation of the droplet contact angle, the NW could exhibit a mixed crystal structure, especially in the transition region. A detailed study of this point might open the way to a controlled combined change of crystal structure and NW radius.

Whatever the morphology, composition and crystal structure of a NW, in order to be used for device fabrication, it will often need to be wrapped with a shell, thereby forming a core/shell structure. Such a shell, sometimes mismatched, should be grown without dislocation, the presence of which will degrade the electronic and optical properties of the structure. It is thus essential to determine the core/shell dimensions at which the formation of a defect-free shell becomes likely. We first studied this point by modelling the strain state of the core/shell NW with and without dislocation. By comparing the total energies of a NW with a coherent interface and with dislocations, we computed the geometrical limits for core radius and shell thickness, above which the formation of a first dislocation is energetically favourable. We performed these calculations for a loop dislocation in the framework of isotropic elasticity and for a straight off-axis dislocation within the two assumptions of an elastically isotropic NW and of a NW with transverse elastic isotropy about the [111] growth axis.

To compare our calculations with experimental limits for dislocation-free growth, we performed a comprehensive study of GaAs/GaP core/shell NWs, varying both core radius and shell thickness. The dislocations observed are much more complex than those considered in our model. Our theoretical estimates are thus not expected to give a full quantitative agreement, but they follow the same trends as the experimental results. For NWs with the thinnest cores, the calculations gives much smaller critical values for dislocation-free growth, than observed in our experiments. For NWs with core radius around 10 nm, we achieved the growth of defect-free shells with a thickness of 40 nm.

The geometrical limits, obtained either experimentally or by modelling, are for NWs with uniform core radii and shell thicknesses. More complex structures, such as the diameter-modulated core/shell NWs considered above, may exhibit quite different critical dimensions for defect-free growth. This would also require further studies.

The results presented in this Thesis open the way to the realization of complex structures in NWs, which might reveal useful for basic physics and applications.



# Résumé en français

Les nanofils semi-conducteurs III-V sont étudiés depuis plusieurs décennies. Bien qu'ils ne soient pas encore largement mis en œuvre dans des produits commerciaux, ils présentent néanmoins des propriétés très intéressantes pour diverses applications [6, 13, 14, 19]. Les nanofils offrent plusieurs avantages clés, tels qu'une excellente qualité cristalline et la possibilité d'élaborer une large gamme de structures. Celles-ci incluent différentes combinaisons de structures 1D et 0D, dont certaines sont spécifiques aux nanofils, telles les hétérostructures de phase cristalline et les points quantiques [25–27], les homo- et hétérojonctions axiales et radiales avec diverses compositions ou niveaux de dopage [6, 7, 16], les super-réseaux compositionnels et morphologiques (*i.e.* avec changements périodiques des dimensions du nanofil le long de l'axe de croissance) [11, 13]. Contrairement à la plupart des semi-conducteurs III-V sous forme massive ou en couche mince, les nanofils III-V peuvent être intégrés sur un substrat de silicium sans nuire à la qualité du cristal, en raison de leur faible surface de base, ce qui facilite l'accommodation de la contrainte liée à la différence de paramètre de maille. De plus, le progrès récent des techniques de croissance de nanofils permet de fabriquer de grands ensembles des nanofils identiques avec la même composition, structure et morphologie sur un même substrat, avec un haut niveau de reproductibilité. Cependant, le potentiel des dispositifs à base de nanofils ne se concrétisera pleinement que si on parvient à contrôler très précisément leur morphologie, phase cristalline, dopage et profils de composition, qui sont souvent fixés au stade même de l'élaboration. Bien que diverses techniques soient couramment utilisées pour fabriquer des nanofils de composition et de structures diverses, de nombreux mécanismes contrôlant leur formation et leurs propriétés restent à étudier et à bien comprendre.

Cette étude porte sur les nanofils auto-catalysés de GaAs et GaP fabriqués par épitaxie par jet moléculaire sur un substrat de Si, en mode de croissance vapeur-liquide-solide. Nous étudions, sur les plans expérimental et théorique, diverses questions relatives au contrôle précis du diamètre d'un nanofil, notamment sa modification déterministe durant la croissance, et aux structures cœur-coquille à base de matériaux de paramètres de maille différents pour, afin d'éviter la formation de dislocations in-

terfaciales.

## Dynamique de la goutte de catalyseur

Dans ces nanofils, le volume de la goutte de gallium qui sert de catalyseur peut être contrôlé en jouant sur les apports respectifs d'éléments III (Ga) et V (P ou As). La goutte peut notamment être consommée sous un excès d'élément V, cette consommation produisant une section du cristal III-V correspondant. Le contrôle de la géométrie de la goutte pendant sa consommation est crucial pour ouvrir la voie au contrôle local de la géométrie et de la structure cristalline locale du nanofil. Ce contrôle est toutefois délicat car l'observation de ces processus en temps réel est impossible dans les systèmes d'épitaxie standards. En outre, il existe toujours un risque de ne pas réduire suffisamment le diamètre des gouttes pour pouvoir ensuite faire croître une section de nanofil de diamètre quantique ou, au contraire, de le consommer entièrement. Dans le but de maîtriser précisément ce processus, nous avons développé un modèle qui décrit l'évolution d'une goutte de catalyseur au sommet d'un nanofil III-V auto-catalysé exposé à un flux d'élément V.

Notre modèle est basé sur les expériences de consommation partielle de la goutte. Après la croissance auto-catalysée de nanofils de GaP organisés en réseaux de différentes périodes sur substrat de  $\text{SiO}_x/\text{Si}$  (111), nous avons exposé l'échantillon à un flux de phosphore uniquement (le flux de Ga est arrêté). Afin d'étudier la progression de la consommation de la goutte de catalyseur, nous avons fait varier la durée d'exposition de 1 minute à 3 minutes.

Pour décrire la dynamique de la géométrie de la goutte lors de sa cristallisation, nous avons développé des calculs prenant en compte quatre canaux possibles de consommation de la goutte sous exposition à la seule espèce du groupe V (Figure F1). Trois canaux correspondent à différents courants de phosphore vers la gouttelette, qui consomment le gallium en formant du GaP solide. Les atomes de phosphore peuvent être délivrés à la goutte par impact direct (i), ou après ré-émission depuis le substrat (ii), ou par diffusion sur les flancs du nanofil considéré d'adatoms déposés sur le substrat ou sur les flancs (iii). Cette troisième voie est généralement jugée inefficace pour les éléments du groupe V. En plus, le volume de la goutte peut diminuer en raison de la 'rétro-diffusion' des atomes de Ga le long des flancs des nanofils voisins vers la base du nanofil ; cela constitue notre quatrième canal (iv). Enfin, Ga et P peuvent quitter la goutte en raison de la désorption (v).

Afin de calculer les courants correspondant à ces différentes voies de consommation de la goutte, nous avons considéré un nanofil axisymétrique isolé sur un substrat infini.

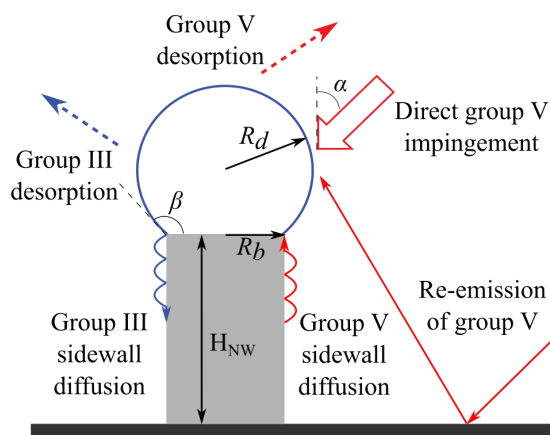


Figure F1: Schéma des courants de matériaux contribuant à la consommation d'une goutte située au sommet d'un nanofil III-V isolé. Ici,  $R_b = R_{NW}$ .

La goutte apicale est une calotte sphérique d'angle de contact  $\beta$ , de rayon  $R_d$  et de rayon de base  $R_b = R_d \sin \beta$  et le corps du nanofil est un cylindre circulaire droit de rayon  $R_{NW}$  et de hauteur  $H_{NW}$  (Figure F1). Tant que la goutte reste accrochée aux flancs du nanofil,  $R_b = R_{NW}$ . L'ensemble du système est exposé à un faisceau moléculaire de  $P_2$  (à l'angle d'incidence  $\alpha$ ), produisant un flux atomique de phosphore  $F_e$  par unité de surface de substrat. Tous les calculs ont été effectués de façon analytique et les formules explicites sont fournies.

Le courant direct  $I_{dir}$  a été calculé précédemment [123]. Il dépend de la géométrie de la goutte et de l'angle d'incidence  $\alpha$ .

Pour ce qui est du courant ré-émis  $I_r$ , nous avons testé deux hypothèses extrêmes de distribution angulaire de ré-émission, la distribution Lambertienne (en cosinus) et la réflexion spéculaire. Dans le cas lambertien, qui est attendu pour des molécules ayant atteint l'équilibre thermique avec le substrat, les espèces de phosphore sont ré-émises indépendamment de leur angle d'incidence, alors que dans le cas de la réflexion spéculaire, qui correspond à une interaction purement mécanique avec le substrat, elles sont évidemment ré-émises sous un angle égal à leur angle d'incidence  $\alpha$ .

Sur la Figure F2, les variations expérimentales dans le temps de divers paramètres géométriques de la goutte (symboles) sont comparées à différents calculs (lignes). L'angle de contact et le rayon de goutte mesurés diminuent plus rapidement que ceux calculés en n'incluant que l'impact direct (i) et la ré-émission (ii), qu'elle soit lambertienne ou spéculaire (traits en tirets-pointillés et en tirets, respectivement). Ces deux courants ne fournissent donc pas assez de phosphore pour consommer la goutte au rythme observé, et la quantité manquante est importante. On est ainsi conduit à prendre en compte les deux canaux supplémentaires (iii) et (iv) de consommation de la goutte de Ga précités.

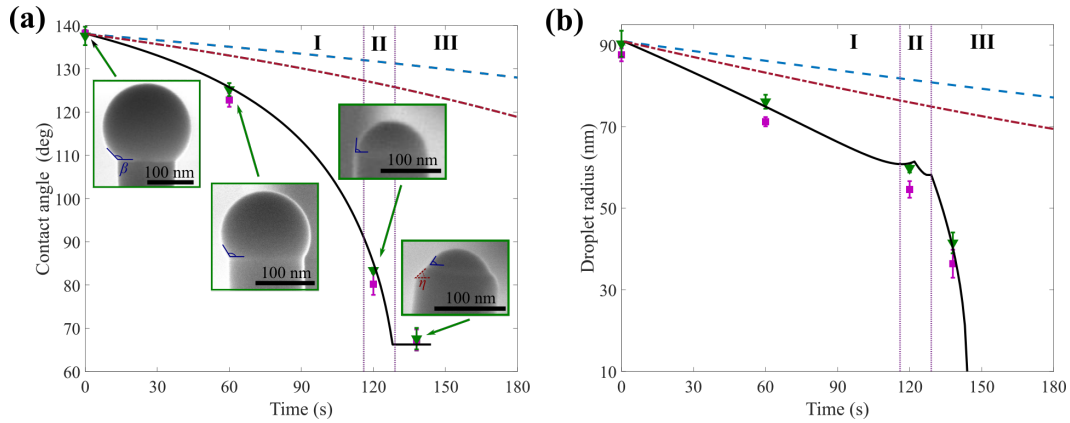


Figure F2: Variation de l'angle de contact de la goutte (a) et du rayon  $R_d$  (b) lors de la consommation. Les symboles donnent les valeurs expérimentales pour les périodes de  $1 \mu\text{m}$  (carrés) et  $5 \mu\text{m}$  (triangles), moyennées sur plusieurs nanofils. Les courbes montrent les résultats de calculs ne considérant que l'impact direct et la ré-émission [spéculaire (traits en tirets) ou lambertien (traits en tirets-pointillés)], ou avec diffusion du phosphore et du gallium en plus (traits pleine). Les encarts en (a) montrent les images SEM de la goutte apicale à chaque étape de la consommation.

Pour calculer le courant de diffusion de phosphore  $I_{dif}$  (iii), nous avons introduit une longueur de diffusion de surface  $\lambda_V$  et avons supposé que tous les atomes frappant les flancs du nanofil sur cette distance en dessous de la ligne de phase triple (TPL) sont transférés à la goutte. Les flancs collectent eux-mêmes les courants de phosphore direct et ré-émis par le substrat, et ce dernier est différent dans les cas de ré-émission lambertienne et de ré-émission spéculaire.

Enfin, nous avons considéré le courant  $I_{bd}$  de Ga quittant la goutte (iv). Pour calculer cette contribution, nous avons utilisé la théorie des états de transition développée pour la croissance des nanofils par Krogstrup *et al.* [99]. Le courant net d'atomes du groupe III est la différence des courants entrant et sortant de la goutte. Le courant entrant dans la goutte est proportionnel à la densité d'adatomes de Ga sur les flancs du nanofil, juste en dessous de la TPL, et dépend de façon exponentielle de leur potentiel chimique (par rapport à l'énergie de l'état de transition). Cependant, en raison de l'absence d'apport externe de Ga pendant la consommation des gouttes, la densité et donc le potentiel chimique devraient être faibles. On ne considère donc que la transition inverse liquide-adatome.

Finalement, nous avons trouvé que les courants de désorption de Ga et P (v) sont négligeables devant les quatre premiers courants, du moins aux températures auxquelles nous opérons.

L'évolution temporelle de la géométrie de la goutte a ensuite été calculé numériquement, en incluant les contributions (i) à (iv), qui dépendent de la géométrie instantanée de la

goutte (rayon de base et angle de contact). Notre modèle inclut deux paramètres libres, la longueur de diffusion du phosphore  $\lambda_V$  et un pré-facteur pour la rétro-diffusion de Ga. Pour estimer ces paramètres, nous avons conçu des expériences complémentaires. Dans ces expériences, nous avons inséré des couches marqueurs d'alliage Ga(As,P) à la fin de la croissance du nanofil. La présence des marqueurs nous a permis de distinguer comment, lors de la consommation qui suit, le gallium de la goutte qui forme du GaP solide se répartit entre un segment axial terminal et une fine coquille. Nous avons constaté (par des expériences de microscopie électronique en transmission) que, dans nos conditions expérimentales, environ 55 % du volume de la goutte est consommé par les courants de phosphore (impact direct, ré-émission et diffusion) et environ 44 % du gallium a quitté la goutte par rétro-diffusion. Ces mesures nous ont permis d'extraire les paramètres libres du modèle. En particulier, nous avons constaté que, pour reproduire nos expériences, la longueur de diffusion du phosphore devrait être de 80 nm et 400 nm pour les ré-émissions lambertienne et spéculaire, respectivement. La valeur plus élevée pour la ré-émission spéculaire est due au fait que, pour un angle de contact de goutte donné, le courant ré-émis est plus faible que dans le cas d'une ré-émission lambertienne.

Nous avons démontré que nos résultats expérimentaux ne peuvent être reproduits par le calcul que si les quatre canaux de consommation de la goutte sont pris en compte (traits pleines sur Figure F2). Le processus de consommation de la goutte peut être divisé en trois étapes. Lors de l'étape I, le rayon de la base de la goutte reste égal au rayon du nanofil et le volume de la goutte diminue par une diminution de son angle de contact. Une fois que l'angle de contact atteint environ  $\pi/2$ , le nanofil commence à rétrécir, en développant à son sommet des facettes inclinées, mais la goutte reste ancrée à l'arête au bord entre les facettes supérieures inclinées et horizontale. Au cours de cette étape II, le rayon de base de la goutte et son angle de contact varient tous deux. Une fois que l'angle de contact de la goutte a atteint l'angle de Young relatif à la facette supérieure du nanofil, il reste fixé à cette valeur mais la goutte se désancre de l'arête (stade III). Le volume de la goutte change alors via un rétrécissement du rayon de base jusqu'à ce que la goutte disparaisse. Globalement, qu'il s'agisse de ré-émission lambertienne ou spéculaire, la diffusion des deux espèces représente environ les deux tiers de la consommation totale de la goutte (63% et 76% de son volume initial, respectivement). La rétro-diffusion de Ga contribue de manière significative, en consommant près de la moitié du volume initial de la goutte.

## Vers des nanofils de diamètre modulé

Une fois que nous sommes parvenus, grâce à notre modèle, à réduire de manière déterministe la taille de la goutte apicale, nous avons étudié comment réduire localement le diamètre du nanofil. A cet effet, après la croissance du pied du nanofil, on consomme partiellement la goutte sous phosphore uniquement. La durée de consommation a été ajustée à l'aide de notre modèle de manière à obtenir un rayon de base de goutte donné. Nous avons ensuite poursuivi la croissance en présence de flux de gallium et de phosphore à un rapport de flux V/III élevé. Cette procédure produit un segment de GaP mince au-dessus du pied épais. Bien que l'angle de contact des gouttes ait diminué jusqu'à la valeur de l'angle de Young de  $65^\circ$  au cours de la consommation, après 5 minute de croissance de la section étroite, il a déjà retrouvé sa valeur de  $136^\circ \pm 1^\circ$ , celle même que l'on observe habituellement pendant la croissance standard à des rapports V/III inférieurs. Le rayon du segment mince  $R_f^{exp}$  est à peu près le même que le rayon de base de la goutte  $R_b^{est}$  calculé en fin de consommation (alors qu'on s'attendait à un  $R_f^{exp}$  inférieur à  $R_b^{est}$  en raison de l'augmentation de l'angle de contact de la goutte à la reprise de croissance. Ce rayon plus large que prévu peut provenir de la croissance radiale affectant sans doute le segment mince. De plus, avec l'augmentation de la longueur de ce segment mince, le courant de diffusion du gallium vers la goutte augmente, ce qui conduit à l'augmentation du volume de la goutte.

Après 5 minutes de croissance du segment mince, l'interface, définie comme la région sur laquelle le diamètre du nanofil change à la base du segment mince, est nette, mais la partie supérieure du pied est biseauté. La croissance pendant 10 minutes conduit cependant à une augmentation supplémentaire du rayon du segment mince en raison de la croissance radiale, qui devient significative à l'interface segment mince/pied. La transition entre pied et segment supérieur s'étend maintenant sur une longueur appréciable. Cet effet est lié à l'accumulation de Ga sur les facettes inclinées de l'interface, ce qui favorise la croissance radiale. Néanmoins, la partie supérieure du segment mince conserve un rayon uniforme sur plusieurs centaines de nanomètres.

Si la goutte apicale est exposée à un excès de gallium (rapport de flux V/III inférieur à un), elle gonflera. Mais pendant cette expansion, la goutte risque de glisser vers le bas sur les flancs du nanofil. L'apport supplémentaire de Ga doit donc être effectué avec précaution afin de maintenir la goutte au sommet du nanofil. Pour réaliser cette inflation des gouttelettes, nous avons exposé les nanofils de GaP à des flux de gallium et de phosphore dans des rapports V/III de 0,5 et 0,25 pendant des temps différents. Nous avons constaté que, contrairement aux prédictions théoriques, l'angle de contact des gouttes n'augmente pas indéfiniment, mais se stabilise à une certaine valeur  $\beta_s$ , qui

dépend du rapport V/III. Plus précisément,  $\beta_s$  vaut  $147^\circ \pm 2^\circ$  avec un rapport V/III de 0,5 et passe à  $158^\circ \pm 1^\circ$  pour un rapport V/III de 0,25. Cette stabilisation de l'angle de contact pourrait provenir de l'équilibrage des courants d'éléments III et V entrant dans la goutte.

Après être ainsi parvenus à faire croître un segment de nanofil ayant un rayon inférieur à celui du pied, nous avons tenté l'opération inverse, c'est-à-dire l'augmentation de diamètre. Si les flux de Ga et de P sont restaurés aux valeurs utilisées lors de la croissance du pied, le rayon du segment supérieur  $R_e$  commence à augmenter puis se stabilise, tandis que l'angle de contact de la goutte reste le même. En effectuant la croissance du segment épais supérieur sur des pieds de rayons différents  $R_f$ , nous avons trouvé que  $R_e$  n'est pas indépendant de  $R_f$ . Pour les plus petits rayons  $R_f$ , le nanofil peut doubler voire tripler son rayon au niveau du segment épais, tandis que pour les nanofils aux pieds épais, le rapport d'agrandissement  $R_e/R_f$  est limité à 1,5 (Figure F3(a)).

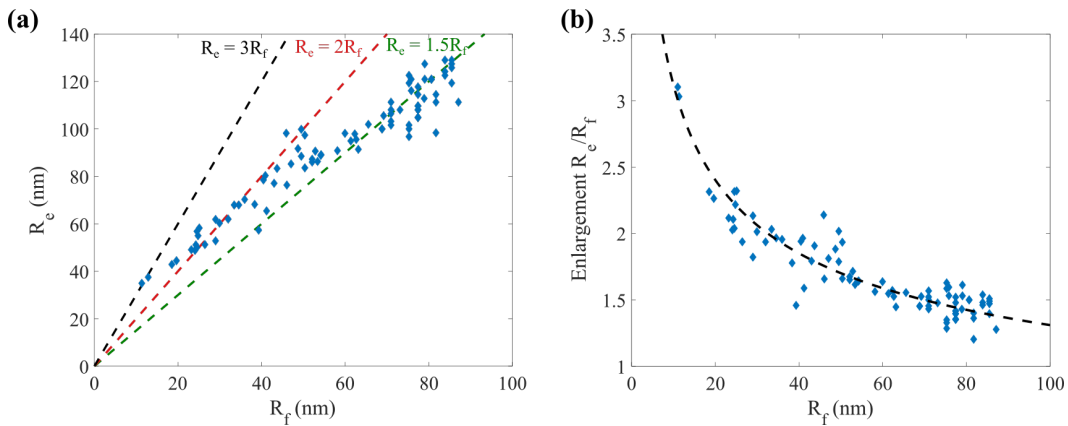


Figure F3: (a) Variation du rayon du segment épais supérieur  $R_e$  avec le rayon de pied  $R_f$ . Les traits en tirets donnent les exemples possibles d'une dépendance linéaire hypothétique de  $R_e$  sur  $R_f$ . (b) Variation du rapport d'agrandissement  $R_e/R_f$  avec le rayon  $R_f$ . Des symboles donnent les valeurs expérimentales. Le trait en tiret donne l'ajustement avec une loi de puissance  $R_f^{-K}$  avec  $K \approx 1/3$ .

En fait, le rapport d'agrandissement semble dépendre continûment du rayon du stem, avec une loi de puissance ( $\propto R_f^{-K}$  avec  $K \approx 1/3$ , Figure F3(b)). Nous notons cependant que les nanofils aux pieds les plus fins présentent un élargissement terminal modeste. De plus, les nanofils avec un pied étroit présentent une transition pied/segment épais abrupte, tandis que dans ceux ayant un pied plus épais, la transition s'étend sur une certaine longueur. La différence dans les rayons du segment supérieur peut être attribuée aux différences de longueur de diffusion du gallium sur des facettes orientées différemment.

## Limites géométriques pour une croissance sans défaut de nanofils cœur/coquille

Quelles que soient la morphologie, la composition et la structure cristalline d'un nanofil, afin d'être utilisé pour la fabrication de dispositifs, il devra souvent être enveloppé d'une coquille, formant ainsi une structure cœur/coquille. Une telle coquille, en général formée d'un matériau ayant un paramètre de maille différent de celui du cœur, doit croître sans dislocation, dont la présence dégradera les propriétés électroniques et optiques de la structure. Il est donc essentiel de déterminer les dimensions du cœur et de la coquille en dessous desquelles la formation d'une hétérostructure radial sans défaut cristallin étendu devient probable.

Nous avons d'abord modélisé l'état de contrainte du nanofil cœur/coquille avec et sans dislocation. En comparant les énergies totales d'un nanofil avec une interface cohérente et avec des dislocations, nous avons calculé les limites géométriques du rayon du cœur et de l'épaisseur de la coquille, au-dessus desquelles la formation d'une première dislocation est énergétiquement favorable. Nous avons effectué ces calculs pour une boucle de dislocation normale à l'axe du nanofil dans le cadre de l'élasticité isotrope, et pour une ligne de dislocation parallèle à l'axe mais excentrée dans les deux hypothèses d'un nanofil élastiquement isotrope et d'un nanofil avec une isotropie élastique transverse autour de l'axe de croissance [111].

Pour comparer nos calculs avec les limites expérimentales de la croissance de nanofils sans dislocation, nous avons effectué l'étude complète des nanofils cœur/coquille de GaAs/GaP, en variant à la fois le rayon du cœur  $R_c$  et l'épaisseur  $H$  de la coquille. Pour bien contrôler les dimensions de nanofils cœur/coquille, nous avons effectué l'optimisation des conditions de toutes les étapes de la croissance, dont la croissance des cœurs fins, la consommation de la goutte et la formation d'une coquille uniforme avec interface abrupte avec le cœur.

Les dislocations observées en microscopie électronique (les expériences ayant été réalisées par un collègue) sont beaucoup plus complexes que celles considérées dans notre modèle. Nos estimations théoriques ne devraient donc pas donner un accord quantitatif complet, mais elles suivent les mêmes tendances que les résultats expérimentaux (Figure F4(a)). Clairement, le plan  $(R_c, H)$  peut être divisé en deux domaines. La zone en haut à droite donne les couples de dimensions cœur/coquille auxquels les dislocations sont formées, et la zone en bas à gauche les dimensions auxquelles une croissance sans défaut est possible. La courbe en tirets verts dessine la limite entre ces domaines et donne ainsi l'épaisseur critique expérimentale de coquille  $h_{crit}^{exp}$  au-dessus de laquelle une dislocation se formera, en fonction du rayon du cœur.

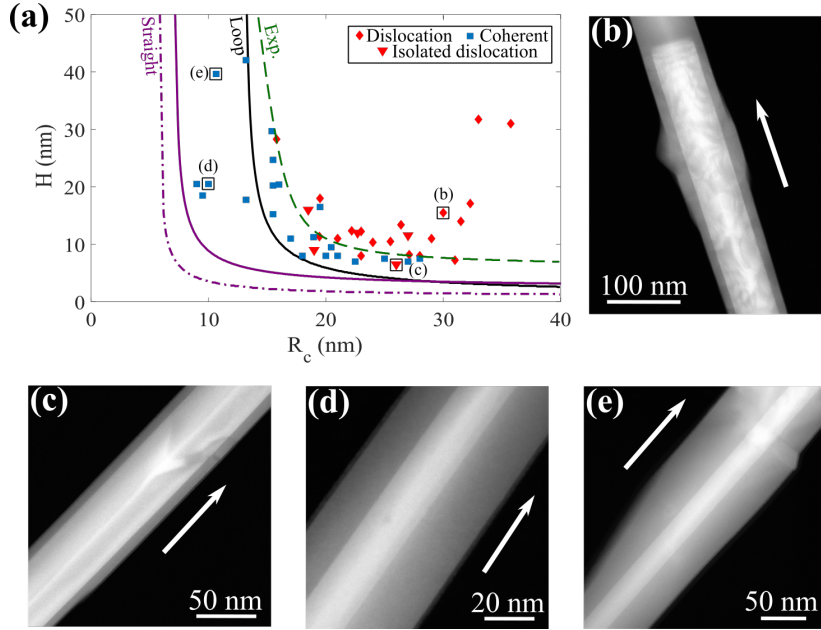


Figure F4: Limites géométriques pour la croissance sans défaut des nanofils cœur/coquille de GaAs/GaP. (a) Symboles : dimensions de cœur et de coquille auxquelles des nanofils sans dislocation (carrés bleus) et avec dislocations multiples (losanges rouges) sont observés. Les symboles triangulaires correspondent aux nanofils où des dislocations isolées sont observées. La courbe en tirets donne l'épaisseur critique expérimentale de la coquille  $h_{crit}^{exp}$  pour l'introduction des dislocations. La courbe continue noire donne l'épaisseur critique calculée pour l'introduction de la première boucle de dislocation dans un nanofil élastiquement isotrope. Les courbes magenta montrent l'épaisseur critique calculée pour l'introduction de la première dislocation ligne hors axe dans un nanofil élastiquement isotrope et avec une isotropie élastique transversale autour de l'axe de croissance, respectivement. (b-d) Images HAADF TEM de nanofils cœur/coquille de GaAs/GaP avec les dimensions indiquées par les mêmes lettres en (a), montrant des nanofils avec (b-c) et sans (d-e) dislocation. Les flèches indiquent la direction [111] de croissance du nanofil.

Pour les nanofils avec les cœurs les plus fins, les calculs donnent des valeurs critiques d'épaisseur de coquille pour la croissance sans dislocation beaucoup plus petites que celles observées dans nos expériences. Nous avons ainsi réussi à faire croître une coquille de GaP cohérente d'une épaisseur de 40 nm en nanofils avec un coquille de 11 nm (Figure F4(d)). Ces résultats montrent qu'il est possible de faire croître des coquilles sans défaut nettement plus épaisses que ce que prédit la théorie. Cela devrait être très précieux pour les futures applications aux dispositifs.



# Bibliography

- [1] J. A. del Alamo. Nanometre-scale electronics with III–V compound semiconductors. *Nature*, 479(7373):317–323, 2011.
- [2] J. Svensson, A. W. Dey, D. Jacobsson, and L.-E. Wernersson. III–V nanowire complementary metal–oxide semiconductor transistors monolithically integrated on Si. *Nano Letters*, 15(12):7898–7904, 2015.
- [3] E. Lind. High frequency III–V nanowire mosfets. *Semiconductor Science and Technology*, 31:093005, 2016.
- [4] F. Lindelöw, N. S. Garigapati, L. Södergren, M. Borg, and E. Lind. III-V nanowire MOSFETs with novel self-limiting  $\Lambda$ -ridge spacers for RF applications. *Semiconductor Science and Technology*, 35(6):065015, 2020.
- [5] M. S. Ram, K.-M. Persson, M. Borg, and L.-E. Wernersson. Low-power resistive memory integrated on III–V vertical nanowire MOSFETs on silicon. *IEEE Electron Device Letters*, 41(9):1432–1435, 2020.
- [6] J. Motohisa and Sh. Hara. Nanowire field-effect transistors. In N. Fukata and R. Rurali, editors, *Fundamental properties of semiconductor nanowires*, pages 371–431. Springer, Singapore, 2021.
- [7] D. Ren, X. Meng, Z. Rong, M. Cao, A. C. Farrell, S. Somasundaram, K. M. Azizur-Rahman, B. S. Williams, and D. L. Huffaker. Uncooled photodetector at short-wavelength infrared using InAs nanowire photoabsorbers on InP with p–n heterojunctions. *Nano Letters*, 18(12):7901–7908, 2018.
- [8] H. Sekiguchi, K. Kishino, and A. Kikuchi. Emission color control from blue to red with nanocolumn diameter of InGaN/GaN nanocolumn arrays grown on same substrate. *Applied Physics Letters*, 96(23):231104, 2010.

- [9] H. Kim, A. C. Farrell, P. Senanayake, W.-J. Lee, and D. L. Huffaker. Monolithically integrated InGaAs nanowires on 3D structured silicon-on-insulator as a new platform for full optical links. *Nano Letters*, 16(3):1833–1839, 2016.
- [10] Ya. Wu, X. Yan, X. Zhang, and X. Ren. A monolayer graphene/GaAs nanowire array schottky junction self-powered photodetector. *Applied Physics Letters*, 109(18):183101, 2016.
- [11] P. Kuyanov, S. A. McNamee, and R. R. LaPierre. GaAs quantum dots in a GaP nanowire photodetector. *Nanotechnology*, 29(12):124003, 2018.
- [12] Y. Zhang, D. Saxena, M. Aagesen, and H. Liu. Toward electrically driven semiconductor nanowire lasers. *Nanotechnology*, 30(19):192002, 2019.
- [13] G. Zhang, K. Tateno, T. Tawara, and H. Gotoh. InP/InAs quantum heterostructure nanowires toward telecom-band nanowire lasers. In N. Fukata and R; Rurali, editors, *Fundamental properties of semiconductor nanowires*, pages 433–454. Springer, Singapore, 2021.
- [14] S. Haffouz, P. J. Poole, J. Jin, X. Wu, L. Ginet, K. Mnaymneh, D. Dalacu, and R. L. Williams. Single quantum dot-in-a-rod embedded in a photonic nanowire waveguide for telecom band emission. *Applied Physics Letters*, 117:113102, 2020.
- [15] J. Wallentin, N. Anttu, D. Asoli, M. Huffman, I. Åberg, M. H. Magnusson, G. Siefert, P. Fuss-Kailuweit, F. Dimroth, B. Witzigmann, H. Q. Xu, L. Samuelson, K. Deppert, and M. T. Borgström. InP nanowire array solar cells achieving 13.8% efficiency by exceeding the ray optics limit. *Science*, 339(6123):1057–1060, 2013.
- [16] O. Saket, Ch. Himwas, V. Piazza, F. Bayle, A. Cattoni, F. Oehler, G. Patriarcho, L. Travers, St. Collin, F. H. Julien, J.-C. Harmand, and M. Tchernycheva. Nanoscale electrical analyses of axial-junction GaAsP nanowires for solar cell applications. *Nanotechnology*, 31:145708, 2020.
- [17] M. T. Borgström, M. H. Magnusson, F. Dimroth, G. Siefert, O. Höhn, H. Riel, H. Schmid, St. Wirths, M. Björk, I. Åberg, W. Peijnenburg, M. Vijver, M. Tchernycheva, V. Piazza, and L. Samuelson. Towards nanowire tandem junction solar cells on silicon. *IEEE Journal of Photovoltaics*, 8(3):733–740, 2018.
- [18] D. Mikulik, M. Mintairov, I. Nagemson, V. Evstropov, P. Romero-Gomez, M. Shvarts, and A. Fontcuberta i Morral. Extraction of p-n junction properties

- and series resistance in GaAs nanowire-based solar cells using light concentration. *Nanotechnology*, 30(9):094001, 2019.
- [19] R. R. LaPierre, A. C. E. Chia, S. J. Gibson, C. M. Haapamaki, J. Boulanger, R. Yee, P. Kuyanov, J. Zhang, N. Tajik, N. Jewell, and K. M.A. Rahman. III-V nanowire photovoltaics: Review of design for high efficiency. *Physica Status Solidi - RRL*, 7(10):815–830, 2013.
- [20] N. I. Goktas, P. Wilson, A. Ghukasyan, D. Wagner, S. McNamee, and R. R. LaPierre. Nanowires for energy: A review. *Applied Physics Reviews*, 5(4):041305, 2018.
- [21] P. K. Sahoo, R. Janissen, Mo. P. Monteiro, A. Cavalli, D. M. Murillo, M. V. Merfa, C. L. Cesar, H. F. Carvalho, A. A. de Souza, E. P. A. M. Bakkers, and M. A. Cotta. Nanowire arrays as cell force sensors to investigate adhesion-enhanced holdfast of single cell bacteria and biofilm stability. *Nano Letters*, 16(7):4656–4664, 2016.
- [22] A. C. Scofield, S.-H. Kim, J. N. Shapiro, A. Lin, B. Liang, A. Scherer, and D. L. Huffaker. Bottom-up photonic crystal lasers. *Nano Letters*, 11(12):5387–5390, 2011.
- [23] A. Standing, S. Assali, L. Gao, M. A. Verheijen, D. van Dam, Yi. Cui, P. H. L. Notten, J. E. M. Haverkort, and E. Bakkers. Efficient water reduction with gallium phosphide nanowires. *Nature Communication*, 6(1):7824, 2015.
- [24] M. Friedl, K. Cerveny, P. Weigele, G. Tütüncüoğlu, S. Martí-Sánchez, Ch. Huang, T. Patlatiuk, H. Potts, Zh. Sun, M. O. Hill, L. Güniat, W. Kim, M. Zamani, V. G. Dubrovskii, J. Arbiol, L. J. Lauhon, D. M. Zumbühl, and A. Fontcuberta i Morral. Template-assisted scalable nanowire networks. *Nano Letters*, 18(4):2666–2671, 2018.
- [25] N. Akopian, G. Patriarche, L. Liu, J.-C. Harmand, and V. Zwiller. Crystal phase quantum dots. *Nano Letters*, 10(4):1198–1201, 2010.
- [26] B. Loitsch, J. Winnerl, G. Grimaldi, J. Wierzbowski, D. Rudolph, St. Morkötter, M. Döblinger, G. Abstreiter, G. Koblmüller, and J. J. Finley. Crystal phase quantum dots in the ultrathin core of GaAs-AlGaAs core-shell nanowires. *Nano Letters*, 15(11):7544–7551, 2015.

- [27] B. Loitsch, D. Rudolph, St. Morkötter, M. Döblinger, G. Grimaldi, L. Hanschke, S. Matich, E. Parzinger, U. Wurstbauer, G. Abstreiter, J. J. Finley, and G. Koblmüller. Tunable quantum confinement in ultrathin, optically active semiconductor nanowires via reverse-reaction growth. *Advanced Materials*, 27(13):2195–2202, 2015.
- [28] E. Barrigón, M. Heurlin, Zh. Bi, B. Monemar, and L. Samuelson. Synthesis and applications of III–V nanowires. *Chemical Reviews*, 119:9170–9220, 2019.
- [29] W. Kim, L. Güniat, A. Fontcuberta i Morral, and V. Piazza. Doping challenges and pathways to industrial scalability of III-V nanowire arrays. *Applied Physics Reviews*, 8(1), 2021.
- [30] J. D. Christesen, Ch. W. Pinion, E. M. Grumstrup, J. M. Papanikolas, and J. F. Cahoon. Synthetically encoding 10 nm morphology in silicon nanowires. *Nano Letters*, 13(12):6281–6286, 2013.
- [31] D. J. Hill, T. S. Teitsworth, S. Kim, J. D. Christesen, and J. F. Cahoon. Encoding highly nonequilibrium boron concentrations and abrupt morphology in p-type/n-type silicon nanowire superlattices. *ACS Applied Materials & Interfaces*, 9(42):37105–37111, 2017.
- [32] L. Güniat, P. Caroff, and A. Fontcuberta i Morral. Vapor phase growth of semiconductor nanowires: Key developments and open questions. *Chemical Reviews*, 119(15):8958–8971, 2019.
- [33] P. C. McIntyre and A. Fontcuberta i Morral. Semiconductor nanowires: to grow or not to grow? *Materials Today Nano*, 9:100058, 2020.
- [34] J. S. Park, M. Tang, S. Chen, and H. Liu. Heteroepitaxial growth of III-V semiconductors on silicon. *Crystals*, 10(12):1–36, 2020.
- [35] A. Wolfsteller, N. Geyer, T.-K. Nguyen-Duc, P. Das Kanungo, N.D. Zakharov, M. Reiche, W. Erfurth, H. Blumtritt, S. Kalem, P. Werner, and U. Gösele. Comparison of the top-down and bottom-up approach to fabricate nanowire-based silicon/germanium heterostructures. *Thin Solid Films*, 518(9):2555–2561, 2010.
- [36] R. G. Hobbs, N. Petkov, and J. D. Holmes. Semiconductor nanowire fabrication by bottom-up and top-down paradigms. *Chemistry of Materials*, 24(11):1975–1991, 2012.

- [37] G. Priante, S. Ambrosini, V. Dubrovskii, A. Franciosi, and S. Rubini. Stopping and resuming at will the growth of GaAs nanowires. *Crystal Growth and Design*, 13(9):3976–3984, 2013.
- [38] V. G. Dubrovskii, T. Xu, A. Díaz Álvarez, S. R. Plissard, P. Caroff, F. Glas, and B. Grandidier. Self-equilibration of the diameter of Ga-catalyzed GaAs nanowires. *Nano Letters*, 15(8):5580–5584, 2015.
- [39] W. Kim, V. Dubrovskii, J. Vukajlovic-Plestina, G. Tütüncüoğlu, L. Francaviglia, L. Güniat, H. Potts, M. Friedl, J.-B. Leran, and A. Fontcuberta i Morral. Bistability of contact angle and its role in achieving quantum-thin self-assisted GaAs nanowires. *Nano Letters*, 18(1):49–57, 2018.
- [40] A. Scaccabarozzi, A. Cattoni, G. Patriarche, L. Travers, S. Collin, J.-C. Harmand, F. Glas, and F. Oehler. Stable and high yield growth of GaP and  $\text{In}_{0.2}\text{Ga}_{0.8}\text{As}$  nanowire arrays using In as a catalyst. *Nanoscale*, 12:18240–18248, 2020.
- [41] G. Koblmüller, S. Hertenberger, K. Vizbaras, M. Bichler, F. Bao, J.-P. Zhang, and G. Abstreiter. Self-induced growth of vertical free-standing InAs nanowires on Si(111) by molecular beam epitaxy. *Nanotechnology*, 21(36):365602, 2010.
- [42] K. A. Bertness, N. A. Sanford, J. M. Barker, J. B. Schlager, A. Roshko, A. V. Davydov, and I. Levin. Catalyst-free growth of GaN nanowires. *Journal of Electronic Materials*, 35(4):576–580, 2006.
- [43] T. Hamano, H. Hirayama, and Yo. Aoyagi. New technique for fabrication of two-dimensional photonic bandgap crystals by selective epitaxy. *Japanese Journal of Applied Physics*, 36:L286–L288, 1997.
- [44] J. Noborisaka, J. Motohisa, and T. Fukui. Catalyst-free growth of GaAs nanowires by selective-area metalorganic vapor-phase epitaxy. *Applied Physics Letters*, 86(21):213102, 2005.
- [45] C.-Y. Wen, M. C. Reuter, J. Bruley, J. Tersoff, S. Kodambaka, E. A. Stach, and F. M. Ross. Formation of compositionally abrupt axial heterojunctions in silicon-germanium nanowires. *Science*, 326(5957):1247–1250, 2009.
- [46] P. Krogstrup, J. Yamasaki, C. B. Sørensen, E. Johnson, J. B. Wagner, R. Pennington, M. Aagesen, N. Tanaka, and J. Nygård. Junctions in axial III-V heterostructure nanowires obtained via an interchange of group III elements. *Nano Letters*, 9(11):3689–3693, 2009.

- [47] A. I. Persson, M. W. Larsson, S. Stenström, B. J. Ohlsson, L. Samuelson, and L. R. Wallenberg. Solid-phase diffusion mechanism for GaAs nanowire growth. *Nature Materials*, 3(10):677–681, 2004.
- [48] S. Kodambaka, J. Tersoff, M. C. Reuter, and F. M. Ross. Germanium nanowire growth below the eutectic temperature. *Science*, 316(5825):729–732, 2007.
- [49] K. Dick, K. Deppert, T. Martensson, B. Mandl, L. Samuelson, and W. Seifert. Failure of the vapor-liquid-solid mechanism in Au-assisted MOVPE growth of InAs nanowires. *Nano Letters*, 5(4):761–764, 2005.
- [50] R. S. Wagner and W. C. Ellis. Vapor-liquid-solid mechanism of single crystal growth. *Applies Physics Letters*, 4:89–90, 1964.
- [51] E. I. Givargizov. Fundamental aspects of VLS growth. *Journal of Crystal Growth*, 31(C):20–30, 1975.
- [52] T. Mårtensson, C. P. T. Svensson, B. A. Wacaser, M. W. Larsson, W. Seifert, K. Deppert, A. Gustafsson, L. R. Wallenberg, and L. Samuelson. Epitaxial III-V nanowires on silicon. *Nano Letters*, 4(10):1987–1990, 2004.
- [53] A. L. Roest, M. A. Verheijen, O. Wunnicke, S. Serafin, H. Wondergem, and E. Bakkers. Position-controlled epitaxial III-V nanowires on silicon. *Nanotechnology*, 17(11), 2006.
- [54] M. T. Borgström, M. A. Verheijen, G. Immink, T. De Smet, and E. Bakkers. Interface study on heterostructured GaP-GaAs nanowires. *Nanotechnology*, 17(16):4010–4013, 2006.
- [55] T. Sato, K. Hiruma, M. Shirai, K. Tominaga, K. Haraguchi, T. Katsuyama, and T. Shimada. Site-controlled growth of nanowiskers. *Applied Physics Letters*, 159:159, 1995.
- [56] Z. H. Wu, X. Y. Mei, D. Kim, M. Blumin, and H. E. Ruda. Growth of Au-catalyzed ordered GaAs nanowire arrays by molecular-beam epitaxy. *Applied Physics Letters*, 81(27):5177–5179, 2002.
- [57] J.-C. Harmand, G. Patriarche, N. Péré-Laperne, M. N. Mérat-Combes, L. Travers, and F. Glas. Analysis of vapor-liquid-solid mechanism in Au-assisted GaAs nanowire growth. *Applied Physics Letters*, 87(20):1–3, 2005.

- [58] M. Tchernycheva, L. Travers, G. Patriarche, F. Glas, J.-C. Harmand, G. E. Cirlin, and V. G. Dubrovskii. Au-assisted molecular beam epitaxy of InAs nanowires: Growth and theoretical analysis. *Journal of Applied Physics*, 102(9), 2007.
- [59] K. A. Dick. A review of nanowire growth promoted by alloys and non-alloying elements with emphasis on Au-assisted III-V nanowires. *Progress in Crystal Growth and Characterization of Materials*, 54(3-4):138–173, 2008.
- [60] M. C. Plante and R. R. LaPierre. Growth mechanisms of GaAs nanowires by gas source molecular beam epitaxy. *Journal of Crystal Growth*, 286(2):394–399, 2006.
- [61] C. Chen, M.C. Plante, C. Fradin, and R.R. LaPierre. Layer-by-layer and step-flow growth mechanisms in GaAsP/GaP nanowire heterostructures. *Journal of Material Research*, 21(11):2801–2809, 2006.
- [62] R. L. Barns and W. C. Ellis. Whisker crystals of gallium arsenide and gallium phosphide grown by the vapor - liquid - solid mechanism. *Journal of Applied Physics*, 36(7):2296–2301, 1965.
- [63] C. J. Novotny and P. K. L. Yu. Vertically aligned, catalyst-free InP nanowires grown by metalorganic chemical vapor deposition. *Applied Physics Letters*, 87(20):1–3, 2005.
- [64] B. Mandl, J. Stangl, Th. Mårtensson, A. Mikkelsen, J. Eriksson, L. S. Karlsson, G. Bauer, L. Samuelson, and W. Seifert. Au-free epitaxial growth of InAs nanowires. *Nano Letters*, 6(8):1817–1821, 2006.
- [65] M. Mattila, T. Hakkarainen, and H. Lipsanen. Catalyst-free fabrication of InP and InP(N) nanowires by metalorganic vapor phase epitaxy. *Journal of Crystal Growth*, 298:640–643, 2007.
- [66] A. Fontcuberta i Morral, C. Colombo, G. Abstreiter, J. Arbiol, and J. R. Morante. Nucleation mechanism of gallium-assisted molecular beam epitaxy growth of gallium arsenide nanowires. *Applied Physics Letters*, 92(6), 2008.
- [67] F. Jabeen, V. Grillo, S. Rubini, and F. Martelli. Self-catalyzed growth of GaAs nanowires on cleaved Si by molecular beam epitaxy. *Nanotechnology*, 19(27), 2008.

- [68] J. H. Paek, T. Nishiwaki, M. Yamaguchi, and N. Sawaki. Catalyst free MBE-VLS growth of GaAs nanowires on (111)Si substrate. *Physica Status Solidi C*, 6(6):1436–1440, 2009.
- [69] B. Bauer, A. Rudolph, M. Soda, A. Fontcuberta i Morral, J. Zweck, D. Schuh, and E. Reiger. Position controlled self-catalyzed growth of GaAs nanowires by molecular beam epitaxy. *Nanotechnology*, 21(43):435601, 2010.
- [70] S. Plissard, K. A. Dick, G. Larrieu, S. Godey, A. Addad, X. Wallart, and P. Caroff. Gold-free growth of GaAs nanowires on silicon: Arrays and polytypism. *Nanotechnology*, 21(38):385602, 2010.
- [71] S. Plissard, G. Larrieu, X. Wallart, and P. Caroff. High yield of self-catalyzed GaAs nanowire arrays grown on silicon via gallium droplet positioning. *Nanotechnology*, 22(27):275602, 2011.
- [72] S. J. Gibson, J. P. Boulanger, and R. R. LaPierre. Opportunities and pitfalls in patterned self-catalyzed GaAs nanowire growth on silicon. *Semiconductor Science and Technology*, 28(10):105095, 2013.
- [73] A. M. Munshi, D. L. Dheeraj, V. T. Fauske, D. C. Kim, J. Huh, J. F. Reinertsen, L. Ahtapodov, K. D. Lee, B. Heidari, A. T.J. Van Helvoort, B. O. Fimland, and H. Weman. Position-controlled uniform GaAs nanowires on silicon using nanoimprint lithography. *Nano Letters*, 14(2):960–966, 2014.
- [74] F. Matteini, G. Tütüncüoğlu, D. Ruffer, E. Alarcón-Lladó, and A. Fontcuberta i Morral. Ga-assisted growth of GaAs nanowires on silicon, comparison of surface  $\text{SiO}_x$  of different nature. *Journal of Crystal Growth*, 404:246–255, 2014.
- [75] F. Matteini, G. Tütüncüoğlu, H. Potts, F. Jabeen, and A. Fontcuberta i Morral. Wetting of Ga on  $\text{SiO}_x$  and its impact on GaAs nanowire growth. *Crystal Growth & Design*, 15(7):3105–3109, 2015.
- [76] E. Russo-Averchi, J. Vukajlovic-Plestina, G. Tütüncüoğlu, F. Matteini, A. Dalmau-Mallorquí, M. De La Mata, D. Ruffer, H. A. Potts, J. Arbiol, S. Conesa-Boj, and A. Fontcuberta i Morral. High yield of GaAs nanowire arrays on Si mediated by the pinning and contact angle of Ga. *Nano Letters*, 15(5):2869–2874, 2015.
- [77] H. Küpers, R. B. Lewis, A. Tahraoui, M. Matalla, O. Krüger, F. Bastiman, H. Riechert, and L. Geelhaar. Diameter evolution of selective area grown Ga-assisted GaAs nanowires. *Nano Research*, 11:2885–2893, 2018.

- [78] J. Vukajlovic-Plestina, W. Kim, L. Ghisalberti, G. Varnavides, G. Tütüncüoğlu, H. Potts, M. Friedl, L. Güniat, W. C. Carter, V. G. Dubrovskii, and A. Fontcuberta i Morral. Fundamental aspects to localize self-catalyzed III-V nanowires on silicon. *Nature Communication*, 10(1):869, 2019.
- [79] D. P. Wilson, V. G. Dubrovskii, and R. R. LaPierre. Improving the yield of GaAs nanowires on silicon by Ga pre-deposition. *Nanotechnology*, 32(26):265301, 2021.
- [80] A. Biermanns. *X-ray diffraction from single GaAs nanowires*. Thesis, Universität Siegen, 2012.
- [81] S. Assali, I. Zardo, S. Plissard, D. Kriegner, M. A. Verheijen, G. Bauer, A. Meijerink, A. Belabbes, F. Bechstedt, J. E. M. Haverkort, and E. Bakkers. Direct band gap wurtzite gallium phosphide nanowires. *Nano Letters*, 13(4):1559–1563, 2013.
- [82] M. I. McMahon and R. J. Nelmes. Observation of a wurtzite form of gallium arsenide. *Physical Review Letters*, 95(21):215505, 2005.
- [83] F. Bechstedt and A. Belabbes. Structure, energetics, and electronic states of III-V compound polytypes. *Journal of Physics: Condensed Matter*, 25(27):273201, 2013.
- [84] S. Adachi. Material parameters of  $\text{In}_{1-x}\text{Ga}_x\text{As}_y\text{P}_{1-y}$  and related binaries. *Journal of Applied Physics*, 53(12):8775–8792, 1982.
- [85] R.S. Wagner and W.C. Ellis. *Vapor-liquid-solid Mechanism of Crystal Growth and Its Application to Silicon*. Bell telephone system technical publications. Bell Telephone Laboratories, 1965.
- [86] V. G. Dubrovskii. *Nucleation Theory and Growth of Nanostructures*. NanoScience and Technology. Springer Berlin Heidelberg, Berlin, Heidelberg, 2014.
- [87] V. G. Dubrovskii. *Theory of VLS growth of compound semiconductors*, volume 93. Elsevier Inc., 1 edition, 2015.
- [88] V. G. Dubrovskii and F. Glas. Vapor-liquid-solid growth of semiconductor nanowires. In N. Fukata and R. Rurali, editors, *Fundamental properties of semiconductor nanowires*, pages 3–107. Springer, Singapore, 2021.
- [89] F. Glas, J.-C. Harmand, and G. Patriarche. Why does wurtzite form in nanowires of III-V zinc blende semiconductors? *Physical Review Letters*, 99(14):3–6, 2007.

- [90] F. Glas, M. Ramdani, G. Patriarche, and J.-C. Harmand. Predictive modeling of self-catalyzed III-V nanowire growth. *Physical review B*, 88:195304, 2013.
- [91] D. Jacobsson, F. Panciera, J. Tersoff, M. C. Reuter, S. Lehmann, St. Hofmann, K. A. Dick, and F. M. Ross. Interface dynamics and crystal phase switching in GaAs nanowires. *Nature*, 531(7594):317–322, 2016.
- [92] J.-C. Harmand, G. Patriarche, F. Glas, F. Panciera, I. Florea, J.-L. Maurice, L. Travers, and Ya. Ollivier. Atomic step flow on a nanofacet. *Physical Review Letters*, 121(16):166101, 2018.
- [93] F. Panciera, Zh. Baraissov, G. Patriarche, V. Dubrovskii, F. Glas, L. Travers, U. Mirsaidov, and J.-C. Harmand. Phase selection in self-catalyzed GaAs nanowires. *Nano Letters*, 20:1669–1675, 2020.
- [94] J. Johansson and E. D. Leshchenko. Zinc blende and wurtzite crystal structure formation in gold catalyzed InGaAs nanowires. *Journal of Crystal Growth*, 509:118–123, 2019.
- [95] O. Yu. Koval, V. V. Fedorov, A. D. Bolshakov, I. E. Eliseev, S. V. Fedina, G. A. Sapunov, S. A. Udovenko, L. N. Dvoretckaia, D. A. Kirilenko, R. G. Burkovsky, and I. S. Mukhin. Xrd evaluation of wurtzite phase in mbe grown self-catalyzed GaP nanowires. *Nanomaterials*, 11(4):1–13, 2021.
- [96] F. Oehler, A. Cattoni, A. Scaccabarozzi, G. Patriarche, F. Glas, and J.-C. Harmand. Measuring and modelling the growth dynamics of self-catalyzed GaP nanowire arrays. *Nano Letters*, 18:701–708, 2018.
- [97] D. Dalacu, A. Kam, D. G. Austing, X. Wu, J. Lapointe, G. C. Aers, and P. J. Poole. Selective-area vapour–liquid–solid growth of InP nanowires. *Nanotechnology*, 20:395602, 2009.
- [98] M. Ramdani, J.-C. Harmand, F. Glas, G. Patriarche, and L. Travers. Arsenic pathways in self-catalyzed growth of GaAs nanowires. *Crystal Growth & Design*, 13:91–96, 2013.
- [99] P. Krogstrup, H. I. Jorgensen, E. Johnson, M. H. Madsen, C. B. Sorensen, A. Fontcuberta i Morral, M. Aagesen, J. Nygard, and F. Glas. Advances in the theory of III–V nanowire growth dynamics. *Journal of Physics D: Applied Physics*, 46:313001, 2013.

- [100] V. G. Dubrovskii, G. E. Cirlin, I. P. Soshnikov, A. A. Tonkikh, N. V. Sibirev, Yu. B. Samosenko, and V. M. Ustinov. Diffusion-induced growth of GaAs nanowhiskers during molecular beam epitaxy: Theory and experiment. *Physical Review B*, 71:205325, 2005.
- [101] G. Priante, G. Patriarche, F. Oehler, F. Glas, and J.-C. Harmand. Abrupt GaP/GaAs interfaces in self-catalyzed nanowires. *Nano Letters*, 15:6036–6041, 2015.
- [102] G. Priante, F. Glas, G. Patriarche, K. Pantzas, F. Oehler, and J.-C. Harmand. Sharpening the interfaces of axial heterostructures in self-catalyzed AlGaAs nanowires: Experiment and theory. *Nano Letters*, 16(3):1917–1924, 2016.
- [103] F. Glas. Comparison of modeling strategies for the growth of heterostructures in III–V nanowires. *Crystal Growth & Design*, 17(9):4785–4794, 2017.
- [104] V.G. Dubrovskii, A.A. Koryakin, and N.V. Sibirev. Understanding the composition of ternary III-V nanowires and axial nanowire heterostructures in nucleation-limited regime. *Materials & Design*, 132:400–408, 2017.
- [105] M. Hei, A. Gustafsson, S. Conesa-Boj, F. Peir, J. R. Morante, G. Abstreiter, J. Arbiol, L. Samuelson, and A. Fontcuberta i Morral. Catalyst-free nanowires with axial  $\text{In}_x\text{Ga}_{1-x}\text{As}/\text{GaAs}$  heterostructures. *Nanotechnology*, 20(7):075603, 2009.
- [106] D. Ferrand and J. Cibert. Strain in crystalline core-shell nanowires. *EPJ Applied Physics*, 67(3), 2014.
- [107] Zh. Zhu, J. Svensson, A. R. Persson, R. Wallenberg, A. V. Gromov, and L. E. Wernersson. Compressively-strained GaSb nanowires with core-shell heterostructures. *Nano Research*, 13(9):2517–2524, 2020.
- [108] Y. Sun, S. E. Thompson, and T. Nishida. Physics of strain effects in semiconductors and metal-oxide-semiconductor field-effect transistors. *Journal of Applied Physics*, 101(10):104503, 2007.
- [109] F. Glas. Critical dimensions for the plastic relaxation of strained axial heterostructures in free-standing nanowires. *Physical Review B*, 74(12):2–5, 2006.
- [110] F. Glas. Strain in nanowires and nanowire heterostructures. In A. Fontcuberta i Morral, S. A. Dayeh, and Ch. Jagadish, editors, *Semiconductor nanowires I:*

- Growth and theory*, volume 93 of *Semiconductors and Semimetals*, pages 79–123. Elsevier, 2015.
- [111] S. Kim and J. F. Cahoon. Geometric nanophotonics: Light management in single nanowires through morphology. *Accounts of Chemical Research*, 52(12):3511–3520, 2019.
- [112] L.-W. Chou and M. A. Filler. Engineering multimodal localized surface plasmon resonances in silicon nanowires. *Angewandte Chemie International Edition*, 52(31):8079–8083, 2013.
- [113] S. Kim, K. H. Kim, D. J. Hill, H. G. Park, and J. F. Cahoon. Mie-coupled bound guided states in nanowire geometric superlattices. *Nature Communication*, 9(1):2781, 2018.
- [114] J.J. Harris, B. A. Joyce, and P.J. Dobson. Oscillations in the surface structure of Sn-doped GaAs during growth by MBE. *Surface Science*, 103(1):L90–L96, 1981.
- [115] C.T. Foxon and B.A. Joyce. Interaction kinetics of As<sub>4</sub> and Ga on {100} GaAs surfaces using a modulated molecular beam technique. *Surface Science*, 50(2):434–450, 1975.
- [116] J. Y. Tsao, T. M. Brennan, and B. E. Hammons. Reflection mass spectrometry of As incorporation during GaAs molecular beam epitaxy. *Applied Physics Letters*, 53(4):288–290, 1988.
- [117] C. Webb, D. Liu, and J. N. Eckstein. Evidence for an As<sub>4</sub> sticking coefficient  $\geq 0.5$  in the molecular beam epitaxy of GaAs. *Applied Physics Letters*, 60(5):571–573, 1992.
- [118] E.S. Tok, J.H. Neave, J. Zhang, B.A. Joyce, and T.S. Jones. Arsenic incorporation kinetics in GaAs(001) homoepitaxy revisited. *Surface Science*, 374(1-3):397–405, 1997.
- [119] G.W. Barnes, E.S. Tok, J.H. Neave, and T.S. Jones. Phosphorus incorporation during InP(001) homoepitaxial growth by solid source molecular beam epitaxy. *Surface Science*, 531(3):L383–L387, 2003.
- [120] C. Somaschini, S. Bietti, A. Trampert, U. Jahn, C. Hauswald, H. Riechert, S. Sanguinetti, and L. Geelhaar. Control over the number density and diameter of GaAs nanowires on Si(111) mediated by droplet epitaxy. *Nano Letters*, 13(8):3607–3613, 2013.

- [121] C. Bohling and W. Sigmund. Self-limitation of native oxides explained. *Silicon*, 8(3):339–343, 2016.
- [122] A. Moldovan, F. Feldmann, G. Krugel, M. Zimmer, J. Rentsch, M. Hermle, A. Roth-Fölsch, K. Kaufmann, and C. Hagendorf. Simple cleaning and conditioning of silicon surfaces with UV/ozone sources. *Energy Procedia*, 55:834–844, 2014.
- [123] F. Glas. Vapor fluxes on the apical droplet during nanowire growth by molecular beam epitaxy. *Physica Status Solidi B*, 247(2):254–258, 2010.
- [124] T. Rieger, S. Heiderich, S. Lenk, M. I. Lepsa, and D. Grutzmacher. Ga-assisted MBE growth of GaAs nanowires using thin HSQ layer. *Journal of Crystal Growth*, 353:39–46, 2012.
- [125] P. Krogstrup, R. Popovitz-Biro, E. Johnson, M. H. Madsen, J. Nygard, and H. Shtrikman. Structural phase control in self-catalyzed growth of GaAs nanowires on silicon (111). *Nano Letters*, 10:4475–4482, 2010.
- [126] A. Kelrich, Y. Calahorra, Y. Greenberg, A. Gavrilov, S. Cohen, and D. Ritter. Shadowing and mask opening effects during selective-area vapor-liquid-solid growth of InP nanowires by metalorganic molecular beam epitaxy. *Nanotechnology*, 24(47), 2013.
- [127] C. Colombo, D. Spirkoska, M. Frimmer, G. Abstreiter, and A. Fontcuberta i Morral. Ga-assisted catalyst-free growth mechanism of GaAs nanowires by molecular beam epitaxy. *Physical Review B*, 77:155236, 2008.
- [128] S. Gibson and R. R. LaPierre. Model of patterned self-assisted nanowire growth. *Nanotechnology*, 25(41):415304, 2014.
- [129] M. H. Madsen, P. Krogstrup, E. Johnson, S. Venkatesan, E. Mühlbauer, C. Scheu, C. B. Sørensen, and J. Nygård. Experimental determination of adatom diffusion lengths for growth of InAs nanowires. *Journal of Crystal Growth*, 364:16–22, 2013.
- [130] J.-C. Harmand, F. Glas, and G. Patriarche. Growth kinetics of a single  $\text{InP}_{1-x}\text{As}_x$  nanowire. *Physical Review B*, 81:235436, 2010.
- [131] D. Scarpellini, A. Fedorov, C. Somaschini, C. Frigeri, M. Bollani, S. Bietti, R. Noetzel, and S. Sanguinetti. Ga crystallization dynamics during annealing of self-assisted GaAs nanowires. *Nanotechnology*, 28:045605, 2017.

- [132] D. Rudolph, S. Hertenberger, S. Bolte, W. Paosangthong, D. Spirkoska, M. Doblinger, M. Bichler, J. J. Finley, G. Abstreiter, and G. Koblmüller. Direct observation of noncatalytic growth regime for GaAs nanowires. *Nano Letters*, 11:3848–3854, 2011.
- [133] V. G. Dubrovskii, N. V. Sibirev, J.-C. Harmand, and F. Glas. Growth kinetics and crystal structure of semiconductor nanowires. *Physical Review B*, 78(23):235301, 2008.
- [134] J. Johansson, L. S. Karlsson, C. Patrik T. Svensson, T. Mårtensson, B. A. Wacaser, K. Deppert, L. Samuelson, and W. Seifert. Structural properties of  $\langle 111 \rangle$ B-oriented III–V nanowires. *Nature Materials*, 5(7):574–580, 2006.
- [135] N. V. Sibirev, M. A. Timofeeva, A. D. Bol’shakov, M. V. Nazarenko, and V. G. Dubrovskii. Surface energy and crystal structure of nanowhiskers of III–V semiconductor compounds. *Physics of the Solid State*, 52(7):1531–1538, 2010.
- [136] E. P. Wenaas. Equilibrium cosine law and scattering symmetry at the gas–surface interface. *The Journal of Chemical Physics*, 54(1):376–388, 1971.
- [137] G. Comsa and R. David. Dynamical parameters of desorbing molecules. *Surface Science Reports*, 5:145–198, 1985.
- [138] F. Glas and J.-C. Harmand. Calculation of the temperature profile in nanowhiskers growing on a hot substrate. *Physical Review B*, 73:155320, 2006.
- [139] A. T. Dinsdale. SGTE data for pure elements. *Calphad*, 15:317–425, 1991.
- [140] I. Ansara, C. Chatillon, H. L. Lukas, T. Nishizawa, H. Ohtani, K. Ishida, M. Hillert, B. Sundman, B. B. Argent, A. Watson, T. G. Chart, and T. Anderson. A binary database for III–V compound semiconductor systems. *Calphad*, 18:177–222, 1994.
- [141] M. Ilegems, M. B. Panish, and J. R. Arthur. Phase equilibria and vapor pressures in the Ga + P system. *The Journal of Chemical Thermodynamics*, 6:157–177, 1974.
- [142] M. Tmar, A. Gabriel, C. Chatillon, and I. Ansara. Critical analysis and optimization of the thermodynamic properties and phase diagrams in the III-V compounds: The In-P and Ga-P systems. *Journal of Crystal Growth*, 68:557–580, 1984.

- [143] V. G. Dubrovskii, N. V. Sibirev, G. E. Cirlin, J. C. Harmand, and V. M. Ustinov. Theoretical analysis of the vapor-liquid-solid mechanism of nanowire growth during molecular beam epitaxy. *Physical Review E*, 73:021603, 2006.
- [144] E. D. Leshchenko, P. Kuyanov, R. R. LaPierre, and V. G. Dubrovskii. Tuning the morphology of self-assisted GaP nanowires. *Nanotechnology*, 29:225603, 2018.
- [145] D. Wilson, A. Sokolovskii, R.R. LaPierre, F. Panciera, F. Glas, and V. G. Dubrovskii. Modeling the dynamics of interface morphology and crystal phase change in self-catalyzed GaAs nanowires. *Nanotechnology*, 31:485602, 2020.
- [146] S. Ambrosini, M. Fanetti, V. Grillo, A. Franciosi, and S. Rubini. Vapor-liquid-solid and vapor-solid growth of self-catalyzed GaAs nanowires. *AIP Advances*, 1:042142, 2011.
- [147] D. Spirkoska, J. Arbiol, A. Gustafsson, S. Conesa-Boj, F. Glas, I. Zardo, M. Heigoldt, M. H. Gass, A. L. Bleloch, S. Estrade, M. Kaniber, J. Rossler, F. Peiro, J. R. Morante, G. Abstreiter, L. Samuelson, and A. Fontcuberta i Morral. Structural and optical properties of high quality zinc-blende/wurtzite GaAs nanowire heterostructures. *Physical Review B*, 80:245325, 2009.
- [148] K. A. Dick, C. Thelander, L. Samuelson, and P. Caroff. Crystal phase engineering in single InAs nanowires. *Nano Letters*, 10:3494–3499, 2010.
- [149] R. de Lépinau, A. Scaccabarozzi, G. Patriarche, L. Travers, S. Collin, A. Cattoni, and F. Oehler. Evidence and control of unintentional As-rich shells in GaAs<sub>1-x</sub>P<sub>x</sub> nanowires. *Nanotechnology*, 30(29):294003, 2019.
- [150] T. Burgess, St. Breuer, Ph. Caroff, J. Wong-Leung, Q. Gao, H. Hoe Tan, and C. Jagadish. Twinning superlattice formation in GaAs nanowires. *ACS Nano*, 7(9):8105–8114, 2013.
- [151] M. Taherkhani, M. Willatzen, J. Mørk, N. Gregersen, and D. P.S. McCutcheon. Type-II quantum-dot-in-nanowire structures with large oscillator strength for optical quantum gate applications. *Physical Review B*, 96(12):125408, 2017.
- [152] S. Kim, D. J. Hill, Ch. W. Pinion, J. D. Christesen, J. R. McBride, and J. F. Cahoon. Designing morphology in epitaxial silicon nanowires: The role of gold, surface chemistry, and phosphorus doping. *ACS Nano*, 11(5):4453–4462, 2017.
- [153] H. Seidel, L. Csepregi, A. Heuberger, and H. Baumgärtel. Anisotropic etching of crystalline silicon in alkaline solutions: I. orientation dependence and behavior

- of passivation layers. *Journal of The Electrochemical Society*, 137(11):3612–3626, 1990.
- [154] C. Kallesøe, K. Mølhav, K. F. Larsen, D. Engstrøm, T. M. Hansen, P. Bøggild, Th. Mårtensson, M. Borgström, and L. Samuelson. Integration, gap formation, and sharpening of III-V heterostructure nanowires by selective etching. *Journal of Vacuum Science & Technology B*, 28(1):21–26, 2010.
- [155] G. Fülöp, S. D’Hollosy, L. Hofstetter, A. Baumgartner, J. Nygård, C. Schönenberger, and S. Csonka. Wet etch methods for InAs nanowire patterning and self-aligned electrical contacts. *Nanotechnology*, 27(19):195303, 2016.
- [156] D. S. Oliveira, L.H.G. Tizei, D. Ugarte, and M. A. Cotta. Spontaneous periodic diameter oscillations in InP nanowires: The role of interface instabilities. *Nano Letters*, 13(1):9–13, 2013.
- [157] E. I. Givargizov. Periodic instability in whisker growth. *Journal of Crystal Growth*, 20(3):217–226, 1973.
- [158] D. S. Oliveira, M. Zavarize, L.H.G. Tizei, M. Walls, C. A. Ospina, F. Iikawa, D. Ugarte, and M. A. Cotta. Different growth regimes in InP nanowire growth mediated by Ag nanoparticles. *Nanotechnology*, 28(50):505604, 2017.
- [159] B. Mattias Borg, M. Ek, K. A. Dick, B. Ganjipour, A. W. Dey, C. Thelander, and L. E. Wernersson. Diameter reduction of nanowire tunnel heterojunctions using *in situ* annealing. *Applied Physics Letters*, 99(20):203101, 2011.
- [160] F. Del Giudice, J. Becker, C. De Rose, M. Döblinger, D. Ruhstorfer, L. Suominen, J. Treu, H. Riedl, J. J. Finley, and G. Koblmüller. Ultrathin catalyst-free InAs nanowires on silicon with distinct 1D sub-band transport properties. *Nanoscale*, 12(42):21857–21868, 2020.
- [161] I. Ilkiv, D. Kirilenko, K. Kotlyar, and A. Bouravleuv. Thermal decomposition of GaAs nanowires. *Nanotechnology*, 31(5):055701, 2020.
- [162] G. Zhang, K. Tateno, T. Sogawa, and H. Gotoh. Diameter-tailored telecom-band luminescence in InP/InAs heterostructure nanowires grown on InP (111)B substrate with continuously-modulated diameter from microscale to nanoscale. *Nanotechnology*, 29(15):155202, 2018.

- [163] P. Caroff, M. E. Messing, B. Mattias Borg, K. A. Dick, K. Deppert, and L. E. Wernersson. InSb heterostructure nanowires: MOVPE growth under extreme lattice mismatch. *Nanotechnology*, 20(49):495606, 2009.
- [164] J. L. Webb, J. Knutsson, M. Hjort, S. Gorji Ghalamestani, K. A. Dick, R. Timm, and A. Mikkelsen. Electrical and surface properties of InAs/InSb nanowires cleaned by atomic hydrogen. *Nano Letters*, 15(8):4865–4875, 2015.
- [165] O. Arif, V. Zannier, V. G. Dubrovskii, I. V. Shtrom, F. Rossi, F. Beltram, and L. Sorba. Growth of self-catalyzed InAs/InSb axial heterostructured nanowires: Experiment and theory. *Nanomaterials*, 10(3):494, 2020.
- [166] F. Panciera. Private communication, jan 2021.
- [167] J. Tersoff. Stable self-catalyzed growth of III-V nanowires. *Nano Letters*, 15(10):6609–6613, 2015.
- [168] T. Takebe, M. Fujii, T. Yamamoto, T. Fujita, and T. Watanabe. Orientation-dependent Ga surface diffusion in molecular beam epitaxy of GaAs on GaAs patterned substrates. *Journal of Applied Physics*, 81:7273, 1997.
- [169] F. Boxberg, N. Saøndergaard, and H. Q. Xu. Elastic and piezoelectric properties of zincblende and wurtzite crystalline nanowire heterostructures. *Advanced Materials*, 24(34):4692–4706, 2012.
- [170] C. M. Warwick and T. W. Clyne. Development of composite coaxial cylinder stress analysis model and its application to SIC monofilament systems. *Journal of Material Science*, 26:3817–3827, 1991.
- [171] Yo. Mikata and M. Taya. Stress field in a coated continuous fiber composite subjected to thermo-mechanical loadings. *Journal of Composite Materials*, 19(6):554–578, 1985.
- [172] T. Trammel, X. Zhang, Yu. Li, L.-Q. Chen, and E. Dickey. Equilibrium strain-energy analysis of coherently strain core-shell nanowires. *Journal of Crystal Growth*, 310:3084–3092, 2008.
- [173] S. Raychaudhuri and E. T. Yu. Critical dimensions in coherently strained coaxial nanowire heterostructures. *Journal of Applied Physics*, 99(11):114308, 2006.
- [174] S. Raychaudhuri and E. T. Yu. Calculation of critical dimensions for wurtzite and cubic zinc blende coaxial nanowire heterostructures. *Journal of Vacuum Science & Technology B: Microelectronics and Nanometer Structures*, 24(4):2053, 2006.

- [175] C. M. Haapamaki, J. Baugh, and R. R. LaPierre. Critical shell thickness for InAs- $\text{Al}_x\text{In}_{1-x}\text{As(P)}$  core-shell nanowires. *Journal of Applied Physics*, 112(12):124305, 2012.
- [176] O. Salehzadeh, K. L. Kavanagh, and S. P. Watkins. Geometric limits of coherent III-V core/shell nanowires. *Journal of Applied Physics*, 114(5):054301, 2013.
- [177] M. Yu. Gutkin, I. A. Ovid'ko, and A. G. Sheinerman. Misfit dislocations in wire composite solids. *Journal of Physics Condensed Matter*, 12(25):5391–5401, 2000.
- [178] A. G. Sheinerman and M. Yu. Gutkin. Misfit disclinations and dislocation walls in a two-phase cylindrical composite. *Physica Status Solidi A*, 184(2):485–505, 2001.
- [179] I. A. Ovid'ko and A. G. Sheinerman. Misfit dislocation loops in composite nanowires. *Philosophical Magazine*, 84(20):2103–2118, 2004.
- [180] K. E. Aifantis, A. L. Kolesnikova, and A. E. Romanov. Nucleation of misfit dislocations and plastic deformation in core/shell nanowires. *Philosophical Magazine*, 87(30):4731–4757, 2007.
- [181] M. Yu. Gutkin, C. Enzevaeae, and H. M. Shodja. Interface effects on elastic behavior of an edge dislocation in a core-shell nanowire embedded to an infinite matrix. *International Journal of Solids and Structures*, 50(7-8):1177–1186, 2013.
- [182] A. P. Chernakov, A. L. Kolesnikova, M. Yu. Gutkin, and A. E. Romanov. Periodic array of misfit dislocation loops and stress relaxation in core-shell nanowires. *International Journal of Engineering Science*, 156:103367, 2020.
- [183] A.M. Smirnov, S.A. Krasnitskii, and M.Yu. Gutkin. Generation of misfit dislocations in a core-shell nanowire near the edge of prismatic core. *Acta Materialia*, 186:494–510, 2020.
- [184] J. Menéndez, R. Singh, and J. Drucker. Theory of strain effects on the Raman spectrum of Si-Ge core-shell nanowires. *Annalen der Physik*, 523(1-2):145–156, 2011.
- [185] C. Kloeffel, M. Trif, and D. Loss. Acoustic phonons and strain in core/shell nanowires. *Physical Review B*, 90(11):1–20, 2014.

- [186] M. V. Nazarenko, N. V. Sibirev, K. Wei Ng, F. Ren, W. Son Ko, V. G. Dubrovskii, and C. Chang-Hasnain. Elastic energy relaxation and critical thickness for plastic deformation in the core-shell InGaAs/GaAs nanopillars. *Journal of Applied Physics*, 113(10):104311, 2013.
- [187] N. Søndergaard, Yu. He, C. Fan, R. Han, T. Guhr, and H. Q. Xu. Strain distributions in lattice-mismatched semiconductor core-shell nanowires. *Journal of Vacuum Science & Technology B: Microelectronics and Nanometer Structures*, 27(2):827, 2009.
- [188] J. Grönqvist, N. Søndergaard, F. Boxberg, Th. Guhr, S. Åberg, and H. Q. Xu. Strain in semiconductor core-shell nanowires. *Journal of Applied Physics*, 106(5):053508, 2009.
- [189] M. Montazeri, M. Fickenscher, L. M. Smith, H. E. Jackson, J. Yarrison-Rice, J. H. Kang, Q. Gao, H. Hoe Tan, Ch. Jagadish, Ya. Guo, J. Zou, M. E. Pistol, and C. E. Pryor. Direct measure of strain and electronic structure in GaAs/GaP core-shell nanowires. *Nano Letters*, 10(3):880–886, 2010.
- [190] S. Lazarev, D. J. O. Göransson, M. Borgström, M. E. Messing, H. Q. Xu, D. Dzhi-gaev, O. M. Yefanov, S. Bauer, T. Baumbach, R. Feidenhans'l, L. Samuelson, and I. A Vartanyants. Revealing misfit dislocations in InAs<sub>x</sub>P<sub>1-x</sub>-InP core-shell nanowires by X-ray diffraction. *Nanotechnology*, 30(50):505703, 2019.
- [191] K. Hestroffer, R. Mata, D. Camacho, C. Leclere, G. Tourbot, Y. M. Niquet, A. Cros, C. Bougerol, H. Renevier, and B. Daudin. The structural properties of GaN/AlN core-shell nanocolumn heterostructures. *Nanotechnology*, 21(41):415702, 2010.
- [192] M. Arjmand, C. Benjamin, and I. Szlufarska. Analytical elastoplastic analysis of heteroepitaxial core-shell nanowires. *AIP Advances*, 9(5):055119, 2019.
- [193] J. P. Hirth and J. Lothe. *Theory of Dislocations*. Wiley, New York, second edition, 1982.
- [194] J.W. Matthews and A.E. Blakeslee. Defects in epitaxial multilayers. *Journal of Crystal Growth*, 27:118–125, 1974.
- [195] J. H. Van Der Merwe. Crystal interfaces. Part II. Finite overgrowths. *Journal of Applied Physics*, 34(1):123–127, 1963.

- [196] E. A. Fitzgerald. Dislocations in strained-layer epitaxy: theory, experiment, and applications. *Materials Science Reports*, 7(3):87–142, 1991.
- [197] E. Ertekin, P. A. Greaney, D. C. Chrzan, and T. D. Sands. Equilibrium limits of coherency in strained nanowire heterostructures. *Journal of Applied Physics*, 97(11):114325, 2005.
- [198] H. Ye, P. Lu, Zh. Yu, and L. Han. Critical lateral dimension for a nanoscale-patterned heterostructure using the finite element method. *Semiconductor Science and Technology*, 24(2):025029, 2009.
- [199] X. Yan, Sh. Fan, X. Zhang, and X. Ren. Analysis of critical dimensions for nanowire core-multishell heterostructures. *Nanoscale Research Letters*, 10(1):389, 2015.
- [200] J. Colin. Prismatic dislocation loops in strained core-shell nanowire heterostructures. *Physical Review B*, 82(5):1–5, 2010.
- [201] G. Perillat-Merceroz, R. Thierry, P. H. Jouneau, P. Ferret, and G. Feuillet. Strain relaxation by dislocation glide in ZnO/ZnMgO core-shell nanowires. *Applied Physics Letters*, 100(17):173102, 2012.
- [202] S. A. Dayeh, W. Tang, F. Boini, K. L. Kavanagh, H. Zheng, J. Wang, N. H. Mack, G. Swadener, J. Yu. Huang, L. Miglio, K.-N. Tu, and S. T. Picraux. Direct measurement of coherency limits for strain relaxation in heteroepitaxial core/shell nanowires. *Nano Letters*, 13(5):1869–1876, 2013.
- [203] S. Conesa-Boj, F. Boini, E. Russo-Averchi, S. Dunand, M. Heiss, D. Ruffer, N. Wyrsh, Ch. Ballif, L. Miglio, and A. Fontcuberta i Morral. Plastic and elastic strain fields in GaAs/Si core-shell nanowires. *Nano Letters*, 14(4):1859–1864, 2014.
- [204] R. B. Lewis, L. Nicolai, H. Kupers, M. Ramsteiner, A. Trampert, and L. Geelhaar. Anomalous strain relaxation in core-shell nanowire heterostructures via simultaneous coherent and incoherent growth. *Nano Letters*, 17(1):136–142, 2017.
- [205] K. L. Kavanagh. Misfit dislocations in nanowire heterostructures. *Semiconductor Science and Technology*, 25(2):024006, 2010.
- [206] R. Popovitz-Biro, A. Kretinin, P. Von Huth, and H. Shtrikman. InAs/GaAs core-shell nanowires. *Crystal Growth & Design*, 11(9):3858–3865, 2011.

- [207] J. F. Nye. *Physical properties of crystals : their representation by tensors and matrices*. Oxford University Press, 1985.
- [208] J. J. Wortman and R. A. Evans. Young's modulus, shear modulus, and Poisson's ratio in silicon and germanium. *Journal of Applied Physics*, 36(1):153–156, 1965.
- [209] J. D. Eshelby. The determination of the elastic field of an ellipsoidal inclusion, and related problems. *Proceedings of the Royal Society A*, 241(1226):376–396, 1957.
- [210] St. Timoshenko and J. N. Goodier. *Theory of Elasticity*. McGraw-Hill, New York, third edition, 1970.
- [211] A. E. Romanov and V. I. Vladimirov. Disclinations in crystalline solids. In F.R.N. Nabarro, editor, *Dislocations in Solids. Vol. 9: Dislocations and Disclinations*. North-Holland, Amsterdam, 1992.
- [212] J. H. van der Merwe. Strain relaxation in epitaxial overlayers. *Journal of Electronic Materials*, 20(7):793–803, 1991.
- [213] R. Hull and J. C. Bean. Nucleation of misfit dislocations in strained layer epitaxy in the  $\text{Ge}_x\text{Si}_{1-x}$  system . *Journal of Vacuum Science & Technology A*, 7(4):2580–2585, 1989.
- [214] M. Peach and J. S. Koehler. The forces exerted on dislocations and the stress fields produced by them. *Physical Review*, 80(3):436–439, 1950.
- [215] B. J. Spencer and J. Tersoff. Stresses and first-order dislocation energetics in equilibrium Stranski-Krastanow islands. *Physical Review B*, 63(20):205424, 2001.
- [216] A. Marzegalli, V. A. Zinovyev, F. Montalenti, A. Rastelli, M. Stoffel, T. Merdzhanova, O. G. Schmidt, and L. Miglio. Critical shape and size for dislocation nucleation in  $\text{Si}_{1-x}\text{Ge}_x$  islands on Si(001). *Physical Review Letters*, 99(23):235505, 2007.
- [217] R. Gatti, A. Marzegalli, V. A. Zinovyev, F. Montalenti, and L. Miglio. Modeling the plastic relaxation onset in realistic SiGe islands on Si(001). *Physical Review B*, 78(18):184104, 2008.
- [218] D. V. Beznasyuk, P. Stepanov, J. L. Rouvière, F. Glas, M. Verheijen, J. Claudon, and M. Hocevar. Full characterization and modeling of graded interfaces in a high lattice-mismatch axial nanowire heterostructure. *Physical Review Materials*, 4:074607, 2020.

- [219] T. B. Bateman, H. J. McSkimin, and J. M. Whelan. Elastic moduli of single-crystal gallium arsenide. *Journal of Applied Physics*, 30(4):544–545, 1959.
- [220] Y.K. Yoğurtçu, A.J. Miller, and G.A. Saunders. Pressure dependence of elastic behaviour and force constants of GaP. *Journal of Physics and Chemistry of Solids*, 42(1):49–56, 1981.
- [221] J.D. Eshelby, W.T. Read, and W. Shockley. Anisotropic elasticity with applications to dislocation theory. *Acta Metallurgica*, 1(3):251–259, 1953.
- [222] A. J.E. Foreman. Dislocation energies in anisotropic crystals. *Acta Metallurgica*, 3(4):322–330, 1955.
- [223] Y. Li, G. C. Weatherly, and M. Niewczas. TEM studies of stress relaxation in GaAsN and GaP thin films. *Philosophical Magazine*, 85(26-27):3073–3090, 2005.
- [224] Romaric de Lepinau. *GaAs-on-Si solar cells based on nanowire arrays grown by molecular beam epitaxy*. Thesis, Université Paris-Saclay, June 2020.
- [225] D. B. Williams and C. B. Carter. *Transmission Electron Microscopy*. Springer US, Boston, MA, 1 edition, 1996.
- [226] A. Mazuelas, L. González, F. A. Ponce, L. Tapfer, and F. Briones. Critical thickness determination of InAs, InP and GaP on GaAs by X-ray interference effect and transmission electron microscopy. *Journal of Crystal Growth*, 131(3-4):465–469, 1993.

## **Ingénierie du diamètre dans les hétérostructures de nanofils III-V - Expériences et modélisation**

### **Résumé :**

Les nanofils semi-conducteurs III-V présentent des propriétés physiques très intéressantes pour diverses applications. Cependant, le potentiel des dispositifs à base de nanofils ne se concrétisera pleinement que si on parvient à contrôler très précisément ces propriétés, souvent fixées au stade même de l'élaboration. Cette étude porte sur les nanofils auto-catalysés de GaAs et GaP fabriqués par épitaxie par jet moléculaire sur un substrat de Si, en mode de croissance vapeur-liquide-solide. Nous étudions sur les plans expérimental et théorique diverses questions relatives au contrôle précis du diamètre d'un nanofil, notamment sa modification déterministe durant la croissance. A cet effet, nous étudions tout d'abord la dynamique de la consommation d'une gouttelette apicale de Ga exposée à un flux de phosphore. En combinant expériences et modélisation, nous établissons les mécanismes qui contribuent à la diminution continue du volume de la goutte et calculons analytiquement les courants de matière correspondants. La mise en œuvre de ce modèle nous permet de moduler localement le diamètre des nanofils de manière contrôlée. Nous parvenons ainsi à former un segment de nanofil plus fin ou plus épais, d'un diamètre stable, au sommet d'un pied du même matériau. La seconde partie du travail est dédiée aux nanofils coeur-coquille à base de matériaux de paramètres de maille différents. Nous calculons les limites géométriques du rayon de coeur et d'épaisseur de coquille, au-delà desquelles la formation d'une première dislocation interfaciale est énergétiquement favorable. Nous fabriquons ensuite de tels nanofils dans une large gamme de rayon de coeur et d'épaisseur de coquille et déterminons, pour chaque géométrie, si des dislocations se forment ou pas. La comparaison de nos déterminations théorique et expérimentale des dimensions critiques pour la relaxation plastique montre qu'il est possible de faire croître des coquilles sans défaut beaucoup plus épaisses que prédit par la théorie. Tous ces résultats ouvrent la voie à la réalisation de structures complexes à base de nanofils, dotées d'un fort potentiel tant en physique fondamentale que pour les applications.

Mots clés : nanofils, GaAs, GaP, croissance cristalline, épitaxie par jet moléculaire, Vapeur-Liquide-Solide, structures coeur-coquille, relaxation plastique

## **Diameter engineering in III-V nanowire heterostructures - Experiments and modelling**

### **Abstract:**

III-V semiconductor nanowires are highly promising building blocks for various applications. However, the full potential of nanowire-based devices will only be realized if the nanowire physical properties, which are usually set right when these nanostructures are elaborated, can be precisely tailored. This study concentrates on self-catalyzed GaAs and GaP nanowires grown on a Si substrate by molecular beam epitaxy, in the Vapor-Liquid-Solid mode. We address experimental and theoretical issues related to the precise control of the diameter of a nanowire, in particular its deterministic modification during growth. We first study the dynamics of the consumption of a Ga apical catalyst droplet under exposure to a phosphorous flux. Combining experiments and modelling, we establish the mechanisms that contribute to the continuous decrease of the droplet volume and calculate analytically the corresponding material currents. Implementing this model allows us to modulate locally the nanowire diameter in a controllable fashion. We thus manage to form a thinner or a thicker nanowire segment with a stable diameter on top of a stem of the same material. The second part of our work is devoted to core-shell nanowires involving lattice-mismatched materials. We first compute the geometrical limits for core radius and shell thickness, above which the formation of a first interfacial dislocation is energetically favorable. We then grow GaAs/GaP core/shell nanowires in a wide range of core radii and shell thicknesses and determine for each geometry if dislocations form or not. The comparison of our theoretical and experimental determinations of the critical dimensions for plastic relaxation shows that it is possible to grow much thicker defect-free shells than predicted by theory. All these results open the way to the realization of complex structures in nanowires, which should reveal useful for basic physics as well as for applications.

Keywords: nanowires, GaAs, GaP, crystal growth, molecular beam epitaxy, Vapor-Liquid-Solid, core-shell structures, plastic relaxation